eXPRESS Polymer Letters Vol.8, No.1 (2014) 1
Available online at www.expresspolymlett.com
DOI: 10.3144/expresspolymlett.2014.1

Preface – How much are the keywords worth?

T. Czigány[*]

Department of Polymer Engineering, Faculty of Mechanical Engineering, Budapest University of Technology and Economics, Műegyetem rkp. 3., H-1111, Budapest, Hungary

Dear Readers,

You are reading the first issue of the eighth volume of ***eXPRESS* Polymer Letters**. Number 8 has traditionally been the number of luck and fulfilment (eight lives were saved in the ark of Noah: he, his wife, his three sons and their wives). This volume will be decisive in the life of our journal as well, as the impact factor, the recognition and popularity of ***eXPRESS* Polymer Letters** increases continuously. With our present impact factor of 2.294 we are in the first third of all journals worldwide, not only within our field of interest. Our aim for this year is to get into the best 25%, which is a kind of elite club. Readership and authorship of ***eXPRESS* Polymer Letters** is progressively increasing, meaning a great responsibility and hard work for the editors and the Editorial Board as they are the gate keepers whose concerns is to allow only the publication of possibly best quality articles dealing with cutting edge topics. Therefore the peer reviewing process was made even stricter, presently 82% of the submitted manuscripts are rejected, but this does not mean a slower publishing procedure.

Investigating the keywords of the articles published so far in ***eXPRESS* Polymer Letters** the first ten most frequently used ones are as follows: polymer composites; nanocomposites; mechanical properties; thermal properties; nanomaterials; biodegradable polymers; polymer synthesis and molecular engineering; smart polymers; polymer blends and alloys; biopolymers and biocomposites. These reflect well the actual R&D directions in the world, being mostly application and industry-oriented, which is of course acceptable, as research is not made for itself. But it may be also noted that one of the negative effects of the economic crisis is that project funding can hardly be won for basic research, supporting bodies are inclined to give support for applied research promising faster return. On the other hand it is not to be forgotten that applied research is always preceded by basic research (nowadays termed as exploratory research), which in fact rarely results in direct practical utilization. Another observed tendency is that the keywords of the project applications influence more the acceptance of the project than the content of the project. The term ‘nano’ became a popular keyword in science in all kinds of combinations and it was nearly impossible to get grants without this almighty expression being present in every second sentence. Sometimes one wonders, how many things appear under the ‘nano’ umbrella not recognized as such before …

Among the current popular keywords, one of the widest is ‘bio’ which suggests natural character in all kinds of combinations. As the selection of proper keywords may influence not only the evaluation of an article but also the amount of funding received, it is advisable to maintain a good balance of them.

In the New Year I wish a successful keyword selection for each author and reader of ***eXPRESS* Polymer Letters** and I would like to take the opportunity to congratulate the chief editor of our journal, Professor Karger-Kocsis on the occasion that his citation reached the desired limit of ten thousand. Sincerely yours,

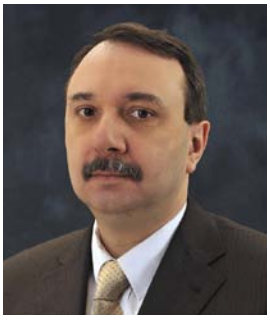

Prof. Dr. Tibor Czigány, editor

---

[*]Corresponding author, e-mail: czigany@eik.bme.hu

eXPRESS Polymer Letters Vol.8, No.1 (2014) 2–14
Available online at www.expresspolymlett.com
DOI: 10.3144/expresspolymlett.2014.2

Interactions, structure and properties in poly(lactic acid)/thermoplastic polymer blends

B. Imre[1,2], K. Renner[1,2], B. Pukánszky[1,2]*

[1]Laboratory of Plastics and Rubber Technology, Department of Physical Chemistry and Materials Science, Budapest University of Technology and Economics, H-1521 Budapest, P.O. Box 91, Hungary
[2]Institute of Materials and Environmental Chemistry, Research Centre for Natural Sciences, Hungarian Academy of Sciences, H-1525 Budapest, P.O. Box 17, Hungary

Received 5 July 2013; accepted in revised form 26 August 2013

Abstract. Blends were prepared from poly(lactic acid) (PLA) and three thermoplastics, polystyrene (PS), polycarbonate (PC) and poly(methyl methacrylate) (PMMA). Rheological and mechanical properties, structure and component interactions were determined by various methods. The results showed that the structure and properties of the blends cover a relatively wide range. All three blends have heterogeneous structure, but the size of the dispersed particles differs by an order of magnitude indicating dissimilar interactions for the corresponding pairs. Properties change accordingly, the blend containing the smallest dispersed particles has the largest tensile strength, while PLA/PS blends with the coarsest structure have the smallest. The latter blends are also very brittle. Component interactions were estimated by four different methods, the determination of the size of the dispersed particles, the calculation of the Flory-Huggins interaction parameter from solvent absorption, from solubility parameters, and by the quantitative evaluation of the composition dependence of tensile strength. All approaches led to the same result indicating strong interaction for the PLA/PMMA pair and weak for PLA and PS. A general correlation was established between interactions and the mechanical properties of the blends.

Keywords: *polymer blends and alloys, poly(lactic acid), dispersed structure, miscibility, structure-property correlations*

1. Introduction

The interest in using polymeric materials derived from renewable resources increases continuously because of the considerably improved environmental awareness of society and the fear from the depletion of petrochemical based plastics [1]. Poly(lactic acid), PLA, seems to be the polymer which exploits the most successfully this surge of demand for such materials and satisfies the requirements of large scale processing and application at the same time. PLA has several advantages, among others it can be produced from renewable resources [2] thus its application does not generate supplementary CO_2 emission [3], it is recyclable and compostable, and it has good stiffness and strength. On the other hand, this polymer has some drawbacks as well, including moisture sensitivity, fast physical ageing, poor impact resistance and relatively high price [4–6]. As a consequence, many attempts are made to modify it by plasticization [7–13], copolymerization [14–19], blending [20, 21] or by the production of composites [11–13, 22–30].

The modification of polymers by blending is a mature technology developed in the 70^{ies} or even earlier. A large number of papers and books were published on the topic [31–43], and the theoretical studies carried out mostly on commodity and engineering thermoplastics paved the way for industrial applications. The advent of biopolymers resulted in a revival of blending technology, as their several

---

[*]Corresponding author, e-mail: bimre@mail.bme.hu

disadvantages can be overcome by blending. The number of papers on the blending of biopolymers is vast, partly because of the huge number and wide diversity of these polymers and partly because of the increased interest in them. PLA and starch are the most often studied materials [36–45], but one could mention poly(3-hydroxybutyrate-co-3-hydroxyhexanoate)/poly(vinyl phenol) [46], thermoplastic phenol formaldehyde resin/poly(ε-caprolactone) (PCL) [47], poly(3-hydroxybutyrate) (PHB)/PCL [48], PLA/poly(butylene succinate) (PBS) [49, 50], poly(3-hydroxybutyrate-co-3-hydroxihexanoate)/poly (lactic acid) (PLA) [51], PHB/PLA [52], etc. without even attempting to be comprehensive. The goals of blending can range from the modification of T_g, increase of fracture resistance, flexibility or processability to the improvement of some other properties like optical characteristics or flammability.

Miscibility is often mentioned in papers dealing with the blends of bio-based and biologically degradable polymers, but rarely investigated in detail in all its various aspects. Phase diagrams and the mutual solubility of the components in each other are not determined, only the fact is established that a homogeneous or heterogeneous blend forms. The conclusion is usually based on the number of glass transition temperatures detected or on the number of phases observed on SEM micrographs. However, all polymers are partially miscible and dissolve in each other in some extent, and mutual solubility depends on interaction, which can be characterized by the Flory-Huggins interaction parameter (χ), for example. Although interactions are complicated and the parameter is rather complex consisting of various components [53], the approach is the simplest from the practical point of view and it is widely used for the estimation of miscibility [19, 54–56].

Fully degradable PLA blends may be used in agriculture and packaging, but engineering applications require more durability and longer lifetime. As a consequence, PLA is blended not only with other bio-based or biodegradable polymers, but also with commodity and/or engineering plastics [57] usually for the automotive or the electronic industry. Several commercial applications exist already for such blends [57]. The application of such materials also has environmental benefits since they improve carbon footprint considerably. However, the production of such blends with properties satisfying the intended application is possible only if the interaction of the components is controlled and miscibility-structure-property correlations are known. Accordingly, the goal of this work was to study interactions, structure and properties in the blends of PLA with three commercial thermoplastics with differing chemical structures. Polystyrene (PS), polycarbonate (PC) and poly(methyl methacrylate) (PMMA) were selected as blend components, because these thermoplastics are available in large quantities, possess excellent properties and are rated among the most common polymers applied for the production of commercially available PLA based blends [57]. Interactions were estimated quantitatively and an attempt was made to relate miscibility, structure and properties in the studied blends.

2. Experimental

The poly(lactic acid) (PLA) used in the experiments was obtained from NatureWorks LLC (Minnetonka, MN, USA). The selected grade (Ingeo 4032D, M_n = 88 500 g/mol and M_w/M_n = 1.8) is recommended for extrusion. The polymer (<2% D isomer) has a density of 1.24 g/cm^3, while its MFI is 3.9 g/10 min at 190°C and 2.16 kg load. The thermoplastics used to prepare the blends were PS (Styron 686E, Styron LLC, Berwyn, PA, USA, density: 1.05 g/cm^3, MFI: 2.5 g/10 min at 200°C, 5 kg), PC (Makrolon 2658, Bayer Material Science AG, Leverkusen, Germany, density: 1.2 g/cm^3, MFI: 13 g/10 min at 300°C, 1.2 kg) and PMMA (Oroglas HFI 7-101, Arkema Inc., King of Prussia, PA, USA, density: 1.17 g/cm^3, MFI: 10 g/10 min at 230°C, 3.8 kg). Composition changed from 0 to 100 vol% of the second component in 10 vol% steps. Before processing PLA was dried in a vacuum oven (110°C for 4 hours), while PS, PMMA and PC were dried in an air circulating oven for 2 hours at 80, 90 and 120°C, respectively.

PLA and the thermoplastics were homogenized in an internal mixer (Brabender W 50 EHT, Brabender GmbH & Co. KG, Duisburg, Germany) for 12 min at 190°C and 50 rpm. Both temperature and torque were recorded during homogenization. The melt was transferred to a Fontijne SRA 100 (Fontijne Grotnes B.V., Vlaardingen, The Netherlands) compression molding machine (190°C, 5 min) to produce 1 mm thick plates used for further testing.

One way to estimate interactions was to measure the solvent uptake of the polymers and the blends. The measurements were carried out in a desiccator by placing 20×20×1 mm compression molded specimens into the vapor of dimethyl sulfoxide (DMSO (Scharlab S.L., Barcelona, Spain) and decane (Alfa Aesar GmbH & Co KG, Karlsruhe, Germany) at 25°C as a function of time until equilibrium was reached. Flory-Huggins interaction parameters were calculated from the equilibrium solvent uptake of the samples according to a method described earlier [58]. The glass transition temperature of the blends was determined by dynamic mechanical analysis (DMA) using a Perkin Elmer Diamond DMA (PerkinElmer Inc., Massachusetts, MA, USA) apparatus. Measurements were done in tensile mode with constant amplitude (10 µm) and frequency (1 Hz) from 0 to 200°C with a heating rate of 2°C/min. The glass transition temperature of the components and the blends was determined also by scanning calorimetry on 5 mg samples at 10°C/min heating rate in two runs. Rheological measurements were carried out using an Anton-Paar Physica MCR 301 (Anton Paar GmbH, Graz, Austria) apparatus at 210°C in oscillatory mode in the frequency range of 0.1–600 1/sec on discs with 25 mm diameter and 1 mm thickness. The amplitude of the deformation was 2%. The morphology of the blends was studied by scanning electron microscopy (JEOL JSM-6380 LA, JEOL Ltd., Tokyo, Japan). Micrographs were taken from cryo-fractured surfaces. Mechanical properties were characterized by tensile testing on standard 1 mm thick ISO 527 specimens using an Instron 5566 (Instron, Norwood, MA, USA) apparatus. Stiffness (E) was determined at 0.5 mm/min cross-head speed and 50 mm gauge length. Tensile strength (σ), and elongation-at-break (ε) were calculated from force vs. deformation traces measured on the same specimens at 5 mm/min cross-head speed.

3. Results and discussion

The results are discussed in several sections. The composition dependence of properties is presented first than the structure developing during processing is discussed in the next section. A longer section is dedicated to the estimation of interactions by several methods and miscibility-structure-property interactions are discussed in the last section of the paper.

3.1. Properties

The composition dependence of blend properties is determined by the interaction of the components, structure, but also by the property itself. Modulus is less sensitive to changes in interaction and structure, while properties measured at larger deformations usually indicate quite well the interaction (compatibility) of the components. As a consequence, the study of the composition dependence of properties may offer information about the interaction of the components. Complex viscosity determined at 0.2 s^{-1} angular frequency is plotted against composition in Figure 1 for the three series of blends. The correlations offer rather dissimilar picture. The simplest is the composition dependence of PLA/PMMA blends, since the viscosity of the blends changes practically linearly between those of the two polymers. Additivity indicates good homogeneity and not too strong specific interactions between the components. Extremes in the composition dependence of viscosity are frequently claimed to indicate the strength of interaction; maxima are related to strong, while minima to poor interactions. Accordingly, the interaction of PC to PLA is expected to be stronger than that of PS. However, we must consider here other factors like the size of the dispersed droplets, their elasticity and interfacial tension, which also influence the actual value of viscosity, thus far reaching conclusions cannot be drawn about interactions from Figure 1.

The composition dependence of modulus (not shown) offers even less information, it changes almost linearly with composition for all three polymer pairs. The inherent stiffness of the three thermoplastics used in the study is close to that of PLA, it changes

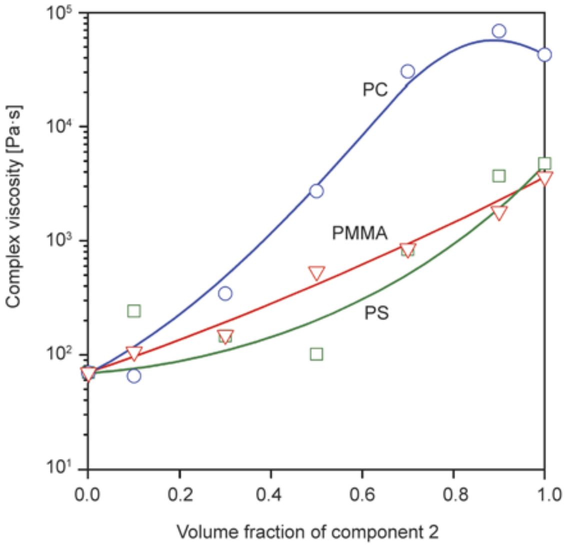

Figure 1. Composition dependence of the complex viscosity of PLA/thermoplastic polymer blends determined at 0.2 s^{-1} angular frequency; (□) PS, (○) PC, (▽) PMMA

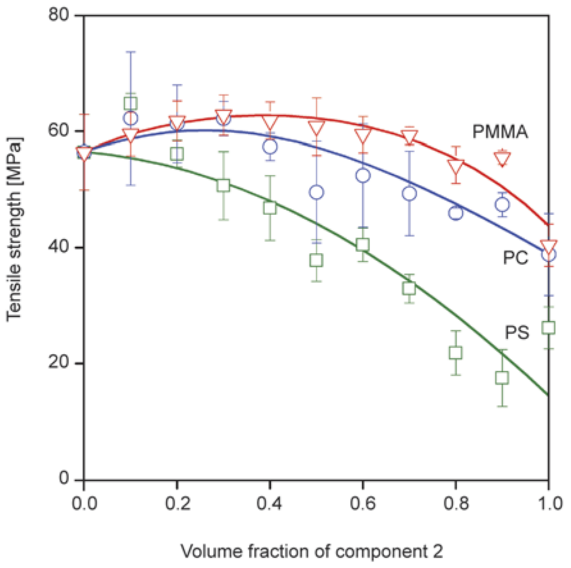

Figure 2. Tensile strength of PLA/thermoplastic polymer blends plotted against the amount of the second component; (□) PS, (○) PC, (▽) PMMA

between 2.0 and 3.1 GPa, while that of PLA is 3.2 GPa. We mentioned already, that modulus is not very sensitive to structure and interactions. The composition dependence of tensile strength shows more variation (Figure 2). The three sets of blends can be distinguished clearly, PMMA blends are the strongest, while PS blends have the smallest tensile strength; the strength of the PC blends runs in between. Such differences in the composition dependence of strength were shown to be related to interactions earlier [59, 60], thus we expect the strongest interactions to develop in PMMA while the weakest in PS blends. The deformability of the blends offers a more complex picture again. PLA/PS blends are very brittle; they fail at very small elongations (Figure 3). The elongation-at break of the PMMA blends changes continuously with composition, it is not very large, but larger than that of the PS blends. The deformability of the PC blends is interesting; it exhibits a maximum in the range of 70 and 90 vol% PC, although we have to emphasize that the standard deviation of the elongation-at-break values for PLA/PC blends is considerable in this composition range. The maximum might indicate changes in interactions, structure or deformation mechanism as a result of the presence of the PLA dispersed phase, but without the thorough analysis of micromechanical deformation processes we have to refrain from drawing further conclusions. Nevertheless, the phenomenon is definitely beneficial from the practical point of view.

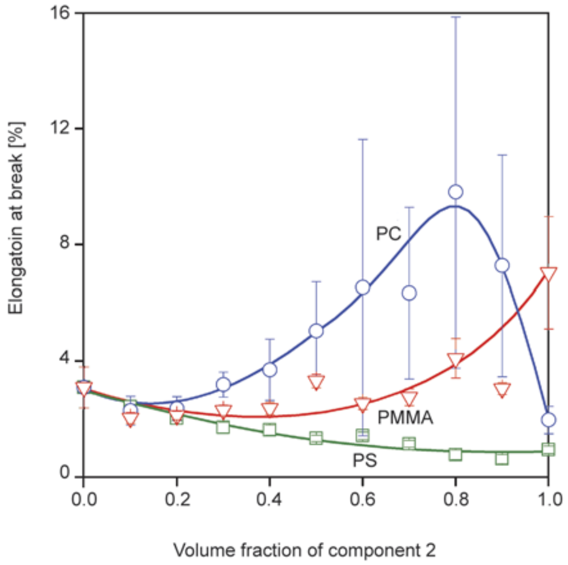

Figure 3. Effect of composition and the type of the second component on the deformability of PLA/thermoplastic polymer blends; (□) PS, (○) PC, (▽) PMMA

3.2. Structure

The structure of the blends was studied by SEM. Miscible blends are usually homogeneous and transparent [e.g. PS/poly(phenylene oxide) (PPO)]. On the other hand, immiscible blends have heterogeneous structure, very often the particles of one component are dispersed in the matrix formed by the other. However, depending on interactions particle size may change in a wide range. Weak interactions result in large particles, often in the range of 10 μm like in the blends of PP and PVC, while good interactions lead to small dispersed particles of several tenth of a micron (e.g. PVC/PMMA). Blend structure is shown as a function of composition in Figure 4 for the three series of blends. Large particles form in the PLA/PS blends and particle size shows a maximum at around 50 vol% PS content. Such large particles indicate poor interactions as indicated above. The opposite is valid for the PMMA blends. Both phases are dispersed as very small particles in the other component at the two ends of the composition range. The particles are hardly visible at the magnification used, but they are there as shown by Figure 5, in which blend structure is presented at larger magnification. At 30 vol% PMMA content small PMMA particles are dispersed in the PLA matrix. It is a little strange that a co-continuous structure cannot be distinguished even at 0.5 volume fraction of PMMA, although the small size of the particles indicate good interactions, and phase transition usually occurs in a wide composition range in such blends. The PLA/PC blends behave rather peculiarly. Large particles

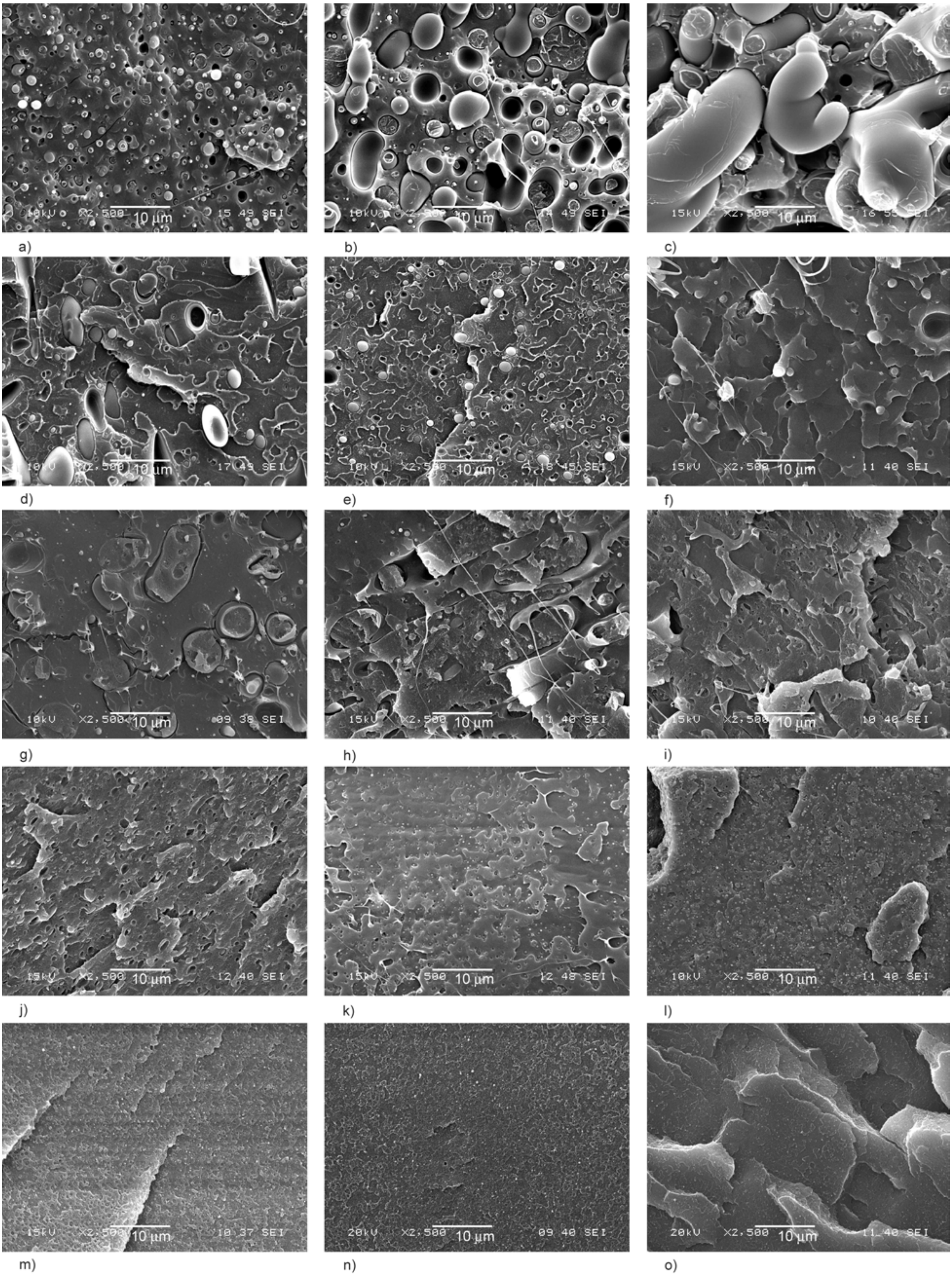

Figure 4. Changes in the morphology of PLA/thermoplastic polymer blends (a–e PLA/PS, f–j PLA/PC, k–o PLA/PMMA) with composition (0.1, 0.3, 0.5, 0.7 and 0.9 volume fraction) and component interactions

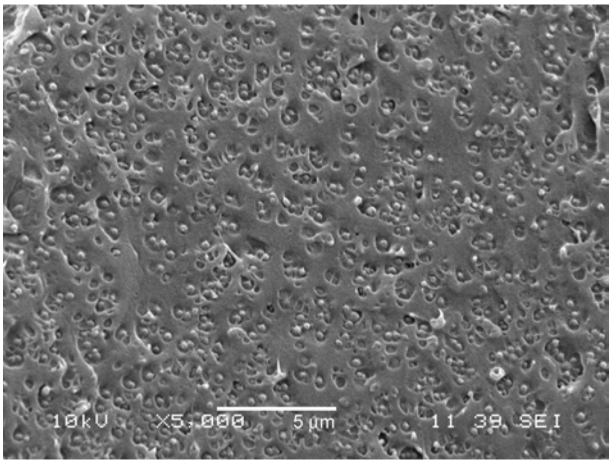

Figure 5. Dispersed structure of the PLA/PMMA blend containing 30 vol% PMMA shown in larger magnification than in Figure 4

develop at the PLA side of the composition range, while rather small ones when PC is the matrix. This might indicate different solubility of the components in each other, although we have to draw the attention here to the fact that several other factors determine particle size in polymer blends besides interfacial interactions. Component viscosity, as well as processing conditions affect morphology to a great extent. During processing, large pieces of one component are dispersed in the matrix at short mixing times, and the dominating process is particle break-up. The size of dispersed particles decreases as a function of mixing time until an equilibrium is reached between break-up and coalescence [61]. Several different models aim to describe the factors affecting this process and the final morphology [61–67]. According to them, equilibrium particle size is assumed to depend on numerous factors including composition, shear rate, the relative viscosity and interfacial tension of the components, degradation, energy required for particle break-up, coalescence probability, etc. The viscosity of PC is of several magnitudes larger than that of PLA, which might result in the formation of considerably different blend structures at the two sides of the composition range, i.e. in PLA and PC matrices, respectively, as observed in PLA/PC blends.

The particle size of the dispersed phase was determined quantitatively in the blends. The results are presented in Figure 6. The correlations reflect the qualitative analysis discussed above; relatively large particles and a maximum in the PS, very small ones in the PMMA blend and asymmetric composition dependence for the PC blends. According to these results the strongest interaction develops between PLA and PMMA, while the weakest in the PLA/PS blends.

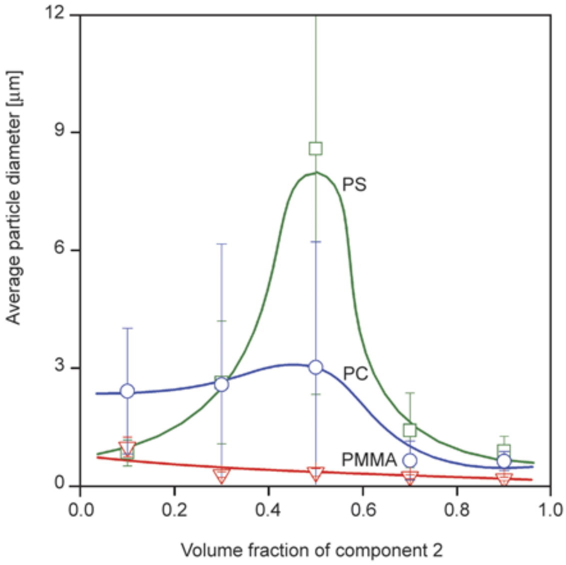

Figure 6. Differences in the size of the dispersed particles in PLA/thermoplastic polymer blends as a function of changing composition and the type of the second component; (□) PS, (○) PC, (▽) PMMA

3.3. Interactions

Interaction, compatibility and/or miscibility are usually treated very qualitatively in many of the papers published on biopolymer blends [68]. Miscibility or immiscibility is usually estimated from SEM micrographs similar to those shown in Figures 4 and 5. A more sophisticate approach is based on the determination of glass transition temperature(s). The blend is declared miscible if it possesses a single glass transition temperature between that of the components, while two T_gs are detected in immiscible blends corresponding to phases rich in the two components. The two transition temperatures shift towards each other in an extent depending on interactions and the mutual miscibility of the phases can be calculated from this shift with the method proposed by Kim and Burns [69].

T_gs determined in two of the blend series are plotted against composition in Figure 7. Both pairs show rather peculiar behavior differing from the usual. The T_g of the PLA rich phase increases steeply and continuously, while that of the phase rich in PMMA decreases with a smaller slope at least at the beginning for the PLA/PMMA blend. The two T_gs indicate heterogeneous, dispersed structure confirmed also by the SEM micrographs of Figures 4 and 5,

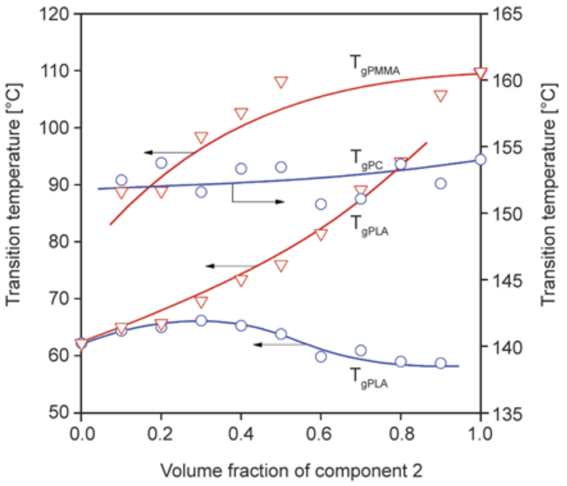

Figure 7. Effect of composition on the glass transition temperature of two series of blends; (○) PC, (▽) PMMA

while the strong composition dependence shows the development of rather strong interactions between the components. Accordingly, the mutual miscibility of the phases must be relatively large. On the other hand, the composition dependence of the two transitions appearing on the DMA traces of the PLA/PC blend is much weaker than in the PLA/PMMA blends. The T_g of the PC phase is almost constant, does not change, or changes only 1 or 2°C throughout the entire composition range. The composition dependence of the glass transition of PLA, on the other hand, is rather strange. It increases at small PC contents as expected, but decreases considerably above 0.4 volume fraction of PC. The asymmetric composition dependence of structure might be related to this decrease (see Figure 6), to the change in interaction and miscibility with composition. Nevertheless, based on these data interaction cannot be estimated quantitatively, interaction parameter or mutual miscibility is difficult or impossible to calculate by the Kim and Burns [69] approach.

Miscibility can also be estimated from component properties using the simple approach of group contributions, which yield the solubility parameter of the components, as described by Small [70], Hoy [71] and Hoftyzer and Van Krevelen [72]. We determined the solubility parameters of PLA and the thermoplastic polymers according to the method of Hoftyzer and Van Krevelen using Equations (1) to (4) [72]:

$$\delta_d = \frac{\Sigma F_{di}}{V} \tag{1}$$

$$\delta_p = \frac{\sqrt{\Sigma F_{pi}^2}}{V} \tag{2}$$

$$\delta_h = \frac{\sqrt{\Sigma E_{hi}}}{V} \tag{3}$$

$$\delta = \sqrt{\delta_d^2 + \delta_p + \delta_h^2} \tag{4}$$

where F_{di} and F_{pi} are group contributions, δ_d, δ_p, δ_h the dispersion, polar and hydrogen bonding components of solubility parameter, while δ the total solubility parameter. E_{hi} is the hydrogen bonding energy, while V refers to the molar volume of the repeating unit. The Flory-Huggins interaction parameter ($\chi_{2,3}$) can be derived from the solubility parameter of the components by using Equation (5) [58]:

$$\chi_{23} = \frac{V_r}{RT}(\delta_2 - \delta_3)^2 \tag{5}$$

where δ_2 and δ_3 are the solubility parameters of the components, V_r is a reference volume, which is the molar volume of a PLA repeating unit in our case, R the universal gas constant and T absolute temperature. The approach is very simple and has several limitations. For example, Equation (5) always yields positive values, although negative χ values also exist. Very small χ_{23} values imply good interaction. The results of the calculations are collected in Table 1 and they confirm our previous conclusions about interactions in the three series of blends.

Another approach for the quantitative estimation of interactions is the measurement of solvent absorption

Table 1. Quantities related to component interactions in PLA blends

Blend	Particle size [µm]	Solvent uptake χ	Calculated[c] χ	Tensile testing	
				Parameter B	Parameter C
PS	2.9	0.82[a]	0.32	2.38	23.3
PC	1.9	–0.35[b]	0.13	3.03	30.0
PMMA	0.4	–0.94[b]	0.08	3.23	35.3

a: based on solvent uptake measurements in DMSO vapor
b:based on solvent uptake measurements in decane vapor
c: from solubility parameters calculated according to the group contributions of Hoftyzer and Van Krevelen

in the components and the blends. The Flory-Huggins interaction parameter can be calculated from equilibrium solvent uptake by Equation (6) [58]:

$$\ln a_1 = \ln\varphi_1 + (1 - \varphi_1) + (\chi_{12}\varphi_2 + \chi_{13}\varphi_3)(1 - \varphi_1) - \chi'_{23}\varphi_2\varphi_3 \qquad (6)$$

where a_1 is the activity of the solvent, φ_1 its volume fraction in the blend at equilibrium, while χ_{12} and χ_{13} are the interaction parameters of the two-component solvent/polymer systems. χ'_{23} is related to the polymer/polymer interaction parameter by Equation (7) [73]

$$\chi'_{23} = \chi_{23}\frac{V_1}{V_2} \qquad (7)$$

where V_1 and V_2 are the molar volumes of the solvent and polymer 2, respectively. We refrain from presenting details of the absorption experiments and equilibrium solvent uptake, but in Figure 8 we show the composition dependence of the Flory-Huggins interaction parameter determined by solvent absorption for the three series of blends. The smallest and negative interaction parameters were obtained for the PLA/PMMA blend, somewhat larger, close to zero for the PC and relative large positive values for the PLA/PS blends. These results are in accordance with the particle sizes determined in the SEM study (see Figure 6) and agree well also with the strength of the blends (Figure 3).

The above conclusion and earlier experience showed that interactions and miscibility are closely related to structure and mechanical properties. A model developed earlier first for particulate filled polymers [74, 75] then adapted to blends [59, 60] allows the determination of a parameter related to interaction. According to the model the composition dependence of tensile strength can be expressed as shown by Equation (8) [75]

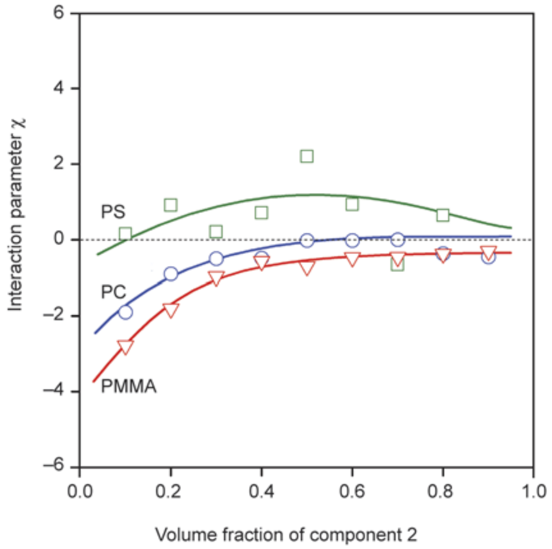

Figure 8. Composition dependence of the Flory-Huggins interaction parameter determined from solvent uptake; (□) PS, (○) PC, (▽) PMMA

$$\sigma_T = \sigma_{T_0}\lambda^n\frac{1 - \varphi_d}{1 + 2.5\varphi_d}\exp(B_T\varphi_d) \qquad (8)$$

where σ_T and σ_{T_0} are the true tensile strength ($\sigma_T = \sigma\lambda$, $\lambda = L/L_0$) of the heterogeneous polymeric system (blend or composite) and the matrix respectively, n is a parameter expressing the strain hardening characteristics of the matrix, and B is related to the load bearing capacity of the dispersed phase [59, 74, 75]. This latter is determined by interactions as well as by the inherent properties of the components as expressed by Equation (9)

$$B = \ln\left(C\frac{\sigma_{T_d}}{\sigma_{T_0}}\right) \qquad (9)$$

where σ_{T_d} is the strength of the dispersed phase, while C is related to stress transfer between the phases, i.e. interactions, and was found to correlate inversely with the Flory-Huggins interaction parameter [60].

According to the model, if we plot the natural logarithm of reduced tensile strength [$\sigma_{T_{red}} = \sigma_T(1+2.5\varphi)/\lambda^n/(1–\varphi)$] against composition we should obtain a straight line the slope of which is parameter B and from that we can easily calculate C. In Figure 9 the strength of the PLA/PC composites was plotted against composition in the way suggested by Equation (8). We obtain straight lines indeed, i.e. the approach works and C can be calculated. Naturally, we can and must draw two lines and determine two B and C values for the two sides of the composition range, since the model assumes a heterogeneous, dispersed structure. The two different B values can yield the same or very similar C values, since the inherent strength of the matrix is usually different [see Equation (9)]. Average particle size, interaction parameters determined from solvent adsorption and by the method of Hoftyzer and Van Krevelen [72], as well as average B and C values are listed in Table 1. All quantities related to component interactions agrees surprisingly well, especially if we consider the simplicity of the approaches used. All of them indicate very good

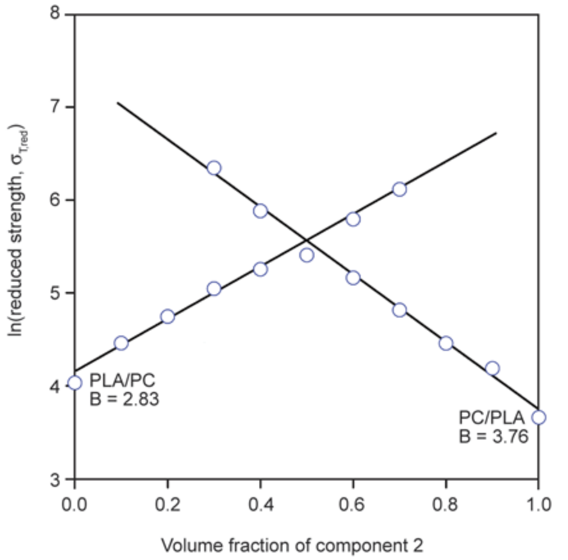

Figure 9. Determination of parameter B (see Equation (8)) for the PLA/PC blend; the calculation of the two B parameters assumes PLA (left line) and PC (right line) matrix, respectively

interactions in the PMMA, weaker in the PC and relatively poor in the PS blends.

3.4. Miscibility-structure-property correlations

The existence of the correlations mentioned in the heading of the section is an accepted fact, but quantitative relationships are not available practically at all. It is known, though, that the size of dispersed particles depends, among others, on interfacial tension which can be related to the Flory-Huggins interaction parameter [60, 62, 64, 76]. The relationship of these parameters is supported also by the results presented above and the data of Table 1. The thickness of the interphase can also be related to the interaction parameter, thus the volume of the interphase and mechanical properties as well. The relationship between mechanical properties and interaction has been demonstrated above. Stronger interactions mean smaller particles, larger interface, thicker interphase, better stress transfer and larger strength even if the structure of the blend is heterogeneous. The relationships are clear qualitatively. However, along these lines quantitative correlations can be also established as shown earlier. Following the line of thought described above inverse correlation was predicted between parameter C determined from mechanical properties and the Flory-Huggins interaction parameter. Figure 10 shows the correlation for a number of blends studied earlier [60, 75, 77]. χ was determined by solvent uptake and C determined in the way described above. The general correlation is clear and the PLA blends studied in this project fit it quite well. Data were taken from the literature for the PLA/poly(butyl succinate) (PLA/PBS) biopolymer blend and it also agrees with the rest of the results. Figure 10 proves the existence of the correlations discussed here and provides a means to predict the behavior of most polymer blends including those of biopolymers with acceptable accuracy.

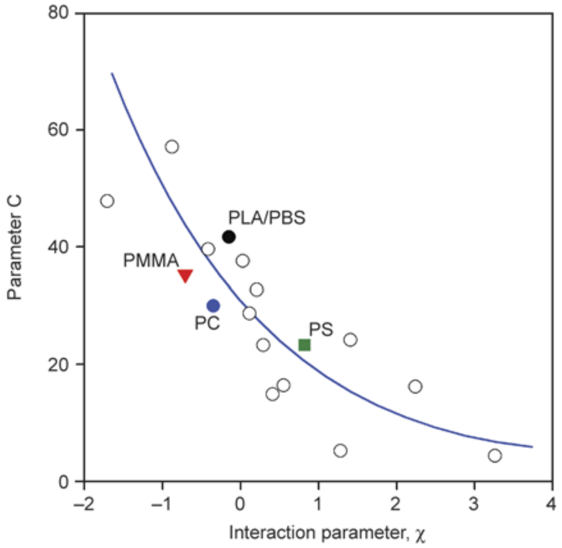

Figure 10. General correlation between component interactions (χ) and mechanical properties (parameter C) for a wide variety of blends; (○) results of earlier studies [60, 75], (●) PLA/PBS, data taken from the literature [77]

4. Conclusions

The study of PLA blends prepared with three commercial polymers having differing chemical structure showed that the structure and properties of the blends cover a wide range. All three blends have heterogeneous structure, but the size of the dispersed particles differs by an order of magnitude indicating dissimilar interactions for the corresponding pairs. Properties change accordingly, the blend containing the smallest dispersed particles has the largest tensile strength, while PLA/PS blends with the coarsest structure have the smallest. The latter blends are also very brittle. Component interactions were estimated by four different methods, the determination of the size of the dispersed particles, the calculation of the Flory-Huggins interaction parameter from solvent absorption, from solubility parameters, and by the quantitative evaluation of the composition dependence of tensile strength. All approaches led to the same result indicating strong interaction for the PLA/PMMA pair and weak for PLA and PS. A general correlation was established between interactions and the mechanical properties of the blends. The results prove that PLA/PMMA blends possess adequate property combination to use them in the automotive and electronic industry.

Acnowledgements

József Selinga is acknowledged for his help in the preparation of the blends. We are grateful for the assistance of József Hári in the preparation of the SEM micrographs. The financial support of the National Scientific Research Fund of Hungary (OTKA Grant No. K 101124) for the research on heterogeneous polymer systems is much appreciated.

References

[1] Markarian J.: Biopolymers present new market opportunities for additives in packaging. Plastics, Additives and Compounding, **10**, 22–25 (2008).
DOI: 10.1016/S1464-391X(08)70091-6

[2] Sawyer D. J.: Bioprocessing – No longer a field of dreams. Macromolecular Symposia, **201**, 271–282 (2003).
DOI: 10.1002/masy.200351130

[3] Dorgan J. R., Lehermeier H. J., Palade L-I., Cicero J.: Polylactides: Properties and prospects of an environmentally benign plastic from renewable resources. Macromolecular Symposia, **175**, 55–66 (2001).
DOI: 10.1002/1521-3900(200110)175:1<55::AID-MASY55>3.0.CO;2-K

[4] Auras R., Harte B., Selke S.: An overview of polylactides as packaging materials. Macromolecular Bioscience, **4**, 835–864 (2004).
DOI: 10.1002/mabi.200400043

[5] Kale G., Auras R., Singh S. P., Narayan R.: Biodegradability of polylactide bottles in real and simulated composting conditions. Polymer Testing, **26**, 1049–1061 (2007).
DOI: 10.1016/j.polymertesting.2007.07.006

[6] Perego G., Cella G. D.: Mechanical properties. in ‘Poly(lactic acid): Synthesis, structures, properties, processing, and applications’ (eds.: Auras R., Lim L-T., Selke S., Tsuji H.) Wiley, Hoboken, 141–153 (2010).
DOI: 10.1002/9780470649848.ch11

[7] Lemmouchi Y., Murariu M., Dos Santos A. M., Amass A. J., Schacht E., Dubois P.: Plasticization of poly(lactide) with blends of tributyl citrate and low molecular weight poly(D,L-lactide)-b-poly(ethylene glycol) copolymers. European Polymer Journal, **45**, 2839–2848 (2009).
DOI: 10.1016/j.eurpolymj.2009.07.006

[8] Pillin I., Montrelay N., Grohens Y.: Thermo-mechanical characterization of plasticized PLA: Is the miscibility the only significant factor? Polymer, **47**, 4676–4682 (2006).
DOI: 10.1016/j.polymer.2006.04.013

[9] Martin O., Avérous L.: Poly(lactic acid): Plasticization and properties of biodegradable multiphase systems. Polymer, **42**, 6209–6219 (2001).
DOI: 10.1016/S0032-3861(01)00086-6

[10] Ljungberg N., Wesslén B.: Tributyl citrate oligomers as plasticizers for poly (lactic acid): Thermo-mechanical film properties and aging. Polymer, **44**, 7679–7688 (2003).
DOI: 10.1016/j.polymer.2003.09.055

[11] Wang N., Zhang X., Ma X., Fang J.: Influence of carbon black on the properties of plasticized poly(lactic acid) composites. Polymer Degradation and Stability, **93**, 1044–1052 (2008).
DOI: 10.1016/j.polymdegradstab.2008.03.023

[12] Paul M-A., Alexandre M., Degée P., Henrist C., Rulmont A., Dubois P.: New nanocomposite materials based on plasticized poly(L-lactide) and organo-modified montmorillonites: Thermal and morphological study. Polymer, **44**, 443–450 (2003).
DOI: 10.1016/S0032-3861(02)00778-4

[13] Murariu M., Da Siva Ferreira A., Pluta M., Bonnaud L., Alexandre M., Dubois P.: Polylactide (PLA)–$CaSO_4$ composites toughened with low molecular weight and polymeric ester-like plasticizers and related performances. European Polymer Journal, **44**, 3842–3852 (2008).
DOI: 10.1016/j.eurpolymj.2008.07.055

[14] Li B., Chen S-C., Qiu Z-C., Yang K-K., Tang S-P., Yu W-J., Wang Y-Z.: Synthesis of poly(lactic acid-*b*-*p*-dioxanone) block copolymers from ring opening polymerization of *p*-dioxanone by poly(L-lactic acid) macroinitiators. Polymer Bulletin, **61**, 139–146 (2008).
DOI: 10.1007/s00289-008-0939-1

[15] Hirata M., Kimura Y.: Thermomechanical properties of stereoblock poly(lactic acid)s with different PLLA/PDLA block compositions. Polymer, **49**, 2656–2661 (2008).
DOI: 10.1016/j.polymer.2008.04.014

[16] Ho C-H., Wang C-H., Lin C-I., Lee Y-D.: Synthesis and characterization of TPO–PLA copolymer and its behavior as compatibilizer for PLA/TPO blends. Polymer, **49**, 3902–3910 (2008).
DOI: 10.1016/j.polymer.2008.06.054

[17] Mert O., Doganci E., Erbil H. Y., Dernir A. S.: Surface characterization of poly(L-lactic acid)–methoxy poly (ethylene glycol) diblock copolymers by static and dynamic contact angle measurements, FTIR, and ATR-FTIR. Langmuir, **24**, 749–757 (2008).
DOI: 10.1021/la701966d

[18] Södergård A., Stolt M.: Properties of lactic acid based polymers and their correlation with composition. Progress in Polymer Science, **27**, 1123–1163 (2002). DOI: 10.1016/S0079-6700(02)00012-6

[19] Nagahama K., Nishimura Y., Ohya Y., Ouchi T.: Impacts of stereoregularity and stereocomplex formation on physicochemical, protein adsorption and cell adhesion behaviors of star-shaped 8-arms poly(ethylene glycol)–poly(lactide) block copolymer films. Polymer, **48**, 2649–2658 (2007). DOI: 10.1016/j.polymer.2007.03.017

[20] Gu S-Y., Zhang K., Ren J., Zhan H.: Melt rheology of polylactide/poly(butylene adipate-*co*-terephthalate) blends. Carbohydrate Polymers, **74**, 79–85 (2008). DOI: 10.1016/j.carbpol.2008.01.017

[21] Rohman G., Lauprêtre F., Boileau S., Guérin P., Grande D.: Poly(D,L-lactide)/poly(methyl methacrylate) interpenetrating polymer networks: Synthesis, characterization, and use as precursors to porous polymeric materials. Polymer, **48**, 7017–7028 (2007). DOI: 10.1016/j.polymer.2007.09.044

[22] Pluta M., Jeszka J. K., Boiteux G.: Polylactide/montmorillonite nanocomposites: Structure, dielectric, viscoelastic and thermal properties. European Polymer Journal, **43**, 2819–2835 (2007). DOI: 10.1016/j.eurpolymj.2007.04.009

[23] Gorna K., Hund M., Vučak M., Gröhn F., Wegner G.: Amorphous calcium carbonate in form of spherical nanosized particles and its application as fillers for polymers. Materials Science and Engineering: A, **477**, 217–225 (2008). DOI: 10.1016/j.msea.2007.05.045

[24] Bleach N. C., Nazhat S. N., Tanner K. E., Kellomäki M., Törmälä P.: Effect of filler content on mechanical and dynamic mechanical properties of particulate biphasic calcium phosphate–polylactide composites. Biomaterials, **23**, 1579–1585 (2002). DOI: 10.1016/S0142-9612(01)00283-6

[25] Bax B., Müssig J.: Impact and tensile properties of PLA/Cordenka and PLA/flax composites. Composites Science and Technology, **68**, 1601–1607 (2008). DOI: 10.1016/j.compscitech.2008.01.004

[26] Kuan C-F., Kuan H-C., Ma C-C. M., Chen C-H.: Mechanical and electrical properties of multi-wall carbon nanotube/poly(lactic acid) composites. Journal of Physics and Chemistry of Solids, **69**, 1395–1398 (2008). DOI: 10.1016/j.jpcs.2007.10.060

[27] Murariu M., Da SilvaFerreira A., Degée P., Alexandre M., Dubois P.: Polylactide compositions. Part 1: Effect of filler content and size on mechanical properties of PLA/calcium sulfate composites. Polymer, **48**, 2613–2618 (2007). DOI: 10.1016/j.polymer.2007.02.067

[28] Pluta M., Murariu M., Da Silva Ferreira A., Alexandre M., Galeski A., Dubois P.: Polylactide compositions. II. Correlation between morphology and main properties of PLA/calcium sulfate composites. Journal of Polymer Science Part B: Polymer Physics, **45**, 2770–2780 (2007). DOI: 10.1002/polb.21277

[29] Sobkowicz M. J., Feaver J. L., Dorgan J. R.: Clean and green bioplastic composites: Comparison of calcium sulfate and carbon nanospheres in polylactide composites. CLEAN – Soil, Air, Water, **36**, 706–713 (2008). DOI: 10.1002/clen.200800076

[30] Kasuga T., Ota Y., Nogami M., Abe Y.: Preparation and mechanical properties of polylactic acid composites containing hydroxyapatite fibers. Biomaterials, **22**, 19–23 (2001). DOI: 10.1016/S0142-9612(00)00091-0

[31] Bucknall C. B.: Toughened plastics. Applied Science Publishers, London (1977).

[32] Olabisi O., Robeson L. M., Shaw M. T.: Polymer–polymer miscibility. Academic Press, New York (1979).

[33] Walsh D. J., Higgins J. S., Maconnachie A.: Polymer blends and mixtures. Martinus Nijhoff Publishers, Dordrecht (1985).

[34] Utracki L. A.: Polymer alloys and blends; Thermodynamics and rheology. Hanser, Munich (1989). DOI: 10.1002/pi.4990250214

[35] Paul D. R., Bucknall. C. B.: Polymer blends: Formulation. Wiley, New York (2000).

[36] St-Pierre N., Favis B. D., Ramsay B. A., Ramsay J. A., Verhoogt H.: Processing and characterization of thermoplastic starch/polyethylene blends. Polymer, **38**, 647–655 (1997). DOI: 10.1016/S0032-3861(97)81176-7

[37] Kim M.: Evaluation of degradability of hydroxypropylated potato starch/polyethylene blend films. Carbohydrate Polymers, **54**, 173–181 (2003). DOI: 10.1016/S0144-8617(03)00169-3

[38] Rodriguez-Gonzalez F. J., Ramsay B. A., Favis B. D.: High performance LDPE/thermoplastic starch blends: A sustainable alternative to pure polyethylene. Polymer, **44**, 1517–1526 (2003). DOI: 10.1016/S0032-3861(02)00907-2

[39] Li H., Huneault M. A.: Comparison of sorbitol and glycerol as plasticizers for thermoplastic starch in TPS/PLA blends. Journal of Applied Polymer Science, **119**, 2439–2448 (2011). DOI: 10.1002/app.32956

[40] Huneault M. A., Li H.: Morphology and properties of compatibilized polylactide/thermoplastic starch blends. Polymer, **48**, 270–280 (2007). DOI: 10.1016/j.polymer.2006.11.023

[41] Chapleau N., Huneault M. A., Li H.: Biaxial orientation of polylactide/thermoplastic starch blends. International Polymer Processing, **22**, 402–409 (2007). DOI: 10.3139/217.2070

[42] Mihai M., Huneault M. A., Favis B. D., Li H.: Extrusion foaming of semi-crystalline PLA and PLA/thermoplastic starch blends. Macromolecular Bioscience, **7**, 907–920 (2007).
DOI: 10.1002/mabi.200700080

[43] Zhang J-F., Sun X.: Mechanical properties of poly(lactic acid)/starch composites compatibilized by maleic anhydride. Biomacromolecules, **5**, 1446–1451 (2004).
DOI: 10.1021/bm0400022

[44] Wang L., Ma W., Gross R. A., McCarthy S. P.: Reactive compatibilization of biodegradable blends of poly (lactic acid) and poly(ε-caprolactone). Polymer Degradation and Stability, **59**, 161–168 (1998).
DOI: 10.1016/S0141-3910(97)00196-1

[45] Kovács J. G., Tábi T.: Examination of starch preprocess drying and water absorption of injection-molded starch-filled poly(lactic acid) products. Polymer Engineering and Science, **51**, 843–850 (2011).
DOI: 10.1002/pen.21900

[46] Cai H., Yu J., Qiu Z.: Miscibility and crystallization of biodegradable poly(3-hydroxybutyrate-*co*-3-hydroxyhexanoate)/poly(vinyl phenol) blends. Polymer Engineering and Science, **52**, 233–241 (2012).
DOI: 10.1002/pen.22069

[47] Yang J., Liu M. K., Zhang B., Chen X. D., Fu R. W., Zhang M. Q.: Intrinsic fluorescence studies of compatibility in thermoplastic phenol formaldehyde resin/poly(ε-caprolactone) blends. Express Polymer Letters, **5**, 698–707 (2011).
DOI: 10.3144/expresspolymlett.2011.68

[48] Hinüber C., Häussler L., Vogel R., Brünig H., Heinrich G., Werner C.: Hollow fibers made from a poly(3-hydroxybutyrate)/poly-ε-caprolactone blend. Express Polymer Letters, **5**, 643–652 (2011).
DOI: 10.3144/expresspolymlett.2011.62

[49] Wu D., Yuan L., Laredo E., Zhang M., Zhou W.: Interfacial properties, viscoelasticity, and thermal behaviors of poly(butylene succinate)/polylactide blend. Industrial and Engineering Chemistry Research, **51**, 2290–2298 (2012).
DOI: 10.1021/ie2022288

[50] Park J. W., Im S. S.: Phase behavior and morphology in blends of poly(L-lactic acid) and poly(butylene succinate). Journal of Applied Polymer Science, **86**, 647–655 (2002).
DOI: 10.1002/app.10923

[51] Furukawa T., Sato H., Murakami R., Zhang J. M., Noda I., Ochiai S., Ozaki Y.: Comparison of miscibility and structure of poly(3-hydroxybutyrate-*co*-3-hydroxyhexanoate)/poly(L-lactic acid) blends with those of poly(3-hydroxybutyrate)/poly(L-lactic acid) blends studied by wide angle X-ray diffraction, differential scanning calorimetry, and FTIR microspectroscopy. Polymer, **48**, 1749–1755 (2007).
DOI: 10.1016/j.polymer.2007.01.020

[52] Wasantha L. M., Gunaratne K., Shanks R. A.: Miscibility, melting, and crystallization behavior of poly(hydroxybutyrate) and poly(D,L-lactic acid) blends. Polymer Engineering and Science, **48**, 1683–1692 (2008).
DOI: 10.1002/pen.21051

[53] Tan Z. J., Vancso G. J.: Polymer-polymer interaction parameters by inverse gas chromatography: A novel molecular interpretation of nonrandom partitioning of solvent probes in polymer blends. Macromolecular Theory and Simulations, **6**, 467–478 (1997).
DOI: 10.1002/mats.1997.040060211

[54] Choe S., Cha Y-J., Lee H-S., Yoon J. S., Choi H. J.: Miscibility of poly(3-hydroxybutyrate-*co*-3-hydroxyvalerate) and poly(vinyl chloride) blends. Polymer, **36**, 4977–4982 (1995).
DOI: 10.1016/0032-3861(96)81624-7

[55] Pereira A. G. B., Gouveia R. F., de Carvalho G. M., Rubira A. F., Muniz E. C.: Polymer blends based on PEO and starch: Miscibility and spherulite growth rate evaluated through DSC and optical microscopy. Materials Science and Engineering C, **29**, 499–504 (2009).
DOI: 10.1016/j.msec.2008.09.009

[56] Zhang L. L., Goh S. H., Lee S. Y., Hee G. R.: Miscibility, melting and crystallization behavior of two bacterial polyester/poly(epichlorohydrin-*co*-ethylene oxide) blend systems. Polymer, **41**, 1429–1439 (2000).
DOI: 10.1016/S0032-3861(99)00320-1

[57] Imre B., Pukánszky B.: Compatibilization in bio-based and biodegradable polymer blends. European Polymer Journal, **49**, 1215–1233 (2013).
DOI: 10.1016/j.eurpolymj.2013.01.019

[58] Szabó P., Epacher E., Földes E., Pukánszky B.: Miscibility, structure and properties of PP/PIB blends. Materials Science and Engineering, **383**, 307–315 (2004).
DOI: 10.1016/j.msea.2004.04.035

[59] Pukánszky B., Tüdős F.: Miscibility and mechanical properties of polymer blends. Makromolekulare Chemie, Macromolecular Symposia, **38**, 221–231 (1990).
DOI: 10.1002/masy.19900380118

[60] Fekete E., Pukánszky B., Peredy Z.: Mutual correlations between parameters characterizing the miscibility, structure and mechanical properties of polymer blends. Die Angewandte Makromolakulare Chemie, **199**, 87–101 (1992).
DOI: 10.1002/apmc.1992.051990108

[61] Pukánszky B., Fortelný I., Kovář J., Tüdős F.: Particle break-up and coalescence in heterogeneous PP/EPDM blends; Effect of particle size on some mechanical properties. Plastics, Rubber and Composites Processing and Applications, **15**, 31–38 (1991).

[62] Taylor G. I.: The formation of emulsions in definable fields of flow. Proceedings of the Royal Society A, **146**, 501–523 (1934).
DOI: 10.1098/rspa.1934.0169

[63] Elmendorp J. J., Maalcke R. J.: Some microrheological aspects of polymer blending. Materials Science Monographs, **21**, 219–230 (1984).

[64] Tokita N.: Analysis of morphology formation in elastomer blends. Rubber Chemistry and Technology, **50**, 292–300 (1977).
DOI: 10.5254/1.3535144

[65] Danesi S.: Principles and technologies of polymer blending. in 'Polymer blends' (eds.: Galeski A., Martuscelli A.) Plenum Press, New York, Vol 2, 35–40 (1984).
DOI: 10.1007/978-1-4899-1831-4_3

[66] Heikens D., Barentsen W.: Particle dimensions in polystyrene/polyethylene blends as a function of their melt viscosity and of the concentration of added graft copolymer. Polymer, **18**, 69–72 (1977).
DOI: 10.1016/0032-3861(77)90264-6

[67] Fortelný I., Kovář J.: Droplet size of the minor component in the mixing of melts of immiscible polymers. European Polymer Journal, **25**, 317–319 (1989).
DOI: 10.1016/0014-3057(89)90239-5

[68] Zhang K., Ran X., Wang X., Han C., Wen X., Zhuang Y., Dong L.: Improvement in toughness and crystallization of poly(L-lactic acid) by melt blending with poly (epichlorohydrin-co-ethylene oxide). Polymer Engineering and Science, **51**, 2370–2380 (2011).
DOI: 10.1002/pen.22009

[69] Kim W. N., Burns C. M.: Blends of polycarbonate and poly(methyl methacrylate) and the determination of the polymer-polymer interaction parameter of the two polymers. Macromolecules, **20**, 1876–1882 (1987).

[70] Small P. A.: Some factors affecting the solubility of polymers. Journal of Applied Chemistry, **3**, 71–80 (1953).
DOI: 10.1002/jctb.5010030205

[71] Hoy K. L.: New values of the solubility parameters from vapor pressure data. Journal of Paint Technology, **42**, 76–118 (1970).

[72] Hoftyzer P. J., Van Krevelen D. W.: Cohesive properties and solubility. in 'Properties of polymers' (ed.: Van Krevelen D. W.) Elsevier, New York, 152–155 (1976).

[73] Hopfenberg H. B., Paul D. R.: Transport phenomena in polymer blends. in 'Polymer blends' (eds.: Paul D. R., Newman S.) Academic Press, New York, Vol. 1, 445–489 (1978).

[74] Pukánszky B., Turcsányi B., Tüdős F.: Effect of interfacial interaction on the tensile yield stress of polymer composites. in 'Interfaces in polymer, ceramic, and metal matrix composites' (ed.: Ishida H.) Elsevier, New York, 467–477 (1988).

[75] Pukánszky B.: Influence of interface interaction on the ultimate tensile properties of polymer composites. Composites, **21**, 255–262 (1990).
DOI: 10.1016/0010-4361(90)90240-W

[76] Fortelný I., Kamenická P., Kovář J.: Effect of the viscosity of components on the phase structure and impact strength of polypropylene/ethylene-propylene elastomer blends. Die Angewandte Markomolekulare Chemie, **164**, 125–141 (1988).
DOI: 10.1002/apmc.1988.051640110

[77] Bhatia A., Gupta R., Bhattacharya S. N., Choi H. J.: Compatibility of biodegradable poly (lactic acid) (PLA) and poly (butylene succinate) (PBS) blends for packaging application. Korea – Australia Rheology Journal, **19**, 125–131 (2007).

eXPRESS Polymer Letters Vol.8, No.1 (2014) 15–29
Available online at www.expresspolymlett.com
DOI: 10.3144/expresspolymlett.2014.3

Influence of selective dispersion of MWCNT on electrical percolation of *in-situ* polymerized high-impact polystyrene/MWCNT nanocomposites

N. K. Shrivastava, S. Maiti, S. Suin, B. B. Khatua[*]

Materials Science Centre, Indian Institute of Technology, Kharagpur, Kharagpur-721302, India

Received 3 July 2013; accepted in revised form 28 August 2013

Abstract. This work demonstrates a simple method to develop highly conducting high impact polystyrene (HIPS)/multiwall carbon nanotube (MWCNT) nanocomposites through selective dispersion of MWCNT in HIPS matrix. The method involves *in-situ* polymerization of polybutadiene containing styrene monomer in the presence of HIPS beads and MWCNT. A significantly lower percolation threshold value than ever reported for HIPS/MWCNT systems was obtained using unmodified unaligned MWCNTs. With the increase in HIPS bead content (at a particular MWCNT loading) in the HIPS/MWCNT nanocomposites, the conductivity value was increased, suggesting that the presence of HIPS beads acted as excluded volume that decreased the percolation threshold. An increase in electrical conductivity from $1.91\cdot10^{-7}$ to $1.15\cdot10^{-5}$ S/cm was evident, when the HIPS bead content was increased from 30 to 60 wt% at a constant loading of MWCNT (i.e. 0.6 wt%). The morphological investigation of the HIPS/MWCNT nanocomposites revealed that, the MWCNTs were selectively dispersed in the *in-situ* polymerized HIPS region, outside the HIPS beads, which resulted in the lowering of the percolation threshold to a lower value of 0.54 wt%. The morphology and electrical properties of the nanocomposites have been discussed in detail in the manuscript.

Keywords: *nanocomposites, HIPS, percolation threshold, conductivity*

1. Introduction

The conducting polymer composites, prepared through the incorporation of conducting filler into an insulating polymer matrix has become a field of growing interest for the last few decades, due to its immense applications in various fields, such as, electronics, aerospace, military, flexible electronics, electromagnetic interference (EMI) shielding, electrostatic dissipation and sensors [1, 2]. The conducting behavior in the insulating polymer can be imposed by the incorporation of various conducting fillers such as carbon fibers [3], carbon black (CB) [4, 5], metallic fillers [6, 7] and carbon nanotubes (CNTs) [8, 9]. The electrical and dielectric properties of polymer/conducting filler composites depend mainly on the filler type, aspect ratio, size, filler loading and the state of dispersion of the filler.

A considerable amount of research effort has been devoted to develop polymer/CNT nanocomposites in the recent years due to the superior conductivity of CNTs over other conducting fillers, such as, CB [10–12]. Thus, a very high conductivity in the polymer/CNT nanocomposites can be achieved at very low loadings of CNTs. The efficient dispersion of CNT into the polymer matrix is very difficult to achieve due to the high van der Waals forces between the individual CNT [13]. The small size and large surface area of the CNT lead to such high van der

---

[*]Corresponding author, e-mail: khatuabb@matsc.iitkgp.ernet.in

Waals forces of attraction, which restricts the dispersion of CNTs in polymer matrices. Hence, to achieve good dispersion of CNTs into polymer matrix, surface modification or functionalization of CNTs is carried out, which results in better adhesion of filler with the host polymer [14]. However, this sort of modification increases the surface defects of CNT, resulting in a decrease in its inherent conductivity [15, 16].

Various thermoplastics such as poly(methyl methacrylate) (PMMA) [17], polystyrene (PS) [18], polyethylene (PE) [19], polycarbonate (PC) [20], and others [21, 22] have been reported in the literature for the development of conducting polymer nanocomposites based on CNT. Among these, PS/CNT nanocomposites have extensively been studied in the previous reports. However, very little stress has been put on the other co-polymers of PS, such as, high impact polystyrene (HIPS). A few researchers have worked on co-polymers of PS. For instance, McClory *et al*. [23] studied the electrical conductivity of melt mixed HIPS/MWCNT nanocomposites and found an electrical conductivity of ~10^{-6} S/cm at 4 wt% loading of MWCNT in HIPS. Lee *et al*. [24] and Göldel *et al*. [25] studied the electrical properties of melt extruded SAN/MWCNT nanocomposites and found $\approx 4\cdot10^{-4}$ and $\approx 1\cdot10^{-4}$ S/cm at 2 and 1.5 wt% MWCNT loadings, respectively. A DC conductivity of $\approx 10^{-2}$ S/cm at 15 wt% of CNT loading in poly (styrene-co-butyl acrylate)/MWCNT nanocomposites was reported by Dufresne *et al*. [26]. Singh *et al*. [27] reported an electrical conductivity value of $\approx 1.27\cdot10^{-6}$ S/cm in (80/20 w/w) ABS/PS blend at 0.64 wt% MWCNT loading.

A considerable research effort has been given towards the development of new methodology to reduce the percolation threshold of CNT in polymer matrix. Zhao *et al*. [28] reported the percolation threshold at 0.07 wt% of MWCNT in poly vinylidene fluoride (PVDF) by coating the PVDF spherical particles with MWCNTs through sonication. Mu *et al*. [29] developed a contiguous, cellular structure of SWCNT using SWCNT coated PS pellets followed by hot pressing. This method reduced the electrical percolation threshold compared to the composites with well-dispersed SWCNT. Liu and Grunlan [30] used nanoclay for inducing network of SWCNT in an epoxy matrix. They could reduce the percolation of SWCNT from 0.05 to 0.01 wt% by adding a small amount of clay. In summary, reports on PS and its copolymers indicate that, it is difficult to disperse the CNT in polymer matrix due to the inherent high melt viscosity of the base polymers. In order to avoid this, a solvent casting process can be used, which is again disadvantageous due to the presence of residual traces of solvent in the nanocomposites, and thus should be avoided. Moreover, the percolation threshold can be reduced to an exceptionally lower value through selective dispersion of MWCNT in the base matrix.

In the present study, we report a cost effective, straightforward method that involves selective dispersions of MWCNT in a continuous 3D network via exclusion of some volume of the base matrix. This method involves the polymerization of styrene in the presence of polybutadiene rubber followed by the introduction of the HIPS beads during the polymerization process. These beads can be considered as an ‘excluded volume’ in the nanocomposites which cannot take part in the generation of conductivity.

2. Experimental

2.1. Materials details

Synthesis grade styrene monomer, used in this study, was procured from Merck, Germany. Benzoyl peroxide (BPO) used as polymerization initiator, was purchased from Sigma-Aldrich Inc USA. Non cross-linked polybutadiene rubber (BR) (Buna CB 550 T) was supplied by LANXESS India Pvt. Ltd., Kolkata. General purpose high impact polystyrene (HIPS) copolymer was of commercial grade (grade SH-03;styrene with 1,3 butadiene polymer; styrene content ≈88% w/w, specific gravity 1.03–1.05 at 25°C; MFI ≈8.5 g/10 min at 200°C/5 kg; average diameter of pellets ≈2.35 mm and length ≈2.70 mm) was supplied by Supreme Petrochem Limited India. The MWCNT was industrial grade (NC 7000 series) supplied by Nanocyl S.A., Belgium. The MWCNT has an average diameter of 9.5 mm and length 1.5 µm, surface area 250~300 m^2/g, and 90% carbon purity. The MWCNT was used without any further chemical modification.

2.2. Preparation of HIPS/MWCNT nanocomposites

Styrene monomers were used after washing with 100 mL of 5 wt% aqueous NaOH solution for polymerization. Desired amount (0.29 g) of MWCNT was dispersed in 40 mL purified styrene monomer by ultrasonication for 2 h at room temperature. Then 4.32 gm of butadiene rubber (BR) was dissolved in same styrene/MWCNT mixture. The styrene/BR/MWCNT mixture was transferred to a specially designed 250 mL three-neck round-bottom flask with open head (like 6947 kettle, Borosil) connected with a condenser, a thermometer, and nitrogen gas inlet/outlet. Under magnetic stirring, required amount (1 wt%) of the BPO, as polymerization initiator, was added to the styrene/BR/MWCNT mixture. The reactor temperature was gradually increased to ≈85°C under constant stirring. During the progress of polymerization reaction (after ≈45 min of the reaction when styrene/BR/MWCNT mixture started developing very high viscosity), 23.45 g of commercial HIPS bead was added into the reactor. The reaction was continued for 5 h under nitrogen atmosphere with constant temperature and stirring. The HIPS/MWCNT nanocomposites thus obtained through *in-situ* bulk polymerization of HIPS/MWCNT in presence of polymer beads was air dried and finally dried in hot air oven at 60°C for 24 h. From the weight of the final product, the calculated loadings of CNT and HIPS bead in the HIPS/MWCNT nanocomposites were 0.5 and 40 wt%, respectively. The HIPS/MWCNT nanocomposites with higher CNT loading (0.7 and 1 wt%) and higher amount of polymer bead (50, 60, and 70 wt%) were also prepared through the same polymerization route, by varying the amounts of styrene, MWCNT and the HIPS bead during the polymerization reaction.The schematic representation for the preparation of the nanocomposites is illustrated in Figure 1.

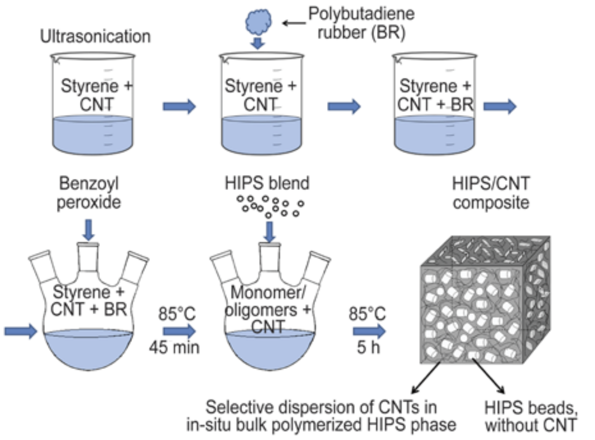

Figure 1. Schematic representation of the nanocomposites manufacturing process

2.3. Molding of the HIPS/MWCNT nanocomposites

Nanocomposites with various compositions of HIPS bead and MWCNT were compression molded at 210°C under constant pressure of 10 MPa/cm^2. The molded parts were cooled naturally to room temperature and used for further characterization. Bulk polymerized HIPS having relatively low molecular weight and low melt viscosity (high MFI value) than the commercial HIPS bead is expected to flow easily inside the mold and thus, form the matrix phase though the content of HIPS bead is more in the nanocomposites.

2.4. Characterization

2.4.1. Electrical conductivity

Keithley sourcemeter Model 4200 (Keithley Instruments Inc., USA) with two-probe setup was used to measure the resistance (R) by current-voltage (I-V) measurement. DC conductivity was calculated by putting the values of I-V measurement in Equation (1). The I-V measurement was carried out in the range of +1 to –1 V. Each sample was tested for five times and the average was reported:

$$\sigma_{\mathrm{DC}} = \frac{IL}{VA} \tag{1}$$

where σ_{DC} is DC conductivity I and V are current and voltage, respectively. L and A represent the length and cross section area of the sample. Compression molded specimen with dimensions 30×10×3 mm^3 were used for measurements. Before measurements, both sides of the nanocomposite were coated with silver paste. After that, both positive and negative electrode was put onto opposite sides of the sample.

The AC electrical conductivity of the nanocomposites (disc type sample with thickness 0.3 cm and area $1.88\cdot10^{-1}$ cm^2) was determined using a computer controlled impedance analyzer (HIOKI 3532-50 LCR HiTESTER) on application of an alternating electric field across the sample cell in the frequency region of 42 Hz to 5 MHz. The parameters such as dielectric constant (ε') and dielectric loss (ε'') were found as a function of the frequency. The AC conductivity (σ_{AC}) was calculated from the dielectric data using Equation (2):

$$\sigma_{\mathrm{AC}} = \omega\varepsilon_0\varepsilon'\tan\delta \qquad (2)$$

where $\omega = 2\pi f$ (f is the frequency), and ε_0 is the dielectric constant of the vacuum. The ratio of the imaginary to the real parts ($\varepsilon''/\varepsilon'$), known as the dissipation factor, is represented by $\tan\delta$, where δ is the angle between the voltage and the charging current. The dielectric constant (ε') was determined by Equation (3):

$$\varepsilon' = \frac{C_{\mathrm{p}}}{C_0} \qquad (3)$$

where C_{p} is the capacitance of the sample (in parallel mode) C_0 is the capacitance of the cell. The value of C_0 was calculated using the Equation (4):

$$C_0 = \frac{\varepsilon_0 A}{d} \qquad (4)$$

where A and d is the area and thickness of the sample respectively. C_{p} and $\tan\delta$ were obtained directly from the machine.

2.4.2. Optical microscopy

The distribution of MWCNT in the HIPS matrix was investigated by a high resolution optical microscope (HROM, Carl Zeiss Vision GmbH, Germany). The surface images were taken using a monochromatic light at different resolutions.

2.4.3. Field emission scanning electron microscope (FESEM) study

The phase morphology of the HIPS/MWCNT nanocomposites was studied by employing a field emission scanning electron microscope (FESEM, Carl Zeiss-SUPRA™ 40 Germany), operated at an accelerating voltage of 100 kV. The samples were broken under liquid nitrogen atmosphere and cryo-fractured surface was coated with a thin layer of gold to avoid electrical charging.

2.4.4. Transmission electron microscopy (TEM) analysis

A high resolution transmission electron microscope (HRTEM, JEM-2100, JEOL, Japan) was used to study the dispersion of the MWCNT in the HIPS matrix, operating at an accelerating voltage of 200 kV. The HIPS/MWCNT nanocomposites sample was ultra-microtomed at –50°C with a thickness of 100 nm. Since the CNT has much higher electron density than the polymers, no staining was required and it appeared darker in the TEM images.

3. Results and discussion

3.1. Morphology

The morphological analysis of the nanocomposite was done by capturing the optical micrographs and the findings were finally verified through the FESEM and TEM analysis. The optical micrograph, TEM image, FESEM image of the nanocomposites with 0.6 wt% MWCNT loading in the presence of 60 wt% HIPS beads are represented in Figure 2a–2f, respectively. As can be seen, the optical micrograph shows two distinct regions; a dispersed light region and relatively a dark continuous region (Figure 2a and 2b). An in depth analysis of the microstructure was done through the FESEM analysis. As observed, the CNTs were selectively concentrated in the continuous dark region while the remaining parts (dispersed light regions) were devoid of the considerable amount of CNT. From the above results we postulate that the CNT-rich continuous dark region is the bulk copolymerized HIPS phase, while the lighter region dispersed in the dark phase are the HIPS beads devoid of any CNT, as shown in the FESEM images. This consideration is reasonable due to the fact that when the HIPS beads were added to the reaction mixture, the polymerization has already progressed to the oligomeric stage. At this stage, it is difficult for the HIPS beads to swell as there was almost no monomer available in the reaction medium.Thus, we can conclude that the nanocomposites consist of two phases: one containing the bulk copolymerized HIPS along with the CNT while the other possessing the HIPS beads with discernible amount of CNT covering the surface.

The TEM images of the nanocomposites are represented in Figure 2e (low magnification) and 2f (high magnification). The presence of CNTs in selective regions was evident from the TEM image, supporting the result obtained from FESEM analysis. A better dispersion of the CNT in the selected regions of the matrix phase can easily be observed from the high magnification TEM micrograph. Moreover, the high magnification TEM image shows the clear separation between the individual CNTs, as was previously seen in the FESEM image. However, it was impossible to capture millimeter scale dimension HIPS beads in a single image; hence a portion

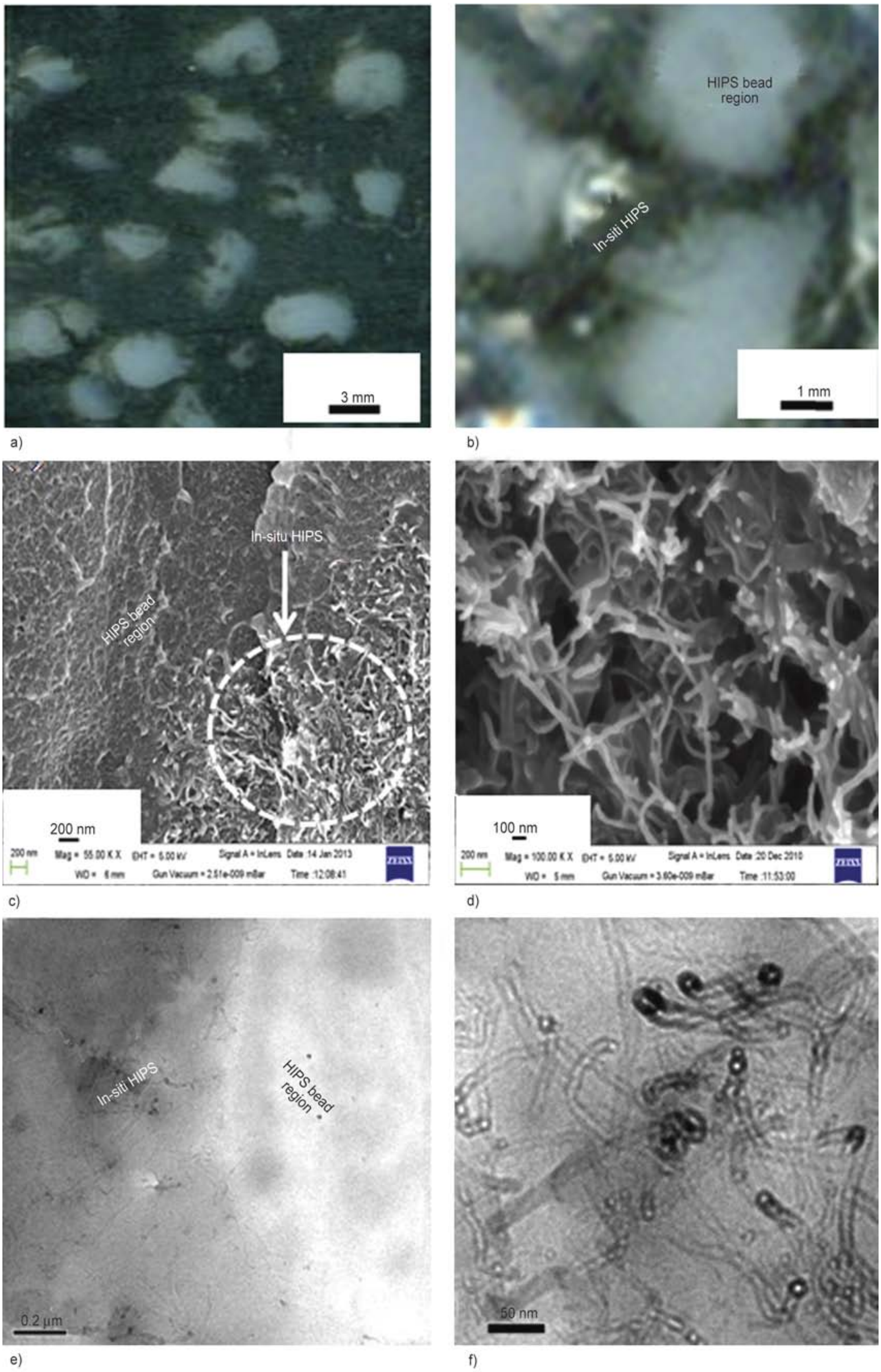

Figure 2. (a) low magnification (b) and high magnification optical micrograph, (c) low magnification and (d) high magnification FESEM micrograph, (e) low magnification and (f) high magnification TEM micrographs of 0.6 wt% MWCNT 60 wt% HIPS bead containing nanocomposites

of the beads could be captured. In both the low and high magnification images no clear phase separation was observed, as both the regions contained the same polymer. From the morphological analysis it can be concluded that, the CNT forms a continuous network structure in the *in-situ* copolymerized HIPS regions, leaving the HIPS beads free of any CNT dispersion. This CNT free region acts as 'excluded volume' with negligible penetration of the CNT into the bead region that enhanced an effective concentration of the CNT in the nanocomposites. This facilitates the probability of the formation of more number of conducting paths throughout the nanocomposites.

3.2. Electrical properties

Figure 3 shows the effect of HIPS beads on the electrical conductivity of HIPS/MWCNT composite at room temperature. The conductivity of the composite increases with increasing the bead loading up to 60 wt%. It is noteworthy that the electrical conductivity of the composite containing 0.6 wt% of MWCNT and without any bead does not show any considerable change in electrical conductivity in comparison to pure HIPS (i.e. $\approx 10^{-11}$ S/cm). Surprisingly, addition of 30 wt% HIPS bead in nanocomposites at the same concentration of CNT loading shows a DC electrical conductivity of $1.91 \cdot 10^{-7}$ S/cm. We hypothesized that the effective concentration of the MWCNT increases in the *in-situ* copolymerized matrix phase of the composite in the presence of HIPS beads. It is considered that HIPS bead plays the role of the excluded volume in the nanocomposite where MWCNT fails to penetrate. Therefore *in-situ* copolymerized HIPS/HIPS beads nanocomposite (40/60 w/w) with 0.6 wt% MWCNT loading in which theoretically calculated effective concentration of the MWCNT in *in-situ* polymerized phase is found to be 1.5 wt% (assuming all the CNT present in *in-situ* copolymerized HIPS phase). So it is expected that the composite, with 1.5 wt% CNT loaded (without any HIPS bead) should exhibit comparable conductivity with composite containing 0.6 wt% MWCNT and 60 wt% HIPS bead.

To explore this assumption 1.5 wt% MWCNT loaded *in-situ* copolymerization HIPS without any bead was prepared and DC conductivity was found $8.76 \cdot 10^{-6}$ S/cm. It was found that the conductivity of 0.6 wt% MWCNT and 60 wt% HIPS bead loaded composite shows higher conductivity ($1.15 \cdot 10^{-5}$ S/cm) than the composite containing 1.5 wt% MWCNT without any HIPS bead. This means that the effective concentration of the CNT in the polymerized phase of the bead containing composite is actually more than the calculated theoretical CNT concentration of 1.5 wt%.

This increment of the conductivity may be due to diffusion of some styrene monomer and oligomer of CNT containing region to the HIPS bead which is evident by the swelling of the HIPS bead while mixing. Thus, a small reduction of the bulk polymerized HIPS in CNT containing region will occur which leads to the increment of the effective concentration of the CNT in polymerized HIPS phase.

Further, to verify this phenomenon we prepared a composite with small size HIPS bead (HIPS-s). Figure 3b compares the electrical conductivity of the HIPS/MWCNT nanocomposites in the presence of HIPS bead and HIPS-s bead. Since diffusion (penetration of styrene monomer inside HIPS bead) is

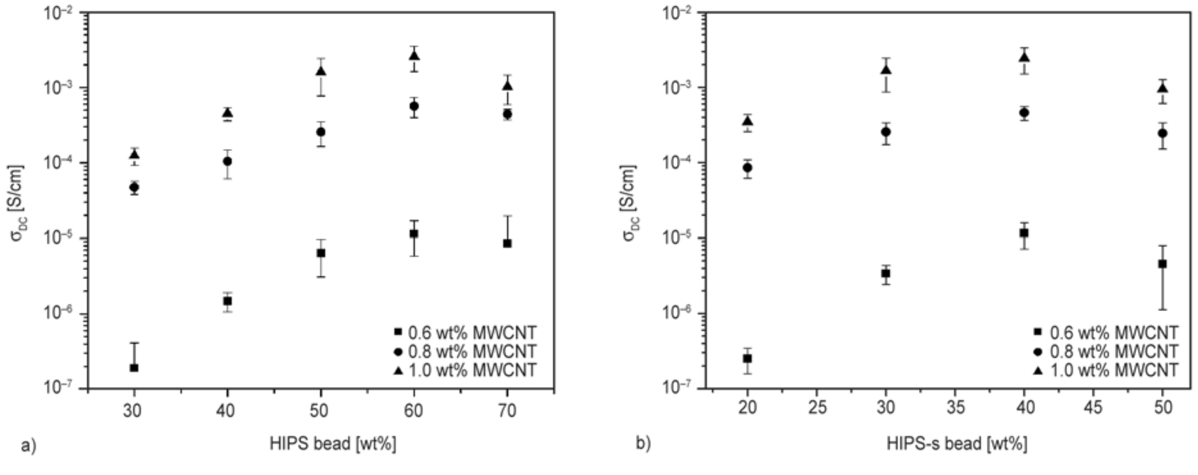

Figure 3. DC Conductivity of HIPS/MWCNT nanocomposites with the weight % of (a) HIPS bead, and (b) micron-sized HIPS-s bead, in the HIPS matrix at various MWCNT loadings

directly proportional to the available surface area of the beads, these HIPS-s beads (diameter ≈200 μm) with high surface area will influence more diffusion of small molecule from *in-situ* polymerized region to bead and thus would cause an increment in conductivity. Interestingly, we found that 0.6 wt% MWCNT and 50 wt% HIPS-s bead loaded composite shows DC conductivity of $1.37\cdot10^{-5}$ S/cm, which is much higher than the conductivity ($6.43\cdot10^{-6}$ S/cm) observed in the composite with 50 wt% HIPS bead with similar MWCNT (0.6 wt%) loading. When we increase the loading of HIPS-s bead beyond 50 wt%, DC conductivity of nanocomposite starts decreasing. This may be due to the fusing of HIPS-s bead with each other that makes non-conducting matrix phase. The composite with 40 wt% HIPS-s bead and 0.6 wt% CNT loaded nanocomposite showed a DC conductivity of $\approx2.27\cdot10^{-5}$ S/cm, on the other hand 60 wt% HIPS bead loaded composite shows $1.15\cdot10^{-6}$ S/cm quite similar range of DC conductivity.

Figure 4 shows the DC conductivity of 60 wt% HIPS beads containing composite with increasing MWCNT loading. DC conductivity of the composites sharply increases by several orders of magnitude from 10^{-11} to 10^{-4} S/cm by varying the CNT loading from 0.2–0.6 wt%. This drastic increase in conductivity is well known as percolation phenomena which indicate the formation of the continuous network structure of MWCNT throughout the nanocomposites. While increasing the CNT loading beyond 0.6 wt%, conductivity of nanocomposites increases slowly. The conductivity of HIPS/MWCNT nanocomposites with 60 wt% HIPS bead increased from $1.15\cdot10^{-5}$ to $2.06\cdot10^{-2}$ S/cm when the CNT loading in the nanocomposites was increased from 0.6 to 1.5 wt%.

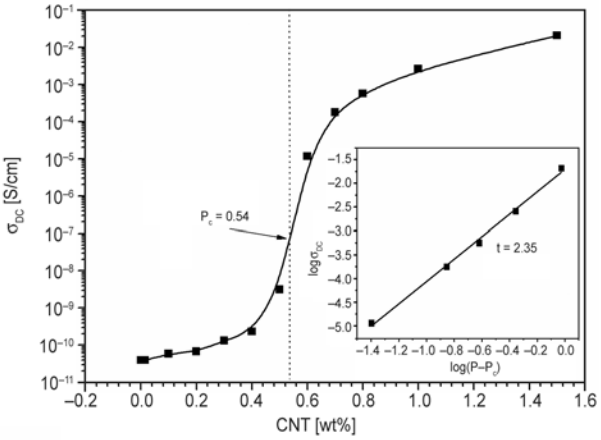

Figure 4. DC Conductivity of HIPS/MWCNT nanocomposites with MWCNT loading at constant 60 wt% HIPS bead loading. The Inset: log-log plot for σ_{DC} vs (P–P_c) for the same nanocomposites. The straight line in the inset is a least-square fit to the data using Equation (4) returning the best fit values $P_c = 0.54\%$ and $t = 2.35$.

In a composite system where the matrix is an insulator and filler is a conducting material as in the case of polymer/CNT nanocomposites, several theories can be predicted for percolation of the system.The most acceptable relation between the DC conductivity, concentration of nanofiller (P) and percolation threshold concentration (P_c) can be written as the scaling (power) law equation (Equation (5) and (6)). To estimate the P_c value, experimental data of DC conductivity were linear fitted by using scaling law [31, 32]:

$$\sigma_{DC} \propto (P - P_c)^t \text{ for } P > P_c \tag{5}$$

$$\sigma_{DC} \propto (P - P_c)^{-s} \text{ for } P < P_c \tag{6}$$

Where σ_{DC} is the DC conductivity of the nanocomposites, s and t are the critical exponent. Inset of Figure 3 shows the best linear fitted data considering the value of $P_c \approx 0.54$ wt%. This value of P_c gives an excellent fit with least error where P_c value varied from 0.2~0.6. In the same Figure (inset of Figure 3), slope of the fitted straight line represents the critical exponent (t) which was found to be $\approx2.5\pm0.13$ and calculated y-intercept is –1.7. This exponent data give excellent fit and shows agreements with Equation (5) and (6) and resembles extremely low percolation threshold at 0.54 wt% of CNT in the HIPS matrix. Percolation theory suggests that for three dimensional (3D) percolation network value of the critical exponent t, should be greater than 2. In our case the value of $t \approx 2.5$ well agrees with the theoretical value and indicates the presence of 3D percolation network over the nanocomposites [33, 34]. According to 3D percolation theory, the value of the critical exponent lowers than 2 shows the presence of more dead arm in the conducting network. The value of critical exponent not only depends on the type of polymer or CNT but also, on the method of nanocomposites preparation. Kota *et al.* [35] used two different solvent namely DMF and THF for preparing PS/MWCNT nanocomposites and found two different t values of 1.5 and 1.9, respectively. In the literature there are large variances reported for systems containing different polymers such as, $t = 1.8$ for epoxy/MWCNT [36], $t = 3.8$ for polycarbonate/MWCNT [37], $t = 2.3$ for PMMA/MWCNT [38] nanocomposites. The critical exponent value mainly depends on the aspect ratio of CNT, carbon purity of CNT, a type of polymer and CNT dispersion method. Out of those factors only dispersion method can be moderate. In our work this extremely ultra-low percolation threshold value indicates excellent dispersion of high aspect ratio MWCNT in the matrix polymer. Balberget *et al*. [39] proposed a general relationship between the aspect ratio of filler and percolation threshold. This relationship is considered with an assumption that the fillers are randomly distributed and fillers have sticks like structure with a length (L) and diameter (D), and thus represents as shown by Equation (7):

$$\frac{L}{D} = \frac{3}{P_c} \tag{7}$$

where P_c is the percolation threshold and L/D is the aspect ratio of the filler. By this relation we can estimate the average aspect ratio of CNT bundles. This CNT has a natural tendency to agglomeration and become a bundle like arrangement in the composite. These bundles are responsible for the development of electrical conductivity in the composite. The size of those bundles indicated the dispersion level of the nanofiller in polymer matrix. The average aspect ratio of MWCNT in this study is 150 ($L = 1.3$ μm, $D = 9.5$ nm, data given by the manufacturer) that gives the P_c value ≈ 0.02. However, we found the value of $P_c \approx 0.54$. In our case, the calculated (from Equation (7)) theoretical aspect ratio of CNT bundles is ~5.66. This analysis unambiguously shows that the conductivity in the composite is due to MWCNT bundle, and not because of individual CNT. However these bundles also have a high aspect ratio, and thus, tend to reduce the percolation threshold of the nanocomposite.

On the other hand, considering y intercept of fitted line in Figure 4 (Inset), the 100 wt% loading of filler (extrapolation value of $P \rightarrow 100$) gives the DC conductivity value $1.99\cdot10^{-2}$ S/cm. This value is far lower than the conductivity (50 S/cm) expected for the pure MWCNT [40, 41]. A decrease in conductivity of CNT is associated with the tunneling barrier between CNTs. The tunneling barrier is mainly depends on the type of polymer and fabrication process of nanocomposites.

To verify the tunneling as exact mechanism behind the conduction in HIPS/CNT nanocomposites, the temperature dependence behavior of the DC conductivity was studied. Figure 5a depicts the temperature dependence of DC conductivity of the nanocomposites having $P > P_c$ at a temperature range of 20–80°C. As observed, the increment in DC conductivity is very less with increase in temperature. A nonmetallic behavior of DC conductivity was evident in the nanocomposites in the investigated temperature range. The Figure 5a also shows the temperature dependence of DC conductivity does not depend on the CNT content, and thus, it can be reasonably assumed that the conduction at room temperature is controlled here by the connectivity of the conductive network. For disordered materials, a theoretical expression can be obtained for tunneling conductivity in the nanocomposites consisting of

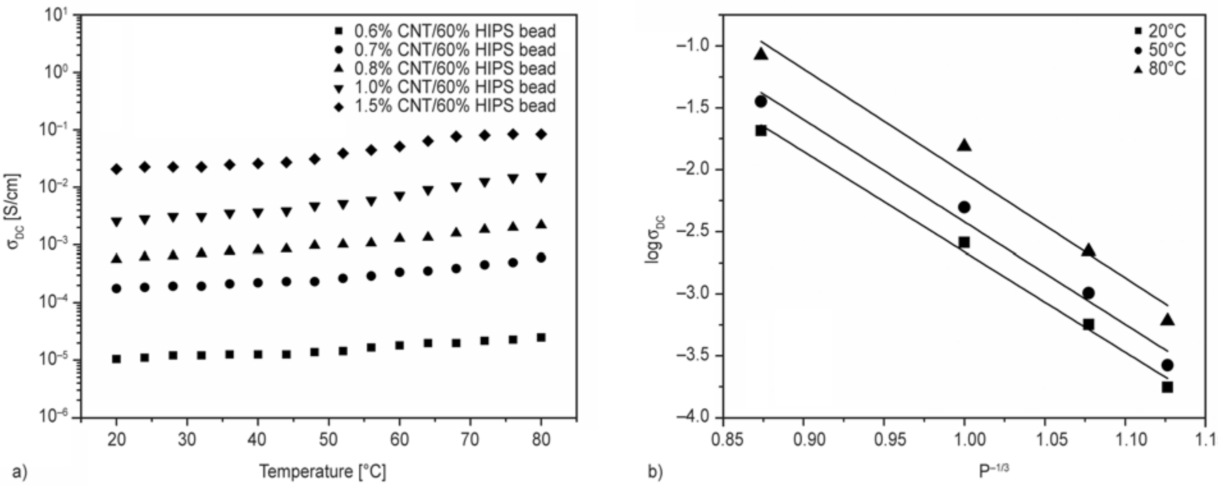

Figure 5. (a) Temperature dependence of DC conductivity of the nanocomposites having $P > P_c$ (b) Linear variation of $\log\sigma_{DC}$ vs $P^{-1/3}$

large conducting regions separated by potential barriers. At higher temperature, the thermally activated voltage fluctuations across insulating regions change the effective barrier between CNTs. Sheng [42] suggested the following relationship (Equation (8)) for the temperature dependent conductivity:

$$\sigma_{\mathrm{DC}} = \sigma_0 \exp\left(-\frac{T_1}{T + T_0}\right) \tag{8}$$

where T_1 is the energy required for an electron to cross the insulating gap between conductive particles aggregates and T_0 represents the temperature above which the thermally activated conduction over the barrier begins to occur.

Conductivity of nanocomposites assisted with tunneling, is expressed as shown by Equation (9):

$$\sigma_{\mathrm{DC}} \propto \exp(-Ad) \tag{9}$$

where A is tunneling parameter and d is the distance between CNTs. When conducting particles are randomly distributed in insulating matrix, then mean average distance between particles is directly proportional to $P^{-1/3}$. Thus, Equation (9) can be written as Equation (10):

$$\log \sigma_{\mathrm{DC}} \propto P^{-1/3} \tag{10}$$

In conducting polymer composites, various researchers have reported tunneling conduction generating from the contacts between conductive clusters is responsible for conductivity [43, 44]. In our system, the variation in electrical conductivity could be associated with tunneling through a potential barrier of varying height resulting from the thermal fluctuations. A polymer nanocomposites consisting of randomly distributed conducting particles, it can be shown that the mean average distance among particles is proportional to $P^{-1/3}$ and also $\log \sigma_{\mathrm{DC}}$ is proportional to $P^{-1/3}$. The linear relationship between $\log \sigma_{\mathrm{DC}}$ and $P^{-1/3}$ (Figure 5b) is indicative to the fact that tunneling conduction may be present in our samples.

However, it is very difficult to explain very low percolation and high conductivity of nanocomposites, because exact size and morphology of MWCNT bundle is not known. The TEM image revealed that MWCNT are uniformly and randomly dispersed in a polymer matrix and have physical entanglement with each other. There are so many factors which influence the high conductivity of nanocomposites. These experiments show that the reason behind conductivity is not only physical contact between CNT or CNT bundles but also the presence of electron tunneling between them. These results revealed that there are many possible factors which can increase the conductivity of the nanocomposites.

I. The high L/D ratio of MWCNT and MWCNT bundles makes a three dimensional conducting structure throughout the matrix but it is very difficult to know the mean size and aspect ratio of MWCNT bundles.
II. High entanglement and irregular packing of MWCNT lead to a good conducting network. Very high surface area of MWCNT and its boundary increases the probability of electron tunneling between them.
III. High surface area of MWCNT and MWCNT bundles increases the probability of tunneling of electrons which leads to a lower P_c value.
IV. MWCNTs and MWCNT bundles can make physical entanglement with neighboring tubes and bundles, and also presence of high Van der Waals forces between CNTs can hold them together. This contact may be with or without a tunneling barrier which leads to a remarkably low P_c value.

Although the first factor plays the major role in conductivity but it is not itself sufficient, consequently some or all of the other three factors are also essential for lowering the P_c value.

However, in the present work of HIPS/MWCNT nanocomposites,effective CNT concentration in the bulk polymerized HIPS phase is increased by incorporating the HIPS beads that led to a reduction in the inter CNT distance. With the increasing of CNT loading from 0.5 to 1 wt%, the conductivity value of the nanocomposites drastically increases from $3.14 \cdot 10^{-9}$ to $2.59 \cdot 10^{-3}$ S/cm. The conductivity of nanocomposites stabilized at around 10^{-3} S/cm which to the best of our knowledgeis the highest value of conductivity ever reported for HIPS/MWCNT nanocomposites at this low level of CNT loading with unaligned, unmodified, commercially available MWCNTs of similar qualities (carbon purity, aspect ratio, etc.)

Comparison of electrical conductivity of the HIPS/MWCNT nanocomposites prepared by our new method with conventional solution blending and melt-mixing method with different weight percent-

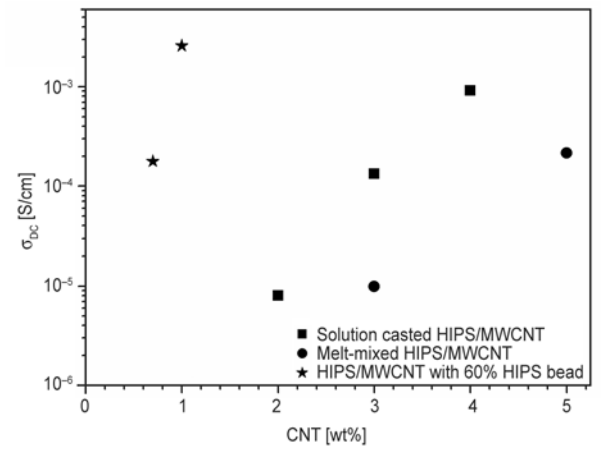

Figure 6. Comparison of the DC conductivity of HIPS/MWCNT nanocomposites prepared by different methods in our study

age of MWCNT is shown in Figure 6. DC conductivity of solution blended nanocomposites was observed $\approx 8.01\cdot10^{-4}$ and $1.32\cdot10^{-4}$ S/cm with 2 and 3 wt% of CNT loadings, respectively. Whereas in our new method similar range of conductivity values of $1.15\cdot10^{-5}$ and $5.67\cdot10^{-4}$ S/cm was achieved in the nanocomposites even at 0.6 and 0.8 wt% CNT loading, respectively. Moreover, the nanocomposites prepared by conventional melt-mixing method shows the DC conductivity of $\approx 9.93\cdot10^{-5}$ S/cm at 3 wt% CNT loading. The similar range of conductivity ($\approx 1.15\cdot10^{-5}$ S/cm) can be obtained with ≈5 times lower CNT loading in the nanocomposite prepared by the proposed method. This very high conductivity of the nanocomposites prepared by the proposed method is due to selective localization of all the CNT in the in situ polymerized HIPS phase in the nanocomposites. Thus, the probability of entanglement between CNTs and tunneling of electrons is expected to increase in comparison to other nanocomposites prepared by conventional methods.

The relationship between AC conductivity and frequency for pure polymer and the nanocomposites containing 0.6 wt% MWCNT loading with varying weight present of HIPS beads is shown in Figure 7a. As can be seen, the AC conductivity of pure polymer increases with increasing frequency, consistent with the behavior of an insulating material. Surprisingly, increasing the weight present of HIPS beads in the nanocomposites at constant CNTs loading shows a gradual increase in conductivity. Increment of HIPS beads in nanocomposites force the CNTs to concise in a small volume of the nanocomposites that leads to more entanglement between them and results in increasing the conductivity value.

It is observed that the AC conductivity remained constant in plateau region up to a critical frequency (f_c), beyond which the conductivity of all the nanocomposites increases with the frequency. Critical frequency (f_c) of the nanocomposites shifted at higher frequencies with increasing weight percent of HIPS beads. Many researchers [45, 46] found a similar kind of increment in the f_c with increasing of conducting filler loading whereas in our case same trend of f_c was found at constant CNTs loading with varying HIPS beads loadings. This is due to the increase in effective concentration of the CNT in the nanocomposites with bead content which in turn increases the concentration of CNT in selective region of the in situ polymerized HIPS phase.

Figure 7b represents the frequency dependence AC conductivity of the nanocomposites with a variation of CNT loading at a constant concentration of HIPS (60 wt%) bead. Compared to the pure HIPS, a higher

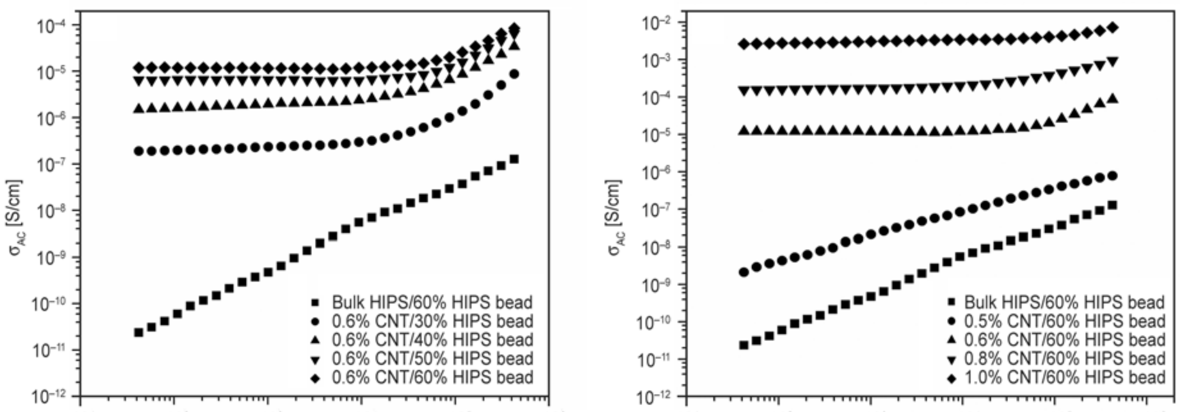

Figure 7. AC conductivity of the HIPS/MWCNT nanocomposites versus frequency at (a) various weight percent of HIPS beads at 0.6 wt% CNT loading and (b) different MWCNT loadings at constant HIPS bead content

conductivity is observed in the nanocomposites with increasing wt% of CNT loading. With an increase in CNT loading from 0~0.6 wt%, a sharp increase in conductivity was found in the low frequency region. However, beyond this (0.6 wt%) CNT loading, a slow but gradual increase in conductivity was evident with the frequency. Furthermore, the nanocomposites containing CNT greater than 1 wt% showed almost constant conductivity value throughout the entire frequency range (42 Hz~5 MHz). This is the-general behavior of a highly conducting material where the AC conductivity occurs mainly due to the flow of electrons, and not due to the polarization of materials.

The dielectric permittivity (ε') determines the ability of a material to store electric potential energy under the influence of an external electric field. Thus, ε' is proportional to the capacitance of the material and alignment of dipoles. Figure 6a and 6b shows the variation of dielectric constant of HIPS/MWCNT nanocomposites at constant frequency (1 kHz and 1 MHz) with increasing amount (wt%) of HIPS bead at constant (0.6 wt%) CNT loading, and with increasing of CNT at constant (60 wt%) HIPS bead loading, respectively. As can be observed, the dielectric constant of the nanocomposites decreased with increasing frequency in both the cases. The dielectric constant of pure HIPS has a low value than all the nanocomposites and behaves almost independent of frequency.

A decrease in ε' is evident in the composites with increase in frequency from 1 kHz to 1 MHz. In dielectric materials, it is generally expected that, the ε' should decrease with increase in the frequency [47]. Potschke *et al.* [48] studied the dielectric constant of polycarbonate/MWCNT composites above the percolation threshold. They also found similar trends of decreasing of dielectric constant with increasing frequency. At low frequency, accumulated interface charges were more readily redistributed on the applied field direction [49]. However, at higher frequency, the periodic alternation of applied electric field leads to the drastic reduction in the diffusion of dipoles in the field direction and the dipole get less time to orient themselves in the direction of alternating field, resulting in decrease in the values of polarization as well as in the ε' value [50]. In both the cases (Figure 8a and 8b), dielectric constant of the HIPS/MWCNT nanocomposites increased with increasing amount of HIPS bead as well as with the CNT content. Increase in ε' with effective concentration of MWCNT in HIPS/MWCNT nanocomposite can be explained based on the enhancement of interfacial polarization. It occurs due to the presence of a thin layer of polymer between CNTs or CNT bundles. The degree of interfacial polarization and charge density is very high resulting from the very large conductivity difference between the MWCNT and the insulating polymer matrix. This interfacial polarization is known as the Maxwell–Wagner–Sillars (MWS) effect [51]. These separated CNTs bundles form, micro capacitors of various length scales [52]. Consequently, the overall capacitance value was increased which resulted in an

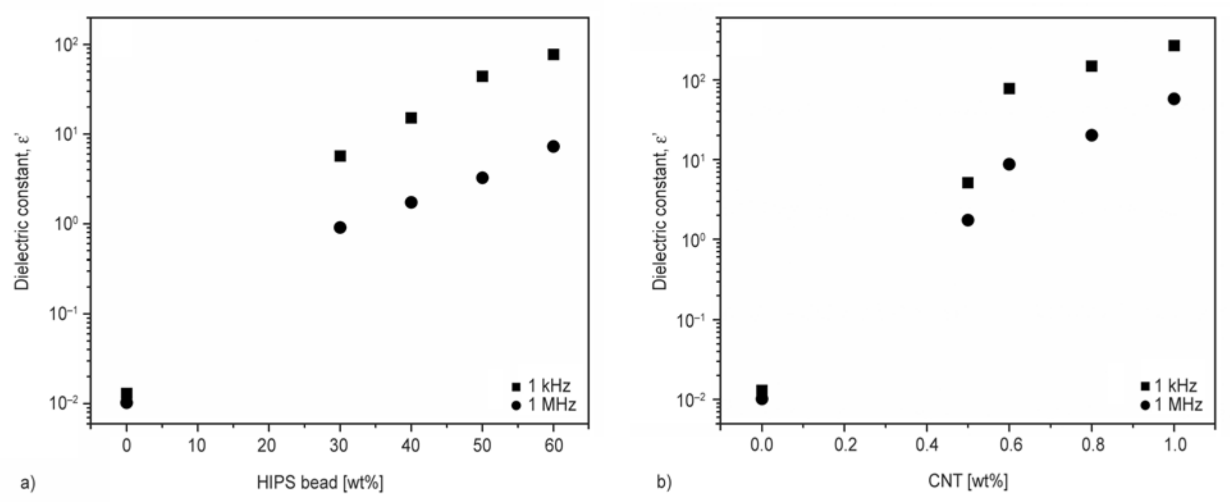

Figure 8. Dielectric constant of HIPS/MWCNT nanocomposites at constant frequency (1 kHz and 1 MHz) (a) with variation of HIPS bead loading at constant (0.6 wt%) CNT loading and (b) with variation of CNT loading at constant (60 wt%) HIPS bead loading

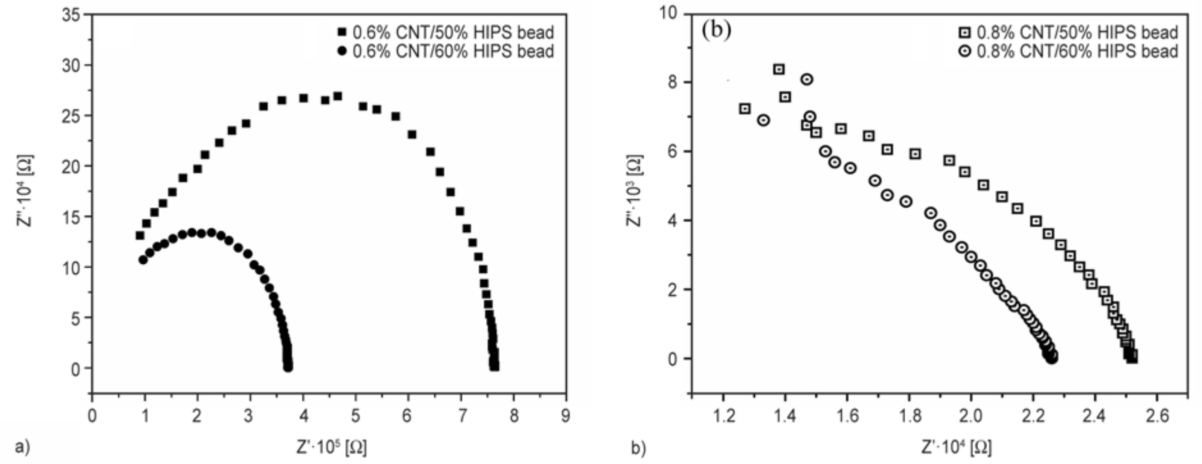

Figure 9. Cole-Cole plots of HIPS/MWCNT nanocomposites (a) 0.6 wt% (b) 0.8 wt%, MWCNT loading variation of HIPS bead (50 and 60 wt%)

increase in the dielectric constant of the nanocomposites.

Figure 9a shows the real (Z') and imaginary (Z'') components of the complex impedance (Cole-Cole) of the HIPS/MWCNT nanocomposites at 0.6 wt% MWCNT loading with varying amount of HIPS bead (50 and 60 wt%), while Figure 9b shows the same plot at 0.8 wt% MWCNT loading. In Cole-Cole plot for polymer/conducting filler nanocomposites system, the real part of impedance represents bulk resistance (R_B) and the imaginary part of impedance represents maximum angular frequency value (ω_{max}). The effect of change in real and imaginary part of the impedance of the system can be expressed in terms of the Equation (11):

$$\omega_{max} = \frac{1}{R_B C_B} \tag{11}$$

As can be seen, that in the both figure (Figure 9a and 9b) Cole-Cole plot yields nearly perfect semi-circle. The radius of these semi-circles decreased with increasing HIPS beads. These indicate that the conductivity of the nanocomposite increases with the increase in the HIPS beads which are associated with effective concentration of MWCNT in HIPS/MWCNT nanocomposite. The Cole–Cole plot of nanocomposite indicates that the composite can be demonstrated by a parallel RC network. At higher frequencies, the release of space charges accumulated at the interface between the MWCNT and the polymer matrix occurs, and thus Z' values seem to be merged together [53]. All the nanocomposites samples exhibited a decrease in Z' with increasing HIPS bead and MWCNT, indicating an increase in DC conductivity.

4. Conclusions

This work demonstrates an easy method for the preparation of HIPS/MWCNT nanocomposites through selective dispersions of MWCNT in the HIPS matrix. A significantly lower value of the percolation threshold of MWCNT was obtained using unmodified and unaligned MWCNT,which is the lowest value ever reported for HIPS/MWCNT nanocomposites system. The incorporation of HIPS bead during the polymerization process acted as 'excluded volume' forcing the MWCNT to disperse selectively in the small region of *in-situ* copolymerized HIPS phase of the nanocomposites. This sort of selective dispersion of MWCNT in the lower volume of *in-situ* polymerized phase increased the effective concentration of MWCNT, leading to the percolation threshold to a lower value of 0.54 wt% of MWCNT. Theoretical studies revealed that the conduction mechanism in the nanocomposites is not only via physical contact between the individual MWCNTs, but also electron tunneling between the neighboring MWCNTs. The polymer coating over individual MWCNT during the bulk polymerization process was indicated from the theoretical approach. The parameters like bead size, bead adding time during copolymerization and bead concentration acted as supreme factors to shift the percolation threshold to an extremely lower value.

References

[1] Connor M. T., Roy S., Ezquerra T. A., Calleja F. J. B.: Broadband AC conductivity of conductor-polymer composites. Physical Review B, **57**, 2286–2294 (1998). DOI: 10.1103/PhysRevB.57.2286

[2] Foulger S. H.: Electrical properties of composites in the vicinity of the percolation threshold. Journal of Applied Polymer Science, **72**, 1573–1582 (1999).
DOI: 10.1002/(SICI)1097-4628(19990620)72:12<1573::AID-APP10>3.0.CO;2-6

[3] Lozano K., Bonilla-Rios J., Barrera E. V.: A study on nanofiber-reinforced thermoplastic composites (II): Investigation of the mixing rheology and conduction properties. Journal of Applied Polymer Science, **80**, 1162–1172 (2001).
DOI: 10.1002/app.1200

[4] Zois H., Apekis L., Omastová M.: Electrical properties of carbon black-filled polymer composites. Macromolecular Symposia, **170**, 249–256 (2001).
DOI: 10.1002/1521-3900(200106)170:1<249::AID-MASY249>3.0.CO;2-F

[5] Jäger K-M., McQueen D. H.: Fractal agglomerates and electrical conductivity in carbon black polymer composites. Polymer, **42**, 9575–9581 (2001).
DOI: 10.1016/S0032-3861(01)00478-5

[6] Kar P., Khatua B. B.: PTCR characteristics of polycarbonate/nickel-coated graphite-based conducting polymeric composites in presence of poly(caprolactone). Polymer Composites, **32**, 747–755 (2011).
DOI: 10.1002/pc.21093

[7] Kar P., Shrivastava N. K., Mallick S., Khatua B. B.: PTCR characteristics of poly(styrene-*co*-acrylonitrile) copolymer/stainless steel powder composites. Journal of Applied Polymer Science, **124**, 607–615 (2012).
DOI: 10.1002/app.35002

[8] Shrivastava N. K., Khatua B. B.: Development of electrical conductivity with minimum possible percolation threshold in multi-wall carbon nanotube/polystyrene composites. Carbon, **49**, 4571–4579 (2011).
DOI: 10.1016/j.carbon.2011.06.070

[9] Maity S., Shrivastava N. K., Khatua B. B.: Reduction of percolation threshold through double percolation in melt-blended polycarbonate/acrylonitrile butadiene styrene/multiwall carbon nanotubes elastomer nanocomposites. Polymer Composites, **34**, 570–579 (2013).
DOI: 10.1002/pc.22462

[10] Spitalsky Z., Tasis D., Papagelis K., Galiotis C.: Carbon nanotube–polymer composites: Chemistry, processing, mechanical and electrical properties. Progress in Polymer Science, **35**, 357–401 (2010).
DOI: 10.1016/j.progpolymsci.2009.09.003

[11] Moniruzzaman M., Winey K. I.: Polymer nanocomposites containing carbon nanotubes. Macromolecules, **39**, 5194–5205 (2006).
DOI: 10.1021/ma060733p

[12] Fiedler B., Gojny F. H., Wichmann M. H. G., Nolte M. C. M., Schulte K.: Fundamental aspects of nano-reinforced composites. Composites Science and Technology, **66**, 3115–3125 (2006).
DOI: 10.1016/j.compscitech.2005.01.014

[13] Shrivastava N. K., Kar P., Maity S., Khatua B. B.: A facile route to develop electrical conductivity with minimum possible multi-wall carbon nanotube (MWCNT) loading in poly(methyl methacrylate)/MWCNT nanocomposites. Polymer International, **61**, 1683–1692 (2012).
DOI: 10.1002/pi.4263

[14] Mitchell C. A., Bahr J. L., Arepalli S., Tour J. M., Krishnamoorti R.: Dispersion of functionalized carbon nanotubes in polystyrene. Macromolecules, **35**, 8825–8830 (2002).
DOI: 10.1021/ma020890y

[15] Bahr J. L., Tour J. M.: Covalent chemistry of single-wall carbon nanotubes. Journal of Materials Chemistry, **12**, 1952–1958 (2002).
DOI: 10.1039/B201013P

[16] Dyke C. A., Tour J. M.: Solvent-free functionalization of carbon nanotubes. Journal of the American Chemical Society, **125**, 1156–1157 (2003).
DOI: 10.1021/ja0289806

[17] Jin Z., Pramoda K. P., Xu G., Goh S. H.: Dynamic mechanical behavior of melt-processed multi-walled carbon nanotube/poly(methyl methacrylate) composites. Chemical Physics Letter, **337**, 43–47 (2001).
DOI: 10.1016/S0009-2614(01)00186-5

[18] Ayewah D. O., Davis D. C., Krishnamoorti R., Lagoudas D. C., Sue H. J., Willson M.: A surfactant dispersed SWCNT-polystyrene composite characterized for electrical and mechanical properties. Composites Part A, **41**, 842–849 (2010).
DOI: 10.1016/j.compositesa.2010.02.015

[19] McNally T., Pötschke P., Halley P., Murphy M., Martin D., Bell S. E. J., Brennan G. P., Bein D., Lemoine P., Quinn J. P.: Polyethylene multiwalled carbon nanotube composites. Polymer, **46**, 8222–8232 (2005).
DOI: 10.1016/j.polymer.2005.06.094

[20] Pötschke P., Bhattacharyya A. R., Janke A.: Carbon nanotube-filled polycarbonate composites produced by melt mixing and their use in blends with polyethylene. Carbon, **42**, 965–969 (2004).
DOI: 10.1016/j.carbon.2003.12.001

[21] Manchado M. A. L., Valentini L., Biagiotti J., Kenny J. M.: Thermal and mechanical properties of single-walled carbon nanotubes–polypropylene composites prepared by melt processing. Carbon, **43**, 1499–1505 (2005).
DOI: 10.1016/j.carbon.2005.01.031

[22] Wanjale S. D., Jog J. P.: Crystallization and phase transformation kinetics of poly(1-butene)/MWCNT nanocomposites. Polymer, **47**, 6414–6421 (2006).
DOI: 10.1016/j.polymer.2006.07.011

[23] McClory C., Pötschke P., McNally T.: Influence of screw speed on electrical and rheological percolation of melt-mixed high-impact polystyrene/MWCNT nanocomposites. Macromolecular Materials and Engineering, **296**, 59–69 (2011).
DOI: 10.1002/mame.201000220

[24] Lee M., Jeon H., Min B. H., Kim J. H.: Morphology and electrical properties of polymethylmethacrylate/poly(styrene-*co*-acrylonitrile)/multi-walled carbon nanotube nanocomposites. Journal of Applied Polymer Science, **121**, 743–749 (2011).
DOI: 10.1002/app.33819

[25] Göldel A., Kasaliwal G. R., Pötschke P., Heinrich G.: The kinetics of CNT transfer between immiscible blend phases during melt mixing. Polymer, **53**, 411–421 (2012).
DOI: 10.1016/j.polymer.2011.11.039

[26] Dufresne A., Paillet M., Putaux J. L., Canet R., Carmona F., Delhaes P., Cui S.: Processing and characterization of carbon nanotube/poly(styrene-*co*-butyl acrylate) nanocomposites. Journal of Materials Science, **37**, 3915–3923 (2002).
DOI: 10.1023/A:1019659624567

[27] Singh B. K., Kar P., Shrivastava N. K., Banerjee S., Khatua B. B.: Electrical and mechanical properties of acrylonitrile-butadiene-styrene/multiwall carbon nanotube nanocomposites prepared by melt-blending. Journal of Applied Polymer Science, **124**, 3165–3174 (2012).
DOI: 10.1002/app.34948

[28] Zhao Z., Zheng W., Yu W., Long B.: Electrical conductivity of poly(vinylidene fluoride)/carbon nanotube composites with a spherical substructure. Carbon, **47**, 2118–2120 (2009).
DOI: 10.1016/j.carbon.2009.03.043

[29] Mu M., Walker A. M., Torkelson J. M., Winey K. I.: Cellular structures of carbon nanotubes in a polymer matrix improve properties relative to composites with dispersed nanotubes. Polymer, **49**, 1332–1337 (2008).
DOI: 10.1016/j.polymer.2008.01.036

[30] Liu L., Grunlan J. C.: Clay assisted dispersion of carbon nanotubes in conductive epoxy nanocomposites. Advanced Functional Materials, **17**, 2343–2348 (2007).
DOI: 10.1002/adfm.200600785

[31] Weber M., Kamal M. R.: Estimation of the volume resistivity of electrically conductive composites. Polymer Composites, **18**, 711–725 (1997).
DOI: 10.1002/pc.10324

[32] Vavouliotis A., Fiamegou E., Karapappas P., Psarras G. C., Kostopoulos V.: DC and AC conductivity in epoxy resin/multiwall carbon nanotubes percolative system. Polymer Composites, **31**, 1874–1880 (2010).
DOI: 10.1002/pc.20981

[33] Blighe F. M., Hernandez Y. R., Blau W. J., Coleman J. N.: Observation of percolation-like scaling – far from the percolation threshold – in high volume fraction, high conductivity polymer-nanotube composite films. Advanced Materials, **19**, 4443–4447 (2007).
DOI: 10.1002/adma.200602912

[34] Alig I., Skipa T., Lellinger D., Pötschke P.: Destruction and formation of a carbon nanotube network in polymer melts: Rheology and conductivity spectroscopy. Polymer, **49**, 3524–3532 (2008).
DOI: 10.1016/j.polymer.2008.05.037

[35] Kota A. K., Cipriano B. H., Duesterberg M. K., Gershon A. L., Powell D., Raghavan S. R., Bruck H. A.: Electrical and rheological percolation in polystyrene/MWCNT nanocomposites. Macromolecules, **40**, 7400–7406 (2007).
DOI: 10.1021/ma0711792

[36] Martin C. A., Sandler J. K. W., Shaffer M. S. P., Schwarz M-K., Bauhofer W., Schulte K., Windle A. H.: Formation of percolating networks in multi-wall carbon-nanotube–epoxy composites. Composites Science and Technology, **64**, 2309–2316 (2004).
DOI: 10.1016/j.compscitech.2004.01.025

[37] Pötschke P., Goad M-A., Alig I., Dudkin S., Lellinger D.: Rheological and dielectrical characterization of melt mixed polycarbonate-multiwalled carbon nanotube composites. Polymer, **45**, 8863–8870 (2004).
DOI: 10.1016/j.polymer.2004.10.040

[38] Kim H. M., Choi M-S., Joo J., Cho S. J., Yoon H. S.: Complexity in charge transport for multiwalled carbon nanotube and poly(methyl methacrylate) composites. Physical Review B, **74**, 54202/1–54200/7 (2006).
DOI: 10.1103/PhysRevB.74.054202

[39] Balberg I., Anderson C. H., Alexander S., Wagner N.: Excluded volume and its relation to the onset of percolation. Physical Review B, **30**, 3933–3943 (1984).
DOI: 10.1103/PhysRevB.30.3933

[40] Fan J., Wan M., Zhu D., Chang B., Pan Z., Xie S.: Synthesis, characterizations, and physical properties of carbon nanotubes coated by conducting polypyrrole. Journal of Applied Polymer Science, **74**, 2605–2610 (1999).
DOI: 10.1002/(SICI)1097-4628(19991209)74:11<2605::AID-APP6>3.0.CO;2-R

[41] Benoit J-M., Corraze B., Lefrant S., Blau W. J., Bernier P., Chauvet O.: Transport properties of PMMA-carbon nanotubes composites. Synthetic Metals, **121**, 1215–1216 (2001).
DOI: 10.1016/S0379-6779(00)00838-9

[42] Sheng P.: Fluctuation-induced tunneling conduction in disordered materials. Physical Review B, **21**, 2180–2195 (1980).
DOI: 10.1103/PhysRevB.21.2180

[43] Alexander M. G.: Anomalous temperature dependence of the electrical conductivity of carbon-poly(methyl methacrylate) composites. Materials Research Bulletin, **34**, 603–611 (1999).
DOI: 10.1016/S0025-5408(99)00043-4

[44] Sichel E. K., Gittelman J. I., Sheng P.: Transport properties of the composite material carbon-poly(vinyl chloride). Physical Review B, **18**, 5712–5716 (1978).
DOI: 10.1103/PhysRevB.18.5712

[45] Kim Y. J., Shin T. S., Choi H. D., Kwon J. H., Chung Y-C., Yoon H. G.: Electrical conductivity of chemically modified multiwalled carbon nanotube/epoxy composites. Carbon, **43**, 23–30 (2005).
DOI: 10.1016/j.carbon.2004.08.015

[46] Barrau S., Demont P., Peigney A., Laurent C., Lacabanne C.: DC and AC conductivity of carbon nanotubes–polyepoxy composites. Macromolecules, **36**, 5187–5195 (2003).
DOI: 10.1021/ma021263b

[47] Sahoo B. P., Naskar K., Tripathy D. K.: Conductive carbon black-filled ethylene acrylic elastomer vulcanizates: Physico-mechanical, thermal, and electrical properties. Journal of Materials Science, **47**, 2421–2433 (2012).
DOI: 10.1007/s10853-011-6065-8

[48] Pötschke P., Dudkin S. M., Alig I.: Dielectric spectroscopy on melt processed polycarbonate–multiwalled carbon nanotube composites. Polymer, **44**, 5023–5030 (2003).
DOI: 10.1016/S0032-3861(03)00451-8

[49] Psarras G. C., Manolakaki E., Tsangaris G. M.: Electrical relaxations in polymeric particulate composites of epoxy resin and metal particles. Composites Part A: Applied Science and Manufacturing, **33**, 375–384 (2002).
DOI: 10.1016/S1359-835X(01)00117-8

[50] Zhao X., Koos A. A., Chu B. T. T., Johnston C., Grobert N., Grant P. S.: Spray deposited fluoropolymer/multi-walled carbon nanotube composite films with high dielectric permittivity at low percolation threshold. Carbon, **47**, 561–569 (2009).
DOI: 10.1016/j.carbon.2008.10.042

[51] Sillars R. W.: The behaviour of polar molecules in solid paraffin wax. Proceedings of the Royal Society A, **169**, 66–83 (1939).
DOI: 10.1098/rspa.1938.0195

[52] Pecharromán C., Moya J. S.: Experimental evidence of a giant capacitance in insulator–conductor composites at the percolation threshold. Advanced Materials, **12**, 294–297 (2000).
DOI: 10.1002/(SICI)1521-4095(200002)12:4<294::AID-ADMA294>3.0.CO;2-D

[53] El Ghanem H. M., Jawad S. A., Al-Saleh M. H., Hussain Y. A., Salah W.: Effect of dc-bias on the dielectric behavior of CNT/ABS nanocomposites. Physica B: Condensed Matter, **418**, 41–46 (2013).
DOI: 10.1016/j.physb.2013.02.039

eXPRESS Polymer Letters Vol.8, No.1 (2014) 30–38
Available online at www.expresspolymlett.com
DOI: 10.3144/expresspolymlett.2014.4

Nanostructured poly(benzimidazole) membranes by N-alkylation

P. Haro Dominguez, K. Grygiel, J. Weber[*]

Max Planck Institute of Colloids and Interfaces, Department of Colloid Chemistry, Research Campus Golm, D-14424 Potsdam, Germany

Received 16 May 2013; accepted in revised form 31 August 2013

Abstract. Modification of poly(benzimidazole) (PBI) by N-alkylation leads to polymers capable of undergoing microphase separation. Polymers with different amounts of C_{18} alkyl chains have been prepared. The polymers were analyzed by spectroscopy, thermal analysis, electron microscopy and X-ray scattering. The impact of the amount of alkyl chains on the observed microphase separation was analyzed. Membranes prepared from the polymers do show microphase separation, as evidenced by scattering experiments. While no clear morphology could be derived for the domains in the native state, evidence for the formation of lamellar morphologies upon doping with phosphoric acid is provided. Finally, the proton conductivity of alkyl-modified PBI is compared with that of pure PBI, showing that the introduction of alkyl side chains does not result in significant conductivity changes.

Keywords: *polymer membranes, molecular engineering, nanomaterials*

1. Introduction

Proton exchange membrane fuel cells (PEMFCs) received a great deal of interest in recent years as they provide an alternative to classic combustion engines. Nafion® can still be considered as a benchmark for proton exchange membranes, despite the fact that its development by DuPont was more than 50 years ago. Ever since then, big efforts have been done by different research groups to understand the characteristic features of Nafion [1–4], which makes it superior to other systems. The microphase-separated microstructure of Nafion, providing mechanical strength together with well-connected water domains that facilitate proton-transport, has been identified as the reason for the superior performance of Nafion. The rather high price of Nafion has led researchers to look for alternative ionomer membranes. This search took almost always the possibility of the polymers to undergo microphase separation into account.

Next to ionomers, acid-base complexes have been regarded as alternatives to Nafion. The probably most prominent example of this class of materials is phosphoric acid (PA) doped polybenzimidazole (PBI) [2, 5, 6]. In this material, PBI provides the mechanical support of the membrane and acts as a basic anchor to the phosphoric acid, which is mainly responsible for the high proton conductivity. One advantage of the PBI system is its easy operability up to high temperatures (150–180°C), which is not easily possible with Nafion membranes. Operation at such high temperatures results in higher tolerance against fuel impurities and an easier heat management and is hence regarded as beneficial. However, the PA-PBI system lacks to the best of our knowledge any self-organization into a microphase-sepa-

---

[*]Corresponding author, e-mail: jens.weber@mpikg.mpg.de

rated structure known from the ionomers. Typically, the PBI chains interrupt the proton conduction pathways of the PA, which consist mainly of dynamic hydrogen-bonded structures [7]. This can be partly overcome by creating nanostructured PA-PBI systems, which do indeed show higher proton conductivities compared to homogenous systems [8]. In earlier work, mesoporous PBI was prepared by templating [9], and the pores were backfilled by PA, which is overall a rather time-consuming synthesis pathway, which is hard to implement in membrane technology. There are a few other attempts to achieve nanostructural control, which were reported recently, including (multi)block copolymer synthesis and generally, a positive effect on the conductivity was found but no detailed structural information (*e.g.* domain size) was provided so far [10–12].

Inspired by recent attempts to use graft copolymers to induce microphase-separated structures for organic-electronics applications [13], we aim to synthesize poly[2,2′-(m-phenylene)-5,5′bibenzimidazole] (PBI) based graft-copolymers that can undergo microphase separation. Within this communication, we present the grafting of PBI with long (C_{18}) alkyl chains following modification protocols presented by Gieselman and Reynolds [14]. The modification of PBIs by N-alkylation was reported by previously by Klaehn *et al.* [15] , who did however not study the mesostructure of the resulting polymers.The modification of so-called ABPBI, i.e. poly(2,5-benzimidazole) by N-alkylation for gas permeation membranes was reported by Kumbharkar and Kharul [16], but again no analysis of any microphase separation was studied. Finally, a very recent study by Jana and coworkers came to our attention, which dealt with the N-alkylation of PBI. Alkyl chains up to C_{16} length were introduced [17]. The study analysed the impact of the alkyl chain length and reported improved solubility while maintaining satisfactory proton conductivity.

There is however no detailed study on the microphase separation of alkylated PBI available yet. It is hence within the focus of the current manuscript to provide an analysis of the microstructure of the resulting polymers in dry and phosphoric acid doped state. Characterization will be done by means of small-angle and wide-angle X-ray scattering (SAXS and WAXS) and electron microscopy. First conductivity data will also be reported.

2. Experimental

2.1. Materials and methods

3,3′-diaminobenzidine (DAB, 99%, D12384) and diphenyl isophthalate (DPI, 99%, 411698) were purchased from Aldrich via Sigma-Aldrich (Steinheim, Germany) and used without further purification. Sodium hydride (NaH, 95%, 223441) and dry NMP (99.5%, 328634) and dry N,N-dimethylacetamide (DMAc, 99.8%, 271012) were also purchased from Sigma-Aldrich. 1-Bromooctadecane (>97%, 199494) was purchased from Aldrich. Other solvents used for workup or syntheses under ambient conditions, such as methanol (MeOH, Merck 1.06008.9180, Darmstadt, Germany), diethylether (VWR, 23811.361; Leuven, Belgium), DMAc (Alfa Aesar; A10924, Karlsruhe, Germany) were of analytical grade.

^{1}H-NMR measurements were carried out using a Bruker DPX-400 spectrometer (Bruker, Germany) operating at 400.1 MHz. As solvents, deuterated chloroform ($CDCl_3$, 151823), deuterated dimethylsulfoxide (DMSO-*d6*, 522120), deuterated tetrahydrofuran (THF-*d8*, 184314) (all Sigma-Aldrich) or mixtures thereof were used. Calibration was carried out using signals corresponding to non-deuterated solvent ($CDCl_3$: 7.26 ppm; DMSO-*d6*: 2.50 ppm).

Fourier-transform infrared (FT-IR) spectra were collected with a Varian 1000 Scimitar FT-IR spectrometer (FTS-1000, Varian, Berlin, Germany), equipped with an attenuated total reflection (ATR) setup.

Gel permeation chromatography (GPC, Thermo Separation Products (TKA), Niederelbert, Germany) in 0.5 wt% LiBr in N-methylpyrrolidon (NMP) as the eluent was performed with a system containing PSS (Mainz, Germany) GRAM 100 and 1000 Å columns. It provides simultaneous ultraviolet (UV) and refractive index (RI) detection. 100 µL were injected and separated at 70°C and a flow of $0.8\ mL\cdot min^{-1}$. GPC in 0.5 wt% LiBr in DMSO as the eluent was performed with a GPC system (Thermo Separation Products (TKA), Niederelbert, Germany) containing two PSS GRAL LIN columns. It provides simultaneous UV and RI detection. 100 µL were injected and separated at 70°C and a flow of $1.0\ mL\cdot min^{-1}$. Samples were filtered through 0.45 µm syringe filters prior to use.

WAXS measurements were performed with a D8 Advance machine from Bruker Instruments (Bruker AXS, Karlsruhe, Germany). The radiation was of the wavelength of CuK_α (0.1542 nm). Measurements were done in reflection geometry. Samples were measured as fine powders (or films respectively) on a silicon sample holder.

SAXS on solid samples was measured with a Rotating Anode Instrument (4 kW, CuK_α, Enraf-Nonius, Germany) with point collimation and MARCCD detector (pixel size 79, Marresearch, Norderstedt, Germany) at room temperature and a distance of 74 cm between detector and sample. 2D diffraction pictures were corrected for background scattering and transformed into 1D radial averages of the scattering intensity using the Fit2D program. Calibration was done using silver behenate.

Thermogravimetric Analysis (TGA) was carried out on a Netzsch TG 209 F1 (Netzsch, Selb, Germany) at 10 $K\cdot min^{-1}$ under either synthetic air or nitrogen atmosphere.

Scanning electron microscopy (SEM) pictures were taken with a Gemini Leo 1550 (Zeiss AG, Jena, Germany) microscope at 3 kV. The samples were loaded on carbon coated stubs and coated by sputtering with Au/Pd alloy prior to imaging.

Proton Conductivity: Resistance measurements were performed using a Solartron SI1260 Impedance/Gain Phase analyzer and Solartron SI1287 Electrochemical interface (AC amplitude: 10 mV; DC potential versus open circuit: 100 mV; frequency range: 0.5 MHz to 0.1 Hz; Solartron Analytical, AMETEK GmbH, Meerbusch, Germany). Membrane disks of 6 mm diameter were contacted with Pt-foils of the same diameter and measurements were performed under closed atmosphere at room temperature (22.5°C, 16% outer humidity). The membranes were dried under vacuum at 60°C for 20 hours prior to measurements. The proton conductivity σ was calculated from the resistance κ by: $\sigma = h\cdot(\kappa A)^{-1}$, where A is the surface area of the films (0.2827 cm^2) and h is the film thickness (determined using a vernier scale).

2.2. Synthesis of N-alkylated PBI

The parent PBI was synthesized using standard protocols developed by Vogel and Marvel [18], and purified from insoluble byproducts by hot filtration from DMAc followed by precipitation and washing by methanol. In a typical alkylation experiment, 0.5 g of PBI were dissolved in anhydrous NMP at 80°C and cooled to *RT*. The required amount of sodium hydride was added under inert atmosphere and the mixture was heated to 80°C for 3 h under inert atmosphere. The required amount of 1-bromooctadecane was slowly added afterwards and the reaction was allowed to proceed at 80°C for 24 h. The polymer was precipitated by MeOH after cooling to *RT* and washed once with diethylether and three times with MeOH before dried under vacuum at 100°C.

3. Results and discussion

3.1. Chemical and structural characterisation

PBI was synthesized by classic melt polycondensation, as introduced by Vogel and Marvel [18]. After solid-state curing at 400°C, the crude product was stirred in hot DMAc (containing 0.5 wt% LiCl) for 20 h, followed by hot filtration in order to exclude non-soluble byproducts. The chemical identity of the parent PBI was verified by FTIR and ^1H-NMR spectroscopy. FTIR spectroscopy could clearly show the characteristic peaks of PBI at 1620, 1443 and 1280 cm^{-1}, 800 and 700 cm^{-1} in accordance with literature [19]. The ^1H-NMR spectra prove the expected structure of the polymer. At 13.3 ppm the prominent NH-protons on the benzimidazole appear, while the peaks between 9.2 and 7.6 ppm can be assigned to the aromatic protons in the main backbone according to reported literature [17, 20].

Reaction of deprotonated PBI with octadecyl bromide (C_{18}-Br) was performed at 75°C for 3 days. Deprotonation of PBI was done by reaction with NaH in dry NMP at 75°C for 3 hours. A slight excess of NaH with respect to the targeted conversion was always used. We aimed at modification of PBI with 0.5, 1 and 2 equivalents of C_{18}-Br per repeat unit (RPU) in order to study the influence of the amount of alkyl chains on the microphase separation. Samples were named PBI-C_{18}-1 to PBI-C_{18}-3 where PBI-C_{18}-1 is the PBI with lowest degree of functionalization. The degree of alkylation (D.A.) was calculated based on NMR analysis of the resulting polymers (see Table 1 and Figure 1).

The calculation is based on the ratio between aromatic backbone H atoms, which are set to 10 protons, and the methylene protons next to the imidazolium N atom (found at 4.5 ppm). The methylene protons of the N–CH_2–$\mathbf{CH_2}$– methylene group (at 1.83 ppm) can also be used for comparison and gave similar results. The NMR spectrum of the modified polymers showed a more complex aromatic region, which can be explained by the more complex chemical environment, which is intro-

Table 1. Molecular characteristics of the parent PBI and the alkyl-modified PBI

Entry	D.A. target	D.A. (^{1}H-NMR)	wt% alkyl (NMR)	wt% alkyl (TGA)	Mw[a] [g·mol^{-1}]	Đ[a]
PBI	–	–	–		45000	2.6
PBI-C_{18}-1	0.5	0.44	25.6	18	52550	1.9
PBI-C_{18}-2	1	0.68	30.4	28	53720	2.1
PBI-C_{18}-3	2	1.18	36.4	42	62000	2.6

[a] determined by GPC at 70°C, eluent: NMP, polystyrene (PS) standards

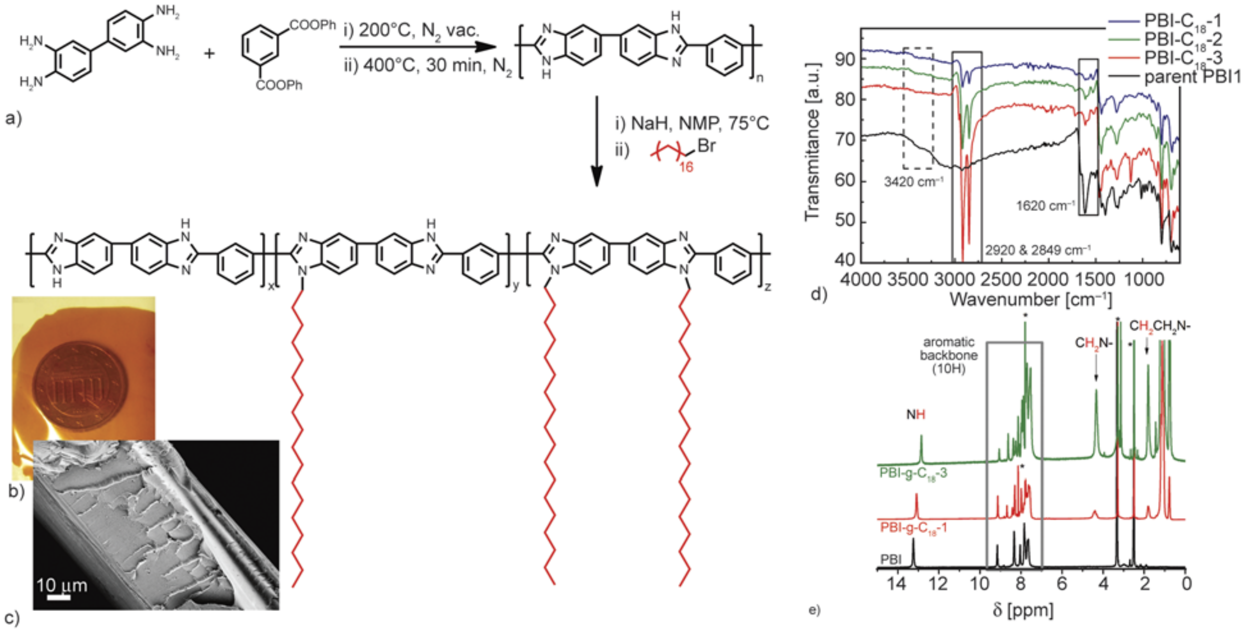

Figure 1. a) chemical structure and synthesis scheme of PBI and PBI-C_{18}; b) photograph of a PBI-C_{18}-3 membrane and c) corresponding SEM micrograph (cross-section); d) FT-IR spectra of PBI and modified PBI, please note that the overly prominent band around 1650–1620 cm^{-1} in the case of pure PBI and (to lower extent also for PBI-g-C_{18}-1/-2) is due to an overlap with solvent residues (DMAc); e) representative ^{1}H-NMR spectra of PBI and PBI-C_{18}-1 and PBI-C_{18}-3, please note that the spectra were taken in different solvents/solvent mixtures, which explains the shift of the NH proton, * marks solvent peaks

duced upon grafting of alkyl chains to the imidazole units. Overall, the spectra agree well with spectra of short-chain alkyl modified PBI reported by Maity *et al*. [17]. The D.A. calculated from NMR results were furthermore supported by thermal gravimetric analysis (TGA), see below.

The reactions did not result in full conversions, *i.e.* the experimentally achieved D.A. was always lower than the targeted value. This is not unexpected, as full conversion in grafting-onto is typically hard to achieve, due to *e.g.* steric reasons. This becomes obvious especially for the case of targeted full alkylation, where the PBI backbone chain would have to stretch to allow all alkyl chains to be attached, resulting in a brush-like morphology. Hence, the degree of success of the grafting reaction dropped from 88% for PBI-C_{18}-1 to 67.5% for PBI-C_{18}-2 and 59% for PBI-C_{18}-3. These values can be translated into the weight fraction of the alkyl component within the graft copolymers, which is found to be 25.6, 30.4 and 36.4 wt% for PBI-C_{18}-1 to PBI-C_{18}-3, respectively. It should be noted that full conversion could be reached in comparable N-alkylation reactions, given that a significant excess of the alkyl compound was used [15]. The degree of alkylation reached within this study agrees reasonable with results obtained by Maity *et al.* [17].

Overall, alkylation resulted in a better solubility of the polymers in common organic solvents. For instance, PBI-C_{18}-3 is soluble in THF and $CHCl_3$, which are typically not good solvents for PBI. Transparent films could be casted from 10 wt% solutions of PBI-C_{18}-3 in THF or $CHCl_3$ after filtration. The increased solubility was only observed for the highest degree of alkylation, which indicates that there is a certain weight fraction of alkyl chains, which is necessary for enhanced solubility.

FTIR spectroscopy could also clearly prove the success of the reaction. Strong C–H bands arise at 2900 cm^{-1} with increasing intensity, which can be clearly attributed to the alkyl chains. Finally, size exclusion chromatography (SEC) using NMP as eluent could also give a qualitative proof of the success of the grafting reaction. An increase of the apparent weight-average molecular weight was observed. As the shape and solvation state of the macromolecules is however changing with increasing functionalization, the SEC results cannot be discussed in detail and the SEC data should not be overstressed.

The thermal properties of the polymers were evaluated using thermogravimetric analysis (TGA). All polymers were stable up to 320°C under air atmosphere. Above this temperature, thermal degradation of the alkyl chains settled in. Full decomposition started around 500°C. The weight fraction of alkyl as determined by TGA is compiled in Table 1 and generally in good agreement with the NMR results.

Initial experiments on the potential microphase separation were performed on polymer powders using small-angle and wide-angle X-ray scattering (SAXS and WAXS, see Figure 2a, 2b). A microphase separation could be observed after thermal annealing at 240°C under N_2 atmosphere. Only a weak peak at scattering vector q = 1.8–1.9 nm^{-1} was observed in the SAXS patterns for PBI-C_{18}-1 and -2, while PBI-C_{18}-3 showed a more pronounced but still broad peak (q = 1.9 nm^{-1}), corresponding to a d-spacing of ~3.3 nm. No clear structure assignment could be made on the basis of the SAXS patters solely, as no other features could be identified clearly.

WAXS showed amorphous halos only, except for PBI-C_{18}-3, for which weak reflections were observed at $2\theta \sim 21.7$ and 24°, indicative of partially crystallized alkyl chains. Further indication of partial crystallinity was derived from scanning electron microscopy (SEM). No distinct morphology was observed for low D.A. (see Figure 2c). This is in contrast to PBI-C_{18}-3, which showed some plate-like layered morphologies and even clear facets after annealing (Figure 2d). This leads to the conclusion, that upon high D.A., the polymers do show a significant microphase separation, most probably into a lamellar phase. The microphase separation comes along with crystallization of the long alkyl side-chains. This picture is in good agreement with reports on lamellar phases formed from polymers bearing long alkyl side chains, such as polyelectrolyte complexes or poly(ionic liquids) [21, 22].

Finally, we were interested whether the microphase separation is also effective upon doping with phosphoric acid. Membranes were cast from THF and annealed before proceeding further on. The membrane was cut into pieces and soaked in H_3PO_4 of various concentrations (2M, 6M, 10M or 14M, respectively). The membranes were dried at 80°C under vacuum afterwards and the acid uptake was determined gravimetrically (see Figure 4b). As expected, the uptake increased with increasing phosphoric acid concentration except for doping of PBI-C_{18}-3 with 2M H_3PO_4. This sample does show only very low acid uptake, this may be due to the hydrophobicity of the material, which could hamper phosphoric acid uptake at low $c_{H_3PO_4}$. It should be noted that the membranes kept their shape very well during acid doping and drying.

The microphase separation was again analyzed by SAXS investigations (Figure 3a–3c). The observed peaks got much stronger (and sharper) with increasing acid uptake for all graft copolymers, indicating that the microphase separation got much stronger with increasing acid loading. Given the non-polar character of the C_{18} alkyl chains, this comes as no surprise. It can be suspected that the phosphoric acid populates the polar PBI domain (forming benzimidazolium salts and/or being hydrogen bonded). This results first of all in a swelling of the PBI domain that gives rise to larger d-spacings with increasing acid loading ($d \sim 4.4$ nm after doping with 14M H_3PO_4 compared to $d \sim 3.3$ nm in the case of PBI-C_{18}-3, see Figure 3d). Secondly, the segregation tendency is increased as a consequence of the increased hydrophobic-hydrophilic contrast. In analogy to block copolymer microphase-separation physics, it can be argued that the Flory-Huggins interaction parameter χ is changed (increased), which leads to stronger segregation tendency. Compared to the universal block copolymer phase-diagram, this could be interpreted as shift from the disordered phase into the lamellar regime.

Consequently, higher order reflections got visible in the case of PBI-C_{18}-2 and -3 starting from acid loadings of 6M. The higher order reflections were observed at $q \sim 2.8$ nm^{-1}, which is the double of the q-value of the primary peak ($q \sim 1.4$ to 1.5 nm^{-1}). Such 1:2 ratio is typically observed for lamellar structures. For PBI-C_{18}-1, no higher order reflections got

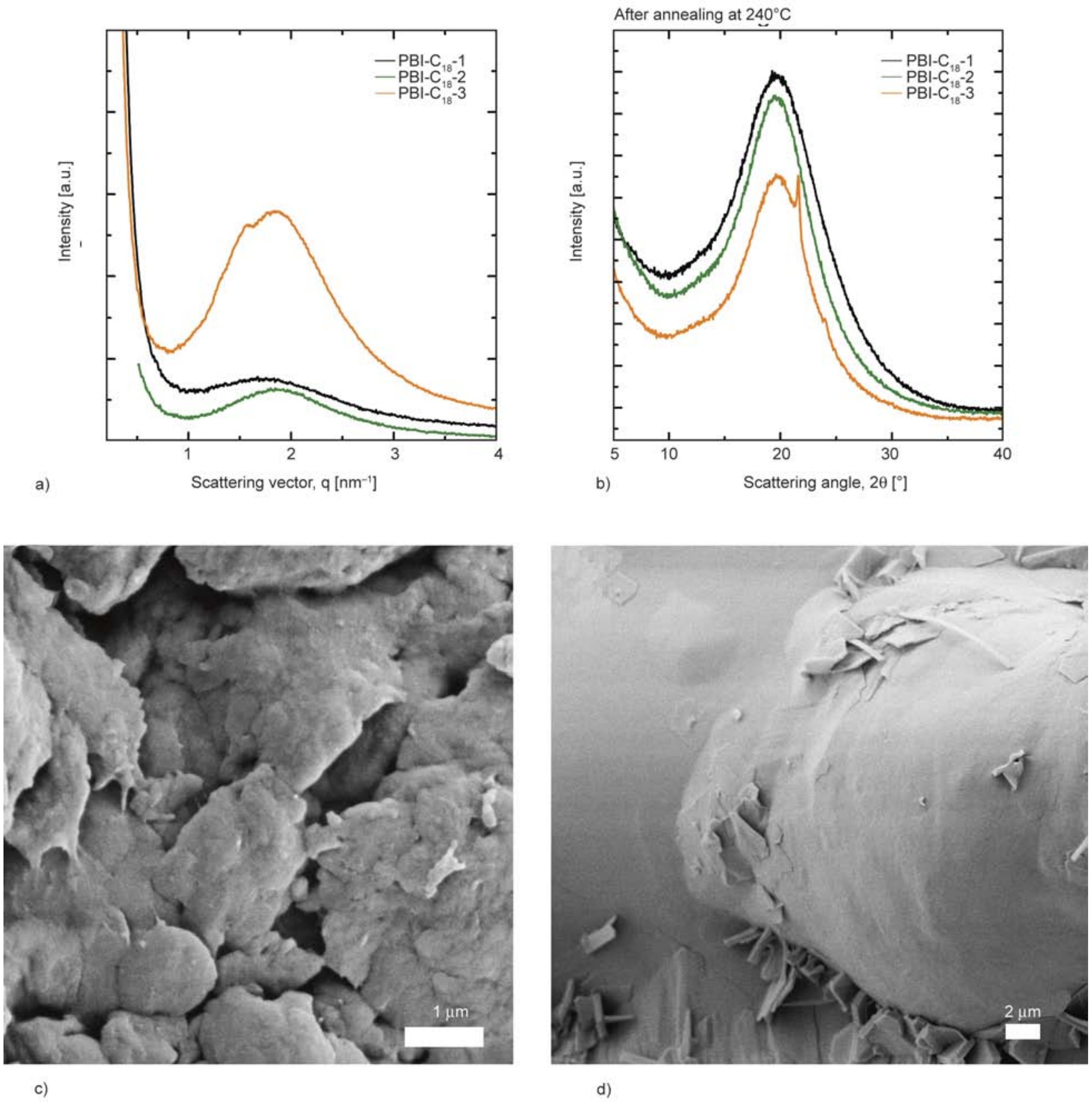

Figure 2. SAXS (a) and WAXS (b) patterns of the modified PBIs (after annealing of the powders at 240°C); SEM picture of annealed powders: PBI-C_{18}-2 (c) and PBI-C_{18}-3 (d)

visible clearly, probably as a consequence of the lower alkyl content and the reduced ability to undergo microphase separation into well-defined morphologies.

The observed peaks were rather broad in all cases. This can be interpreted as a consequence of small-sized ordered domains coexisting with a microphase-separated morphology of only short range order.

3.2. Conductivity

We analyzed the proton conductivity σ of the phosphoric acid doped PBI graft copolymers preliminary in order to get a first idea on the effect of the nanostructuration on σ. Hence, no temperature dependency was studied within this communication. For better comparability, we measured also the proton conductivity of a plain PBI membrane after phosphoric acid doping. This gives us some 'internal' standard as it is known that the conductivity of PA doped PBI can depend on the processing history (sol-gel doping, used solvent for membrane casting, gel methodology) [23–25]. The phosphoric acid doped membranes were dried under vacuum at 60°C for 16 hours before performing the measurements. The membranes were contacted between

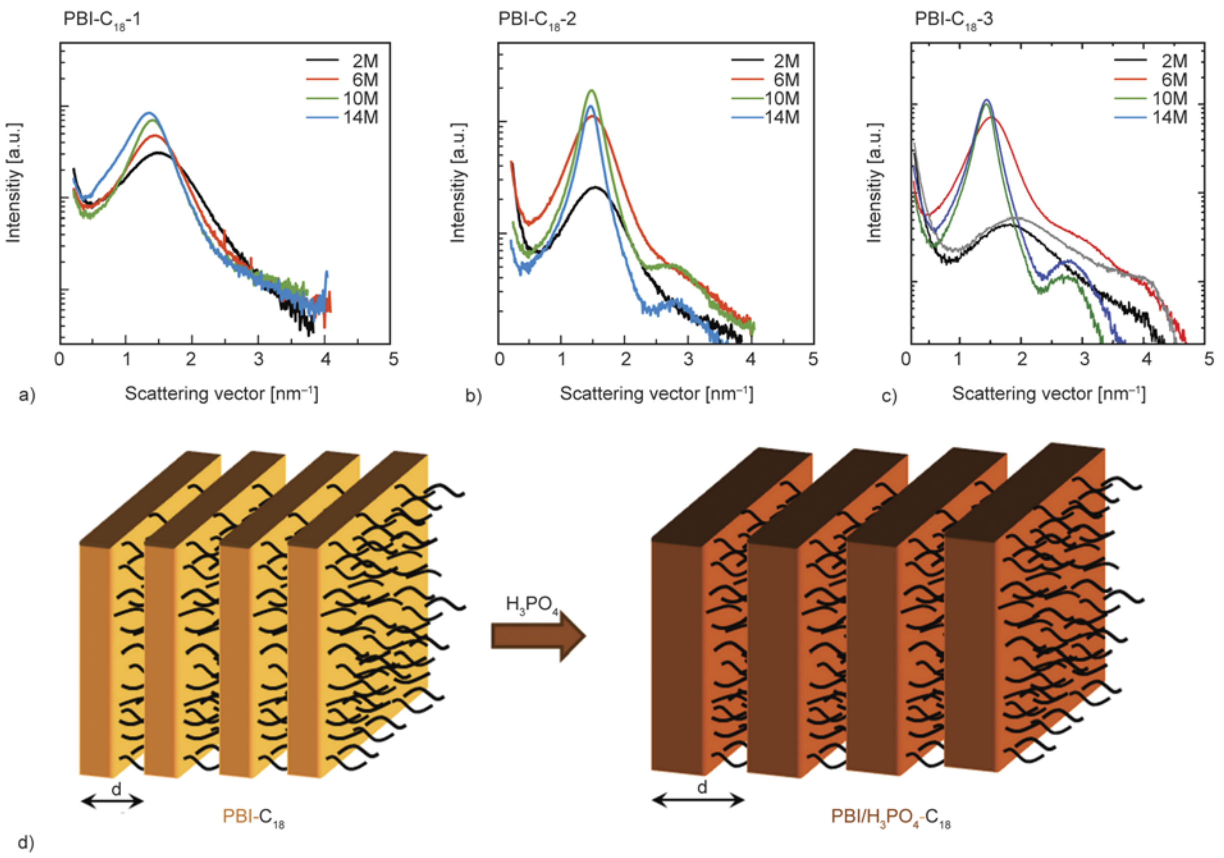

Figure 3. SAXS patterns of phosphoric acid doped PBI membranes: (a) PBI-C_{18}-1; (b) PBI-C_{18}-2; (c) PBI-C_{18}-3 and (d) schematic idealized drawing of the layer expansion upon acid doping

platinum foils and sealed to the external atmosphere; hence the measurements were done under rather low humidity (<5–10%). The measurements were done using an impedance analyzer.

Figure 4a shows the proton conductivity of PBI and PBI-C_{18}-3 in dependence of the acid doping. It becomes clear that the conductivity upon acid doping gets reduced if the PA is confined into a microphase-separated morphology. This is not surprising, as the total number of charge carriers get reduced upon grafting in accordance with the lower phosphoric acid uptake compared to plain PBI mem-

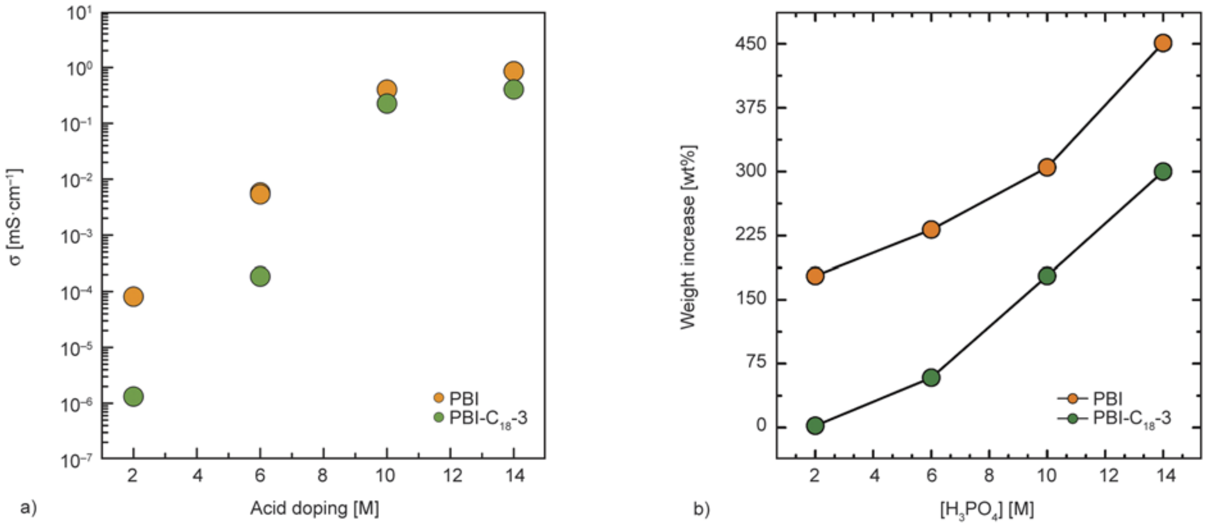

Figure 4. (a) proton conductivity of a pure PBI membrane and PBI-C_{18}-3 in dependence of the acid doping level (measured after vacuum drying in a closed cell at room temperature (22.4°C) relative humidity of the surrounding: 16%); (b) weight increase of a PBI and PBI-C_{18}-3 membrane upon doping with phosphoric acid and vacuum drying

branes [26]. Nevertheless, the conductivity is in an acceptable range, which indicates that the PBI domains should be well connected. Furthermore, there are reports on increased proton hopping rates for doped ionic liquids, which are confined in microphase separated domains of block copolymers. The effect was believed to be related to a changed polymer morphology (chain stretching), which has some kind of back-coupling effects on the hydrogen-bond structure [26]. The results presented here can at the present stage however not give an indication, whether comparable effects could be also true in the modified and acid-doped PBI membranes. However, the preliminary results show in accordance with earlier reports that comparable proton conductivities can be reached in nanostructured PBI at lower PA content [10].

4. Conclusions

The present work shows that nanostructured PBI membranes can be obtained after N-alkylation with long (C_{18}) alkyl chains. Polymers of different degrees of alkylation were prepared and characterized by a variety of methods. While the microphase separation is only weak at low degree of alkylation, it can be enhanced by larger amounts of incorporated alkyl chains. Membranes can be formed and doped with phosphoric acid. As a consequence of the non-polar alkyl chains the total acid uptake is lower compared to plain PBI. The acid populates the PBI domains, thereby increasing the segregation tendency between the non-polar alkyl chains and the PBI backbone. This results in the formation of lamellar domains as evidenced by SAXS experiments. The proton conductivity of the modified membranes was found to be lower than that of the pure PBI, but no detailed analysis has been carried out within this communication yet. Nevertheless, the present study opens the possibility to study the impact of the 2D like confinement of the phosphoric acid and the presence of a large amount of interfaces on the proton conductivity in more detail.

References

[1] Kreuer K. D.: On the development of proton conducting polymer membranes for hydrogen and methanol fuel cells. Journal of Membrane Science, **185**, 29–39 (2001).
DOI: 10.1016/S0376-7388(00)00632-3

[2] Kreuer K-D., Paddison S. J., Spohr E., Schuster M.: Transport in proton conductors for fuel-cell applications: Simulations, elementary reactions, and phenomenology. Chemical Reviews, **104**, 4637–4678 (2004).
DOI: 10.1021/cr020715f

[3] Gebel G., Diat O.: Neutron and X-ray scattering: Suitable tools for studying ionomer membranes. Fuel Cells, **5**, 261–275 (2005).
DOI: 10.1002/fuce.200400080

[4] Schmidt-Rohr K., Chen Q.: Parallel cylindrical water nanochannels in nafion fuel-cell membranes. Nature Materials, **7**, 75–83 (2008).
DOI: 10.1038/nmat2074

[5] Wainright J. S., Wang J-T., Weng D., Savinell R. F., Litt M.: Acid-doped polybenzimidazoles: A new polymer electrolyte. Journal of the Electrochemical Society, **142**, 121–123 (1995).
DOI: 10.1149/1.2044337

[6] Asensio J. A., Sánchez E. M., Gómez-Romero P.: Proton-conducting membranes based on benzimidazole polymers for high-temperature PEM fuel cells. A chemical quest. Chemical Society Reviews, **39**, 3210–3239 (2010).
DOI: 10.1039/b922650h

[7] Vilciauskas L., Paddison S. J., Kreuer K-D.: Ab initio modeling of proton transfer in phosphoric acid clusters. The Journal of Physical Chemistry A, **113**, 9193–9201 (2009).
DOI: 10.1021/jp903005r

[8] Weber J., Kreuer K-D., Maier J., Thomas A.: Proton conductivity enhancement by nanostructural control of poly(benzimidazole)-phosphoric acid adducts. Advanced Materials, **20**, 2595–2598 (2008).
DOI: 10.1002/adma.200703159

[9] Weber J., Antonietti M., Thomas A.: Mesoporous poly (benzimidazole) networks via solvent mediated templating of hard spheres. Macromolecules, **40**, 1299–1304 (2007).
DOI: 10.1021/ma062598m

[10] Lee H-S., Roy A., Lane O., McGrath J. E.: Synthesis and characterization of poly(arylene ether sulfone)-*b*-polybenzimidazole copolymers for high temperature low humidity proton exchange membrane fuel cells. Polymer, **49**, 5387–5396 (2008).
DOI: 10.1016/j.polymer.2008.09.019

[11] Mader J. A., Benicewicz B. C.: Synthesis and properties of segmented block copolymers of functionalised polybenzimidazoles for high-temperature PEM fuel cells. Fuel Cells, **11**, 222–237 (2011).
DOI: 10.1002/fuce.201000085

[12] Ng F., Bae B., Miyatake K., Watanabe M.: Polybenzimidazole block sulfonated poly(arylene ether sulfone) ionomers. Chemical Communications, **47**, 8895–8897 (2011).
DOI: 10.1039/c1cc12266e

[13] Sivanandan K., Chatterjee T., Treat N., Kramer E. J., Hawker C. J.: High surface area poly(3-hexylthiophenes) thin films from cleavable graft copolymers. Macromolecules, **43**, 233–241 (2010).
DOI: 10.1021/ma902009q

[14] Gieselman M. B., Reynolds J. R.: Water-soluble polybenzimidazole-based polyelectrolytes. Macromolecules, **25**, 4832–4834 (1992).
DOI: 10.1021/ma00044a056

[15] Klaehn J. R., Luther T. A., Orme C. J., Jones M. G., Wertsching A. K., Peterson E. S.: Soluble N-substituted organosilane polybenzimidazoles. Macromolecules, **40**, 7487–7492 (2007).
DOI: 10.1021/ma062186d

[16] Kumbharkar S. C., Kharul U. K.: New *N*-substituted ABPBI: Synthesis and evaluation of gas permeation properties. Journal of Membrane Science, **360**, 418–425 (2010).
DOI: 10.1016/j.memsci.2010.05.041

[17] Maity S., Sannigrahi A., Ghosh S., Jana T.: N-alkyl polybenzimidazole: Effect of alkyl chain length. European Polymer Journal, **49**, 2280–2292 (2013).
DOI: 10.1016/j.eurpolymj.2013.05.011

[18] Vogel H., Marvel C. S.: Polybenzimidazoles, new thermally stable polymers. Journal of Polymer Science, **50**, 511–539 (1961).
DOI: 10.1002/pol.1961.1205015419

[19] Musto P., Karasz F. E., MacKnight W. J.: Fourier transform infra-red spectroscopy on the thermo-oxidative degradation of polybenzimidazole and of a polybenzimidazole/polyetherimide blend. Polymer, **34**, 2934–2945 (1993).
DOI: 10.1016/0032-3861(93)90618-K

[20] Conti F., Willibold S., Mammi S., Korte C., Lehnert W., Stolten D.: Carbon NMR investigation of the polybenzimidazole–dimethylacetamide interactions in membranes for fuel cells. New Journal of Chemistry, **37**, 152–156 (2012).
DOI: 10.1039/C2NJ40728K

[21] Yuan J., Soll S., Drechsler M., Müller A. H. E., Antonietti M.: Self-assembly of poly(ionic liquid)s: Polymerization, mesostructure formation, and directional alignment in one step. Journal of the American Chemical Society, **133**, 17556–17559 (2011).
DOI: 10.1021/ja207080j

[22] Thünemann A. F.: Polyelectrolyte–surfactant complexes (synthesis, structure and materials aspects). Progress in Polymer Science, **27**, 1473–1572 (2002).
DOI: 10.1016/S0079-6700(02)00017-5

[23] Ma Y-L., Wainright J. S., Litt M. H., Savinell R. F.: Conductivity of PBI membranes for high-temperature polymer electrolyte fuel cells. Journal of the Electrochemical Society, **151**, 8–16 (2004).
DOI: 10.1149/1.1630037

[24] Xiao L., Zhang H., Scanlon E., Ramanathan L. S., Choe E-W., Rogers D., Apple T., Benicewicz B. C.: High-temperature polybenzimidazole fuel cell membranes via a sol–gel process. Chemistry of Materials, **17**, 5328–5333 (2005).
DOI: 10.1021/cm050831+

[25] Sannigrahi A., Ghosh S., Maity S., Jana T.: Polybenzimidazole gel membrane for the use in fuel cell. Polymer, **52**, 4319–4330 (2011).
DOI: 10.1016/j.polymer.2011.07.013

[26] Hoarfrost M. L., Tyagi M. S., Segalman R. A., Reimer J. A.: Effect of confinement on proton transport mechanisms in block copolymer/ionic liquid membranes. Macromolecules, **45**, 3112–3120 (2012).
DOI: 10.1021/ma202741g

eXPRESS Polymer Letters Vol.8, No.1 (2014) 39–49
Available online at www.expresspolymlett.com
DOI: 10.3144/expresspolymlett.2014.5

Grafting of collagen onto interpenetrating polymer networks of poly(2-hydroxyethyl methacrylate) and poly(dimethyl siloxane) polymer films for biomedical applications

S. M. Rezaei, Z. A. Mohd Ishak[*]

School of Materials & Mineral Resources Engineering, Engineering campus, University Sains Malaysia, 14300 Nibong Tebal, Penang, Malaysia

Received 29 June 2013; accepted in revised form 1 September 2013

Abstract. Poly(dimethyl siloxane) (PDMS) films were modified using poly(2-hydroxyethyl methacrylate) (PHEMA) by sequential method of interpenetrating polymer networks (IPNs). Collagen (type I) was also linked onto the modified films via methyl sulfonyl chloride. Collagen reacted with the activated groups to obtain covalently linked protein layers. The surface properties of samples were characterised by attenuated total reflectance Fourier transform infrared spectroscopy (ATR-FTIR), X-ray photoelectron spectroscopy (XPS), scanning electron microscopy (SEM) and water contact angle measurements. Dynamic Mechanical Thermoanalysis (DMTA) and tensile testing were used to study the physical and mechanical properties of the IPNs.

Grafting of collagen on the surface was confirmed using ATR-FTIR and XPS. The results also showed that the hydrophilicity of modified samples increased as the content of PHEMA increased. The biocompatibility of the PDMS surface was evaluated by culture of fibroblast cells (L929). The collagen-linked surfaces showed significant cell adhesion and growth in comparison with unmodified PDMS samples.

Keywords: *biocompatible polymers, poly(dimethyl siloxane), interpenetrating polymer network, collagen, hydrophilicity*

---

1. Introduction

Polymeric biomaterials have played an important role in medical therapy, finding applications in areas such as implantable medical devices and artificial organs, ophthalmology, dentistry, bone repair, drug delivery systems and many other medical fields. These biomaterials are easily fabricated into products with various shapes at reasonable cost. Despite possessing desirable mechanical and physical properties, these materials have one major drawback, i.e., biocompatibility, that limits their applicability [1]. Depending on the proposed medical application, all biomaterials are evaluated in terms of biocompatibility. Biocompatibility can be defined as the acceptance of an artificial material by the surrounding tissues and the body as a whole. It is commonly accepted that this term means not only a lack of cytotoxic effects, but also positive effects in the sense of biofunctionality [2, 3].

PDMS-based materials have been mostly used in biomedical applications as soft tissue substitutes because of their excellent softness, stability and inertness. However, serious problems have occurred when silicone devices are implanted for long periods of time [4, 5]. These include damage to the tissues in direct contact through mechanical friction

---

[*]Corresponding author, e-mail: zarifin@eng.usm.my

and dense fibrous tissue formation around the surface, without bulk deterioration. On the other hand, cell attachment on PDMS is rather low due to its hydrophobicity [6]. One approach to solving these problems is the fixation of a biocompatible layer on the surface of the polymer to improve cellular interactions by covalent grafting of a coupling agent and suitable macromolecular chains. In recent years, a large number of research groups have studied protein immobilisation on polymer surfaces to improve biocompatibility [7–9]. Fixing of some special biologically active molecules on synthetic materials is of critical importance since they can, in principle, elicit some specific, predictable and controlled responses from the cells seeded on the materials. Among the different types of natural materials, collagen is one of the most important biological macromolecules of the extracellular matrix in tissues. Collagen has been successfully used to produce biomaterials for a wide range of applications, including burn healing and the strengthening of soft tissue [10–14]. In order to covalently link protein molecules on an inert polymer surface such as PDMS, it is necessary to introduce reactive groups such as hydroxyl, carboxyl or amino groups on the polymer surface [15].

Hydrogels with desirable functional groups and high hydrophilicity have received considerable attention as excellent biomaterials. Among the many important hydrogels, PHEMA is the first one that has been successfully employed for biological use. PHEMA is known as a hydrogel with good biomedical properties. Applications of PHEMA are versatile and it has been engaged in injectable polymeric systems, nasal cartilage, ophthalmic applications, drug delivery systems, artificial corneas and wound dressings [16–20]. There are many reports in the literature for improving the surface properties of silicone using hydrogels by laser, plasma, corona discharge and particulate composites methods [21–27]. Another option for modifying PDMS by hydrogels is to form an interpenetrating polymer network [28–31] . Interpenetrating polymerisation is the only way of combining cross-linked polymers. This technique can be used to combine two or more polymers into a mixture in which phase separation is not as extensive as it would be otherwise [32]. In the present work, PDMS/PHEMA film was prepared via IPN to improve the hydrophilicity of PDMS. The functional groups of PHEMA on the silicone surface were covalently coupled with collagen via a coupling agent to improve the cell adhesion properties of PDMS. Thus, incorporating PHEMA and collagen onto the silicone surface may give silicone substrates new and interesting properties for applications in silicone-based implantable biomaterials.

2. Experimental

2.1. Materials

The materials used are listed in Table 1. HEMA was redistilled under vacuum. Azobisisbutyronitrile (AIBN) was recrystallised twice from methanol. Ethylen glycol dimethacrtylate (EGDMA) was used as received. Medical grade PDMS was used without any further purification. All other chemicals used in this study were of reagent grade and were used as received.

Table 1. Materials used

Designation	Description	Source
HEMA	2-Hydroxyethyl methacrylate	Merck Co.
AIBN	α,ά-Azoisobutyronitrile	Fluka Co.
EGDMA	Ethylene glycol dimethacrylate	Merck Co.
–	Toluene	Merck Co
–	Ethanol	Riedel Co.
PDMS	Silastic MDX4-4210	Dow Corning Co.
Col	Collagen type I	Sigma Aldrich
–	Methyl sulfonyl chloride	Sigma Aldrich
–	Diethyl ether	Sigma Aldrich

2.2. PDMS vulcanisation

Medical grade PDMS (Silastic MDX4-4210) is a two-component product. The elastomer component of PDMS was mixed with 10% w/w curing agent part. After thorough mechanical stirring, the mixture was degassed. The PDMS sheets were prepared by compression moulding (GOTECH, GT-7014-A) (250 psi/1,75 MPa/, 75°C, 30 min), followed by a post-curing process at 120°C for a period of 2 h to establish the physical properties.

2.3. Preparation of IPN

The PDMS films were immersed at room temperature for 24 h in a swelling solution of HEMA (monomer), EGDMA (crosslinker) and AIBN (initiator) in toluene. The swollen samples were suspended in a sealed glass reactor. The initiator and crosslinker concentration were fixed at 0.2 and 2 wt% with respect to the amount of monomer, respectively. The temperature was then raised and kept at 80°C for 3 h to allow HEMA, EGDMA and

AIBN to react. The obtained IPNs were kept at 90°C for 4 h to complete polymerisation of the monomer. The produced IPNs were immersed in ethanol for 24 h, followed by Soxhlet extraction in distilled water for 48 h to remove homopolymers and unreacted monomers. The specimens were then dried until constant weight under vacuum at 50°C. The PHEMA content of the IPNs was calculated as shown by Equation (1):

$$\text{PHEMA content}\,[\,\%\,] = \frac{w_{\text{IPN}} - w_0}{w_{\text{IPN}}}\cdot 100 \qquad (1)$$

where w_{IPN} is the weight of the IPN and w_0 is the weight of the unmodified PDMS sample. Samples of IPNs, which contained approximately 30% PHEMA, were then selected for collagen grafting. These compositions have been reported as the optimum composition to give good biocompatibility and physical and mechanical properties [6].

2.4. Collagen grafting

IPN films were introduced into a glass tube containing 2 mL of methyl sulfonyl chloride and 20 mL of diethyl ether to activate hydroxyl groups in the PHEMA chains. After incubation at 20°C for 3 h, the activated films were immersed into a collagen solution at 4°C for 24 h to allow the activated hydroxyl groups in the PHEMA chains and the amino groups in the protein to form covalent bonds. The concentration and pH of the collagen solution were 1 mg·mL^{-1} and 3.0, respectively. Collagen-grafted PDMS films were rinsed with distilled water and the samples were stored at 4°C before use. Figure 1 shows the schematic diagram of the reaction of collagen-grafted PDMS/PHEMA IPN films.

2.5. Characterisation

Stress–strain measurements were carried out using an Instron (3366) tensile tester on dumbbell-shaped samples with a thickness of 1 mm. The tests were performed with a speed of 50 mm·min^{-1} at room temperature. The hardness of the samples was measured using a Shore-A durometer. Five specimens were measured for each composition. The elongation at break, tensile strength and hardness were obtained by averaging the results of five specimens. To characterise the surface of modified samples, infrared spectra were obtained on a Fourier transform infrared (FT-IR) spectrophotometer (Perkin Elmer-Spectrum one) using an attenuated total reflection (ATR) method. The collagen grafting on the PDMS/PHEMA IPN surface was analysed by X-ray photoelectron spectroscopy (XPS). An Omicron X-PS system (ELS5000, Germany) with an unmonochromated aluminum Al K_α source (1486:6 eV) was run to record the XPS spectra of the samples. The emission angle from the X-ray detector with respect to the sample surface was 90º. Scanning electron microscopy (FESEM, ZEISS–SUPRA 35 VP) was performed on gold-coated samples using a sputter coater. A SEM typically operating at 10 kV was employed for morphological observation. Static water contact angles were investigated on the swollen samples in water for 24 h using the sessile drop method with contact-angle measurement equipment (KRUSS- K12). The swollen samples were dried with filter paper before water contact angle measurements were acquired. All results of the water contact angles were the average value of five measurements on different parts of the sample.

Dynamic mechanical thermal analysis measurements (DMTA) were conducted using a Polymer-Lab DMTA analyser (Mettler Toledo DMA 861) at 10 Hz over a temperature range of –150 to 150°C and at a heating rate of 2°C/min in the bending mode under a dry nitrogen flow.

2.6. Cell culture study

Cell adhesion was determined with the mouse L929 fibroblast cell line (purchased from ATTC). The cells were maintained in Dulbecco's modified eagle's medium (DMEM) supplemented with 100 IU/mL

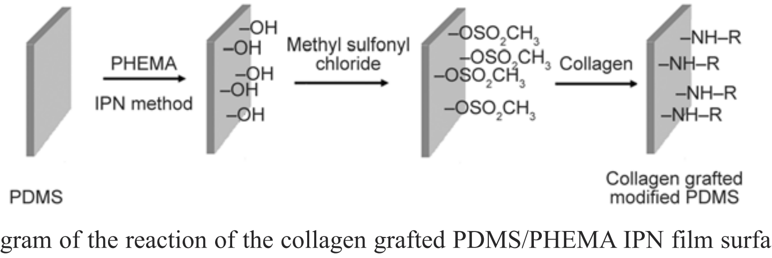

Figure 1. Schematic diagram of the reaction of the collagen grafted PDMS/PHEMA IPN film surface. HN–R represents a collagen molecule

penicillin, 100 µg/mL streptomycin (Gibco BRL) and 10% fetal calf serum (Gibco BRL). A routine subculture was used to maintain the cell line. The cells were incubated in a humidified atmosphere of 5% CO_2 at 37°C. After 1 week of incubation, the monolayer was harvested by trypsinisation. A cell suspension of $3\cdot10^5$ cells/mL was prepared before seeding. The samples were sterilised in 70% alcohol and washed in culture medium before the cell seeding procedure. They were then placed in a multi-well tissue culture polystyrene plate with the cell suspension and maintained in an incubator for 72 h. After incubation, the samples were removed from the incubator and washed immediately in phosphate-buffered saline (PBS). The cells were fixed in graded alcohol (60, 70, 80 and 99%) and stained with 5% Giemsa for optical microscopic examinations (OLYMPUS- BX51M). All samples were run in duplicate and approximately 10 objective fields were randomly chosen in the central and peripheral regions of each sample.

3. Results and discussion

3.1. Tensile properties

Tensile tests were carried out to study the hydrogel effect on the mechanical properties of the PDMS, and the results are shown in Table 2. As can be seen, the IPN samples up to approximately 30 wt% of PHEMA reveal good tensile strengths and elongations at break in comparison to the PDMS. The tensile strength and elongation at break of the PDMS/ PHEMA IPN samples were gradual lower than that of PDMS, based on the weak mechanical properties of PHEMA, these results are acceptable because the hydrophilicity of these IPNs were significantly improved. In addition, for samples with approximately 31.7 wt% PHEMA, tensile strength and elongation at break were about 15% lower than that of the unmodified sample. The hardness values of the IPN systems were in agreement with the results of the elongation measurements because harder polymers show lower elongations at break.

Table 2. Hardness (Shore A), tensile strength and elongation at break percentage of PDMS/PHEMA IPN

PHEMA % in IPN	Hardness	Tensile strength [MPa]	Elongation [%]
0	35±0.16	5.4±0.03	493±1.41
10.5	37±0.35	5.1±0.06	475±2.47
19.4	40±0.57	4.8±0.12	443±3.35
31.7	43±0.16	4.5±0.02	427±1.27
40.8	51±0.48	3.6±0.08	340±4.26

3.2. Surface characterisation by ATR-FTIR

Surface characterisation of the PDMS samples was performed by comparing the ATR-FTIR spectra of unmodified and modified PDMS. Figure 2 shows the spectra of the samples. The absorption bands at approximately 1005 cm^{-1} are the characteristic absorption bands for –Si–O–Si– groups of PDMS polymers (Figure 2 curve a). The absorption bands appearing at approximately 1715 cm^{-1} are the characteristic absorption bands for carbonyl groups, which confirm the presence of PHEMA on the surface (Figure 2 curve b). A broad adsorption that appeared at 3100–3600 cm^{-1} confirms that the collagen was linked onto the functional group of the PDMS/ PHEMA IPN by the coupling agent (Figure 2 curve c). This figure indicated that ~3350 cm^{-1} was the adsorption peak of hydrogen bonding and ~3150 cm^{-1} was the peak for N–H bonds of collagen. In addition, the absorption at ~1600 cm^{-1} confirms the presence of amide bonds on the collagen-grafted film surfaces that were associated with carbonyl groups. Hence, it was concluded that grafting occurred on the film surface.

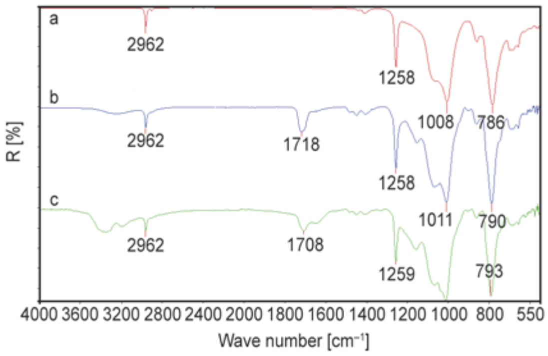

Figure 2. FTIR-ATR spectra of (a) unmodified PDMS; (b) PDMS/PHEMA IPN with 31.7 wt% PHEMA; and (c) collagen grafted PDMS/PHEMA IPN

3.3. XPS study

Figure 3a depicts the XPS wide scan spectrum of the PDMS surface. It shows a spectrum consisting of the electrons of oxygen (O 1s), carbon (C 1s), and silicones (Si 2s and Si 2p). The peaks of these elements occurred in the regions around 533, 285, 153 and 103 eV, respectively. The spectrum of the PDMS/PHEMA IPN film surface (Figure 3b) also

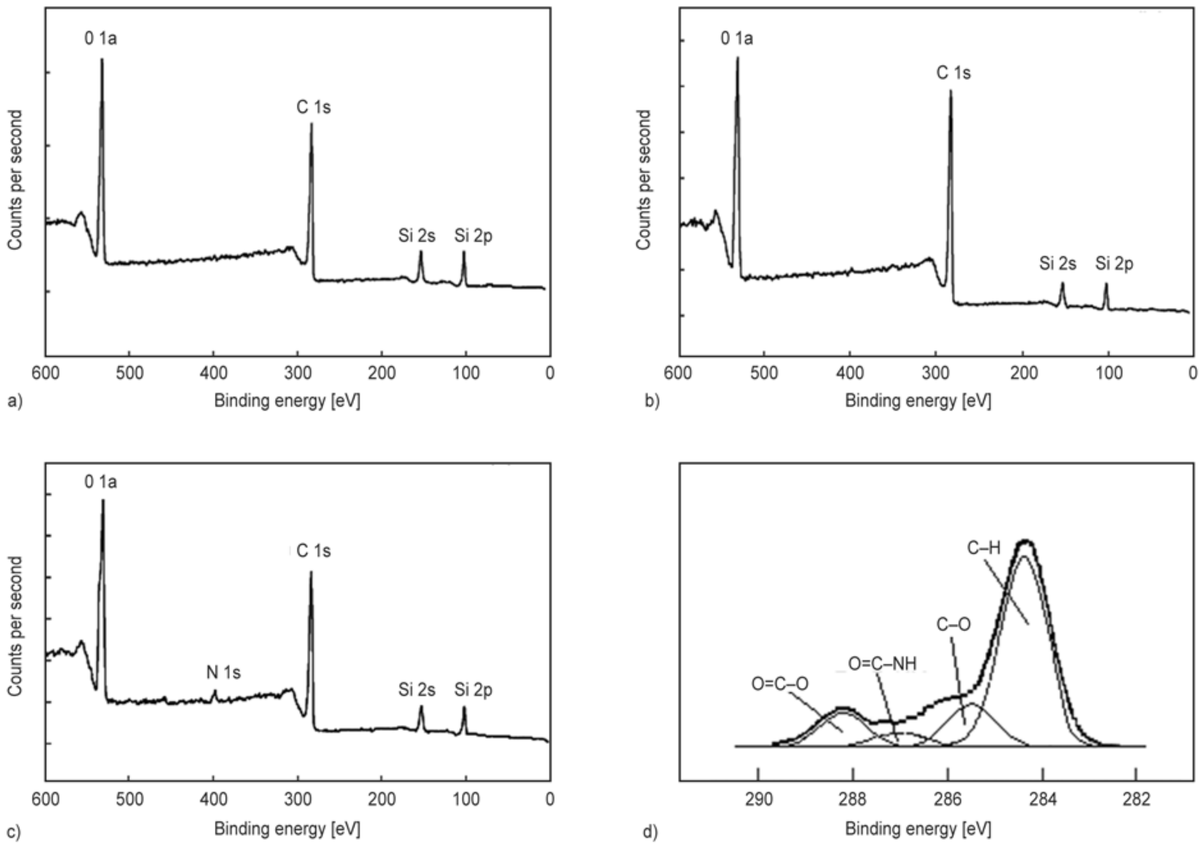

Figure 3. XPS wide scan spectra of (a) unmodified PDMS; (b) PDMS/PHEMA IPN with 31.7 wt% PHEMA; (c) collagen-grafted PDMS/PHEMA IPN and (d) high resolution C1s spectrum for the collagen grafted PDMS/PHEMA IPN

showed the same peaks as the PDMS surface. However, the relative intensity of the carbon and oxygen peaks varied after formation of the PHEMA IPNs. In contrast, a new peak corresponding to N 1s at around 400 eV appeared in the spectrum of the collagen-grafted film surface (Figure 3c). The wide scan and low-resolution spectra were performed to establish which elements were available on the various surfaces. N ls was only present on the modified surface grafted with collagen. Therefore, collagen was successfully introduced onto the modified surfaces based on this spectrum. Figure 3d shows the respective C 1s core-level spectra of the samples. In the case of the PDMS/PHEMA IPN film surface, the C 1s core level spectrum contained three major peak components with binding energies at 284.6, 286.2 and 288.6 eV, corresponding to carbon atoms of hydrocarbons, carbon atoms with a single bond to oxygen and carbon atoms in carbonyl groups. After collagen grafting onto the film surface, the C 1s core level was curve-fitted with four peak components with binding energies at 284.6 eV for the C–H species, 286.2 eV for the C–O species, 287.4 eV for the O=C–NH– species and 288.6 eV for the O–C=O species.

3.4. Contact angle study

One of the best ways to improve the hydrophilicity of a given polymer surface is to allow water to engage its preferred interaction with the surface, i.e., the short-range hydration, acid–base and hydrogen bonding interactions. The presence of hydrophilic groups on the surface of the PDMS/PHEMA IPNs was confirmed by surface characterisation methods. The wettability of the unmodified and modified films was studied using static water contact angles. As can be seen in Figure 4, the surface wettability of the modified PDMS film was obviously increased compared with the unmodified PDMS film, which showed a relatively high contact angle. The water contact angle of the pure PDMS surface was 104.6°; while after modification, the water contact angle of PDMS/PHEMA IPN with 31.7 wt% PHEMA dropped to 58.6°. Increasing PHEMA content in the IPNs was observed to decrease the contact angles of the samples. The water contact angles for various

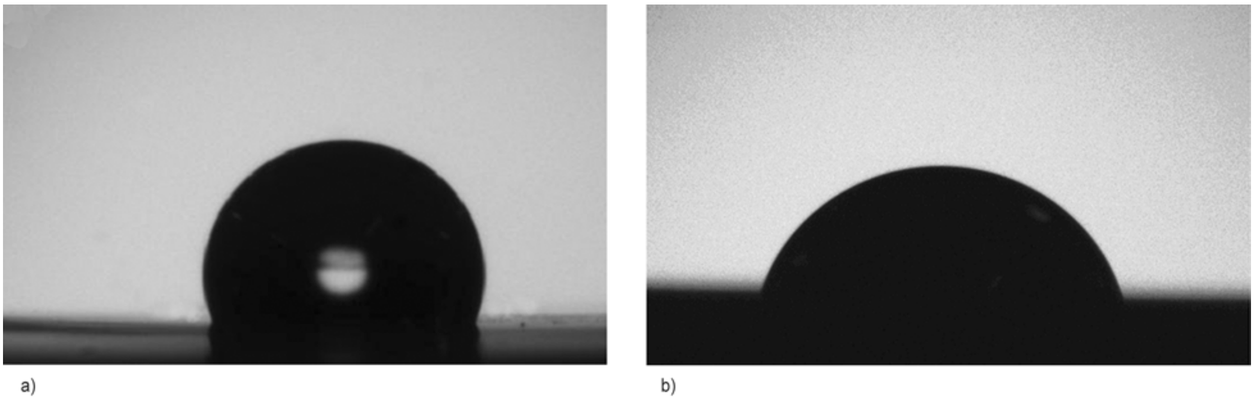

Figure 4. Contact angle measurement images with water on (a) unmodified PDMS and (b) PDMS/PHEMA IPN with 31.7 wt% PHEMA

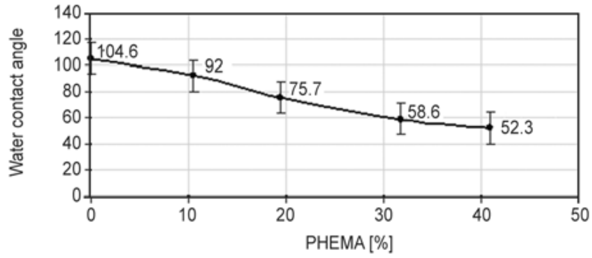

Figure 5. Water contact angle of the unmodified and modified PDMS IPNs films with different amounts of PHEMA

amounts of PHEMA IPN films were measured to examine the change in wettability of the samples. In Figure 5, it can be seen that the IPN films showed a considerable decrease in water contact angle compared to the unmodified PDMS. The water contact angle dramatically decreased from 104.6 to 52.3° as the content of PHEMA increased. Furthermore, the contact angle for collagen linked onto IPN films was 65°. In fact, the contact angle of the collagen-linked IPN film slightly increased. Consequently, the hydrophilicity of the modified PDMS film was maintained. The wettability of the PDMS film was therefore increased in each of the modified samples. The basis of surface hydrophilisation is to maximise hydration and hydrogen bonding interactions. Hydroxyl, carbonyl and carboxyl groups contain lone pairs, unshared electrons and asymmetric charge distributions. Many types of oxygen-containing organic functional groups can interact with water more effectively than the methyl groups of PDMS. For these reasons, higher PHEMA-containing IPNs have lower water contact angles.

3.5. Morphological study

The surface appearance of the unmodified and PDMS/PHEMA IPN samples are shown in scanning electron micrographs in Figure 6a and 6b. Both unmodified and modified samples had a smooth surface without any contrast. As can be seen, there was no difference between the unmodified and modified PDMS morphology in accessible magnification of the SEM by this method. This indicates that the dimensions of the hydrophilic phase were smaller than the micron scale. According to the nature of sequential IPNs, the distribution of monomer before establishment as a second network is the molecular dimension [32]. The second network in the composition of any percentage that functions as a dispersed phase is submicron and will not be detectable by SEM in surface appearance of samples. However, as shown in Figure 6d, the SEM micrograph of the cross section IPN sample clearly confirms the appearance of two phases. It can be seen that PHEMA as the second network are homogeneously distributed throughout the PDMS film. The presence of distributed PHEMA in the PDMS matrix increases the hydrophilicity of the IPN samples that is in agreement with the water contact angle results. Additionally, Figure 6c shows the cross section of pure PDMS sample that there is no additional phase. The surface morphology of collagen grafted PDMS/PHEMA IPN was observed by SEM (Figure 6e). A comparative morphology was made between collagen grafted IPN film and PDMS films that the surface morphology of collagen grafted IPN were different.

3.6. Dynamic mechanical thermal analysis (DMTA)

Figure 7 shows the DMTA results of the PDMS and PDMS/PHEMA IPN. As can be seen, in the area of the glass transition of the components, the curve corresponding to the PDMS exhibits a distinct tan δ

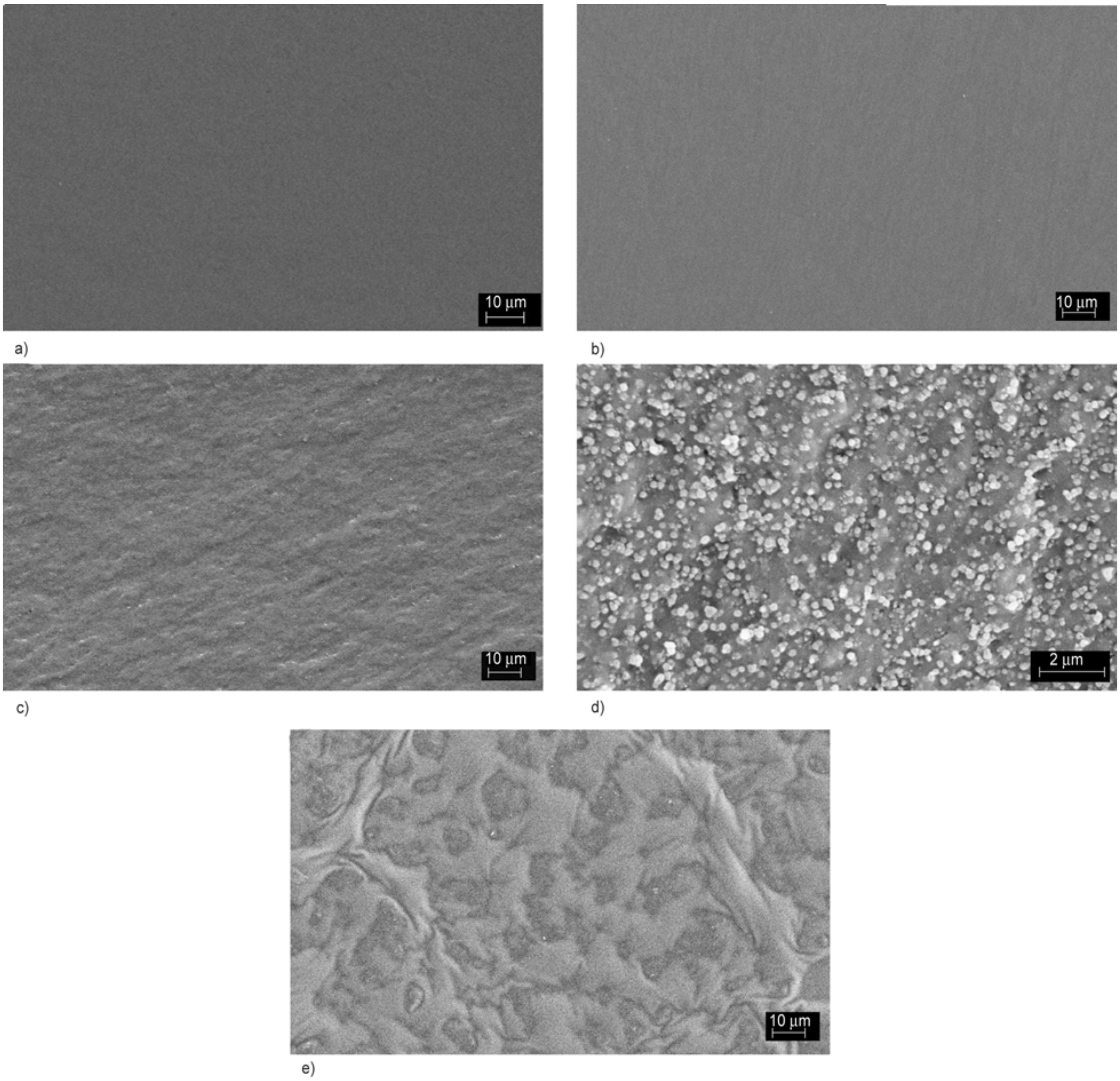

Figure 6. SEM showing surface appearance of (a) unmodified PDMS; (b) PDMS/PHEMA IPN with 31.7 wt% PHEMA; (c) cross section of unmodified PDMS; (d) cross section of PDMS/PHEMA IPN with 31.7 wt% PHEMA; and (e) collagen grafted PDMS/PHEMA IPN

maximum at –37°C (Figure 7a), whereas for the PHEMA IPN, the glass–rubber transition occurs at 136°C (Figure 7c). The DMTA curves corresponding to IPNs with large PHEMA contents depict an obvious maximum in the region of the PHEMA α-transition (Figure 7d), however for small PHEMA contents, the curves depict a low maximum (Figure 7b). The storage modulus curves clearly show that there are two T_gs in the IPNs samples and these compounds are two phase polymeric system. The shapes of the temperature dependence of tan δ are typical for two-phase polymeric systems with incompatible components. Moreover, the lack of shifting maximum tan δ for PHEMA in IPNs from their position indicated substantially complete phase separation in IPNs form. The height of the damping peaks for each phase varied with IPN composition, while there was no approaching temperature in maximum tan δ between two components. As can be seen, DMTA results of IPNs display two main relaxations corresponding to the relaxations of PDMS and PHEMA, indicating that the separation phase occurs during these syntheses. The strong decay of E' from –37°C followed by a second decay of 136°C allows to assume that the continuous phase is PDMS and PHEMA macro domains dispersed in the con-

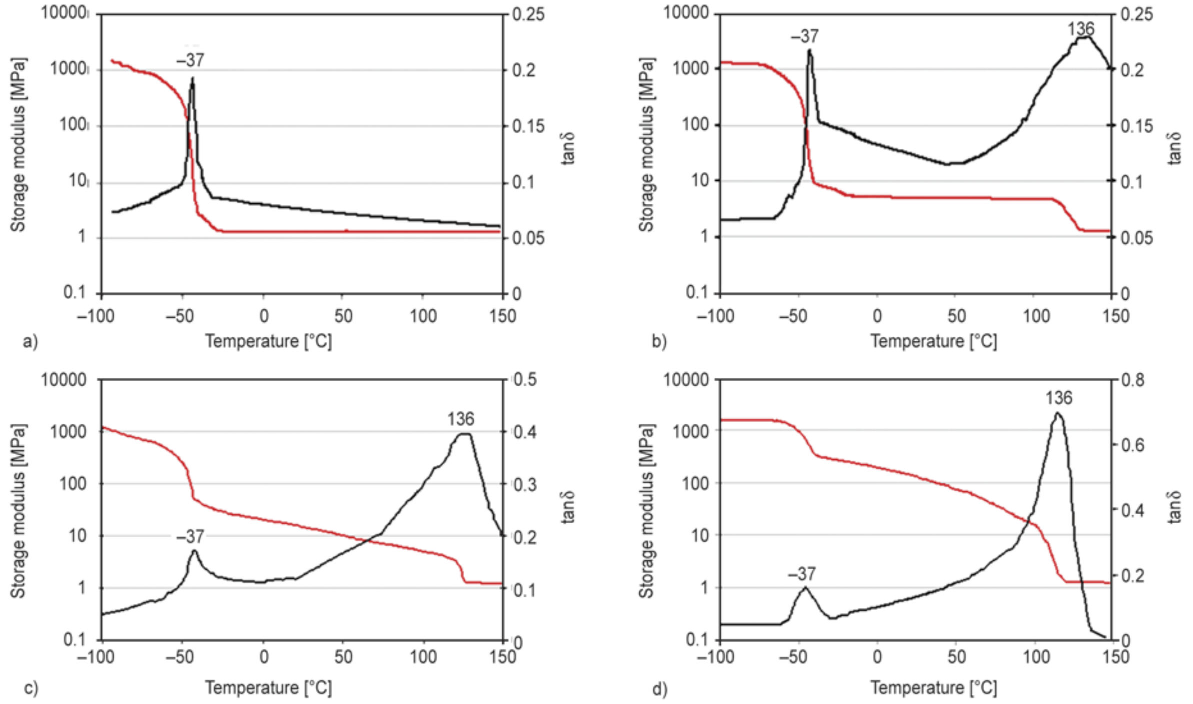

Figure 7. DMTA results curve of PDMS and PDMS/PHEMA IPN (a) PDMS, (b) PDMS/PHEMA IPN with 10.5 wt% PHEMA, (c) 31.7 wt% PHEMA, and (d) 40.8 wt% PHEMA

tinuous phase. This result is in agreement with the general assumption that the continuous phase in IPN is usually the cross-linked phase which is formed first and that second polymer is the dispersed phase [33].

3.7. Cell attachment and growth study

The cellular behaviour of a biomaterial is an important factor in determining its biocompatibility. The whole process of adhesion of the cells after contact with biomaterials consists of cell attachment, spreading and growth.

As mentioned earlier, before testing the biological response of the materials, IPN films were immersed in ethanol followed by Soxhlet extraction in distilled water in order to eliminate residual monomers that are potentially toxic.

The optical micrographs of the *in vitro* cell culture samples are presented in Figure 8. It can be seen that L929 fibroblast cells was attached to the PHEMA IPN surface (Figure 8b) and had grown without eliciting a toxic response. The cell areas attached on the film surface increased with the presence of PHEMA in the PDMS network. This indicated that the attached cells on the PHEMA IPN supported a higher degree of cell spreading and become flat in comparison with the unmodified PDMS (Figure 8a). The fibroblast cells appeared to be attached on the surface of the PHEMA IPN, whereas during the same culture period, the fibroblast cells on the unmodified PDMS were almost round. The difference between cell appearances was likely to be a function of surface chemistry and surface morphology. From a thermodynamic point of view, only materials with a minimal surface tension can provide good adhesive opportunities for cells. As seen in Figure 5, the water contact angle of the PDMS surface decreased with increasing incorporation of PHEMA into the PDMS network. The degree of cell spreading on the PHEMA IPN increased compared with unmodified PDMS. The higher degree of cell spreading on the PHEMA IPN may be attributable to the change in surface wettability of the PDMS surface. As can be seen in Figure 8c, cell adhesion, spreading and growth onto the collagen-grafted onto IPN films was better than with the IPN films. This was attributed to the presence of collagen, which provides a suitable substrate for cell growth. The proliferation of cells onto films grafted with collagen was normal. From the above results, the collagen-grafted films were shown to enhance the attachment and growth capability of the cells. Although wettability is an important factor for cell

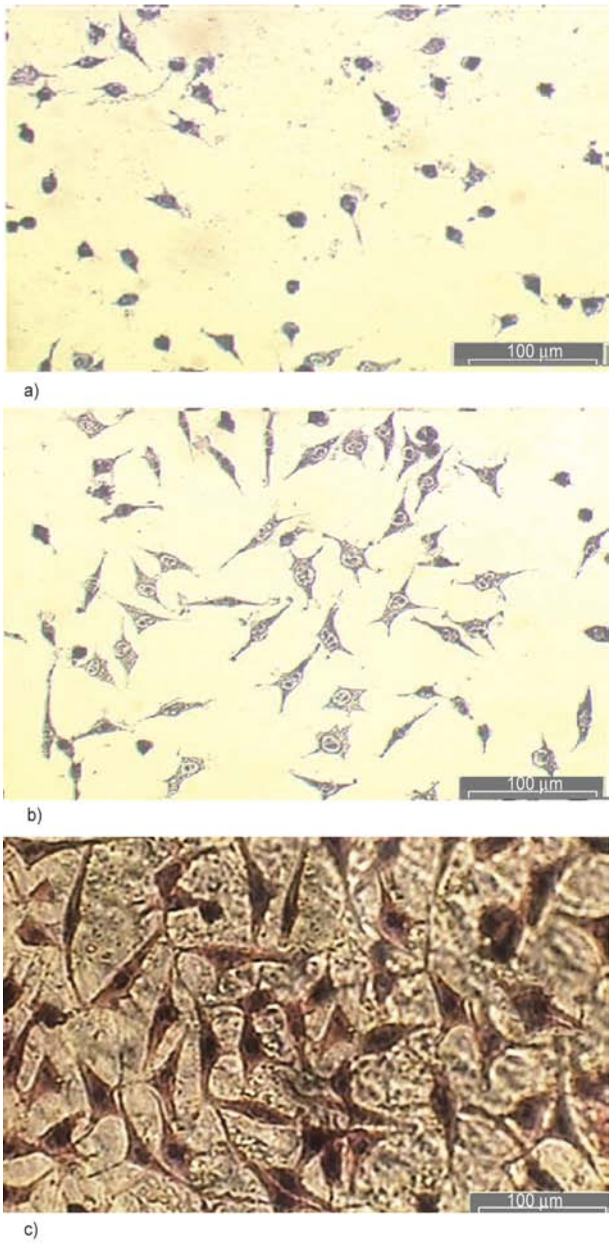

Figure 8. Optical micrographs of cell culture on (a) unmodified PDMS; (b) PDMS/PHEMA IPN with 31.7 wt% PHEMA; and (c) collagen grafted PDMS/PHEMA IPN

adhesion, spreading and growth onto polymer surfaces, surface chemistry or charge character are also very important factors.

4. Conclusions

Collagen-grafted PDMS/PHEMA IPN film was prepared to improve the biocompatibility of PDMS for biomedical applications. PHEMA hydrogel was first introduced onto the PDMS film by the IPN method. Through sulfonyl chloride chemistry, the reactive groups were subsequently used to graft collagen type I. XPS spectra and ATR-FTIR measurements confirmed the collagen grafting on the film surface. SEM and water contact angle surface analysis were performed to confirm the modification process. DMTA results of IPNs displayed two main relaxations corresponding to the relaxations of PDMS and PHEMA, indicating that the separation phase occurs in PDMS/PHEMA IPN system. The wettability of modified PDMS surfaces with and without collagen grafting was enhanced. However, the water contact angle of the PHEMA IPN films was less than that the collagen-grafted IPN film because collagen is a tendency hydrophobic material. Additionally, collagen-grafted film surfaces showed significant cell adhesion and growth in comparison with the PDMS/PHEMA IPN samples. This study provides a strategy for using a biomacromolecules that can potentially improve cellular interactions.

Acknowledgements

The authors gratefully acknowledge Prof. Rahmah Noordin and Dr. Ong Ming Thong of the Institute for Research in Molecular Medicine (INFORMM) for their assistance with cell culture tests.

References

[1] Park J., Lakes R. S.: Biomaterials. Springer, New York (2007).
DOI: 10.1007/978-0-387-37880-0

[2] Kirkpatrick C., Bittinger F., Wagner M., Köhler H., van Kooten T., Klein C., Otto M.: Current trends in biocompatibility testing. Proceedings of the Institution of Mechanical Engineers Part H: Journal of Engineering in Medicine, **212**, 75–84 (1998).
DOI: 10.1243/0954411981533845

[3] Říhová B.: Biocompatibility of biomaterials: Hemocompatibility, immunocompatiblity and biocompatibility of solid polymeric materials and soluble targetable polymeric carriers. Advanced Drug Delivery Reviews, **21**, 157–176 (1996).
DOI: 10.1016/S0169-409X(96)00404-8

[4] Khorasani M. T., Mirzadeh H., Sammes P. G.: Laser induced surface modification of polydimethylsiloxane as a super-hydrophobic material. Radiation Physics and Chemistry, **47**, 881–888 (1996).
DOI: 10.1016/0969-806X(95)00166-U

[5] Vladkova T.: Surface modification of silicone rubber with poly(ethylene glycol) hydrogel coatings. Journal of Applied Polymer Science, **92**, 1486–1492 (2004).
DOI: 10.1002/app.20001

[6] Cifcová I., Lopour P., Vondráček P., Jelínek F.: Silicone rubber-hydrogel composites as polymeric biomaterials: I. Biogical properties of the silicone rubber-p(HEMA) composite. Biomaterials, **11**, 393–396 (1990).
DOI: 10.1016/0142-9612(90)90093-6

[7] Griffith L. G.: Polymeric biomaterials. Acta Materialia, **48**, 263–277 (2000).
DOI: 10.1016/S1359-6454(99)00299-2

[8] Lee C. H., Singla A., Lee Y.: Biomedical applications of collagen. International Journal of Pharmaceutics, **221**, 1–22 (2001).
DOI: 10.1016/S0378-5173(01)00691-3

[9] Yue Z., Liu X., Molino P. J., Wallace G. G.: Bio-functionalisation of polydimethylsiloxane with hyaluronic acid and hyaluronic acid – Collagen conjugate for neural interfacing. Biomaterials, **32**, 4714–4724 (2011).
DOI: 10.1016/j.biomaterials.2011.03.032

[10] Bisson I., Kosinski M., Ruault S., Gupta B., Hilborn J., Wurm F., Frey P.: Acrylic acid grafting and collagen immobilization on poly(ethylene terephthalate) surfaces for adherence and growth of human bladder smooth muscle cells. Biomaterials, **23**, 3149–3158 (2002).
DOI: 10.1016/S0142-9612(02)00061-3

[11] Cheng Z., Teoh S-H.: Surface modification of ultra thin poly (ε-caprolactone) films using acrylic acid and collagen. Biomaterials, **25**, 1991–2001 (2004).
DOI: 10.1016/j.biomaterials.2003.08.038

[12] Li Y-H., Huang Y-D.: The study of collagen immobilization on polyurethane by oxygen plasma treatment to enhance cell adhesion and growth. Surface and Coatings Technology, **201**, 5124–5127 (2007).
DOI: 10.1016/j.surfcoat.2006.07.128

[13] Ma L., Gao C., Mao Z., Zhou J., Shen J., Hu X., Han C.: Collagen/chitosan porous scaffolds with improved biostability for skin tissue engineering. Biomaterials, **24**, 4833–4841 (2003).
DOI: 10.1016/S0142-9612(03)00374-0

[14] Yan T., Sun R., Li C., Tan B., Mao X., Ao N.: Immobilization of type-I collagen and basic fibroblast growth factor (bFGF) onto poly (HEMA-co-MMA) hydrogel surface and its cytotoxicity study. Journal of Materials Science: Materials in Medicine, **21**, 2425–2433 (2010).
DOI: 10.1007/s10856-010-4094-5

[15] Hu S-G., Jou C-H., Yang M-C.: Biocompatibility and antibacterial activity of chitosan and collagen immobilized poly(3-hydroxybutyric acid-co-3-hydroxyvaleric acid). Carbohydrate Polymers, **58**, 173–179 (2004).
DOI: 10.1016/j.carbpol.2004.06.039

[16] Chirila T. V., Constable I. J., Crawford G. J., Vijayasekaran S., Thompson D. E., Chen Y-C., Fletcher W. A., Griffin B. J.: Poly(2-hydroxyethyl methacrylate) sponges as implant materials: *In vivo* and *in vitro* evaluation of cellular invasion. Biomaterials, **14**, 26–37 (1993).
DOI: 10.1016/0142-9612(93)90072-A

[17] Hoffman A. S.: Hydrogels for biomedical applications. Advanced Drug Delivery Reviews, **54**, 3–12 (2002).
DOI: 10.1016/S0169-409X(01)00239-3

[18] Hsiue G-H., Guu J-A., Cheng C-C.: Poly(2-hydroxyethyl methacrylate) film as a drug delivery system for pilocarpine. Biomaterials, **22**, 1763–1769 (2001).
DOI: 10.1016/S0142-9612(00)00336-7

[19] Rosiak J. M., Yoshii F.: Hydrogels and their medical applications. Nuclear Instruments and Methods in Physics Research Section B: Beam Interactions with Materials and Atoms, **151**, 56–64 (1999).
DOI: 10.1016/S0168-583X(99)00118-4

[20] Young C-D., Wu J-R., Tsou T-L.: Fabrication and characteristics of polyHEMA artificial skin with improved tensile properties. Journal of Membrane Science, **146**, 83–93 (1998).
DOI: 10.1016/S0376-7388(98)00097-0

[21] Chetoni P., Di Colo G., Grandi M., Morelli M., Saettone M. F., Darougar S.: Silicone rubber/hydrogel composite ophthalmic inserts: Preparation and preliminary in vitro/in vivo evaluation. European Journal of Pharmaceutics and Biopharmaceutics, **46**, 125–132 (1998).
DOI: 10.1016/S0939-6411(97)00168-9

[22] Hsiue G-H., Lee S-D., Wang C-C., Shiue M. H-I., Chang P. C-T.: ppHEMA-modified silicone rubber film towards improving rabbit corneal epithelial cell attachment and growth. Biomaterials, **14**, 591–597 (1993).
DOI: 10.1016/0142-9612(93)90177-4

[23] Khorasani M. T., Mirzadeh H., Sammes P. G.: Laser surface modification of polymers to improve biocompatibility: HEMA grafted PDMS, in vitro assay – III. Radiation Physics and Chemistry, **55**, 685–689 (1999).
DOI: 10.1016/S0969-806X(99)00212-1

[24] Lednický F., Janatová V., Lopour P., Vondráček P.: Silicone rubber-hydrogel composites as polymeric biomaterials III. An investigation of phase distribution by scanning electron microscopy. Biomaterials, **12**, 848–852 (1991).
DOI: 10.1016/0142-9612(91)90073-J

[25] Lopour P., Vondráček P., Janatová V., Šulc J., Vacik J.: Silicone rubber-hydrogel composites as polymeric biomaterials: II. Hydrophilicity and permeability to water-soluble low-molecular-weight compounds. Biomaterials, **11**, 397–402 (1990).
DOI: 10.1016/0142-9612(90)90094-7

[26] Okada T., Ikada Y.: Modification of silicone surface by graft polymerization of acrylamide with corona discharge. Die Makromolekulare Chemie, **192**, 1705–1713 (1991).
DOI: 10.1002/macp.1991.021920804

[27] Rezaei S. M., Mohd Ishak Z. A.: The biocompatibility and hydrophilicity evaluation of collagen grafted poly (dimethylsiloxane) and poly (2-hydroxyethylmethacrylate) blends. Polymer Testing, **30**, 69–75 (2011).
DOI: 10.1016/j.polymertesting.2010.07.013

[28] Abbasi F., Mirzadeh H., Katbab A-A.: Modification of polysiloxane polymers for biomedical applications: A review. Polymer International, **50**, 1279–1287 (2001). DOI: 10.1002/pi.783

[29] Fichet O., Vidal F., Laskar J., Teyssie D.: Polydimethylsiloxane–cellulose acetate butyrate interpenetrating polymer networks synthesis and kinetic study. Part I. Polymer, **46**, 37–47 (2005). DOI: 10.1016/j.polymer.2004.10.053

[30] Park S., Nam S. H., Koh W-G.: Preparation of collagen-immobilized poly(ethylene glycol)/poly(2-hydroxyethyl methacrylate) interpenetrating network hydrogels for potential application of artificial cornea. Journal of Applied Polymer Science, **123**, 637–645 (2011). DOI: 10.1002/app.34532

[31] Wang J., Li X.: Enhancing protein resistance of hydrogels based on poly(2-hydroxyethyl methacrylate) and poly(2-methacryloyloxyethyl phosphorylcholine) with interpenetrating network structure. Journal of Applied Polymer Science, **121**, 3347–3352 (2011). DOI: 10.1002/app.33960

[32] Sperling L. H.: Interpenetrating polymer networks: An overview. Advances in Chemistry, **239**, 3–38 (1994). DOI: 10.1021/ba-1994-0239.ch001

[33] Sperling L. H., Mishra V.: Metastable phase diagrams for simultaneous interpenetrating networks. Macromolecular Symposia, **118**, 363–370 (1997). DOI: 10.1002/masy.19971180147

eXPRESS Polymer Letters Vol.8, No.1 (2014) 50–54
Available online at www.expresspolymlett.com
DOI: 10.3144/expresspolymlett.2014.6

Synthesis and characterization of poly(ester amide) from renewable resources through melt polycondensation

Y. P. Ge[1], D. Yuan[1], Z. L. Luo[1], B. B. Wang[1,2*]

[1]School of Materials Science and Engineering, Changzhou University, 213164 Changzhou, China
[2]School of Materials Science and Engineering, North University of China, 030051 Taiyuan, China

Received 22 June 2013; accepted in revised form 2 September 2013

Abstract. Biodegradable poly(ester amide)s (PEAs) were synthesized from lactic acid and 11-aminoundecanoic acid via melt polycondensation. Molecular weights, chemical structures and thermal properties of the poly(ester amide)s were characterized in terms of gel permeation chromatography (GPC), Fourier transform infrared spectroscopy (FTIR), ^{1}H nuclear magnetic resonance (^{1}H NMR), differential scanning calorimetry (DSC) and thermogravimetric analysis (TGA), respectively. The PEAs have low molecular weights and display a lower cold crystallization temperature as well as smaller crystallinity by comparison with the pure poly(lactic acid) (PLA). The incorporation of the 11-aminoundecanoic acid into the PLA chain not only improved the thermal stability but changed the decomposition process.

Keywords: *thermal properties, poly(ester amide)s, polycondensation, characterization*

1. Introduction

The ecological challenges and the fluctuating petroleum prices have instigated the research and development on the materials from renewable resources to be the hot spot. Nylon 11 and poly(lactic acid) (PLA) have attracted great interest since they can be produced from renewable resources, that is, the beginning material for nylon 11 is castor oil [1, 2] and these for PLA can be starch, cane molasses and beet sugar [3, 4]. Poly(ester amide)s (PEAs) are a class of very promising materials combining the favorable properties of polyesters (biodegradability) and polyamides (good mechanical and thermal behavior) [5]. The rigidity due to the double-bond character of the amide group coupled with extensive hydrogen bonding influences the ordering of PEAs and consequently enhances the mechanical and thermal stability. As such, the synthesis of PEAs represents a good alternative to overcome the thermal and mechanical limitations of PLA. Liu *et al*. [6] had synthesized tough PEAs having short nylon 6 segments in the main chains through polycondensation and chain extension, the initial decomposition temperature of the chain-extended PEAs is over 339°C. Fonseca *et al*. [7] synthesized novel PEAs from glycine and L-lactic acid by interfacial polymerization, the method needs to be optimized to afford a higher molecular weight and a narrow molecular weight distribution. Pramanik *et al.* [8] reported the synthesis of castor oil modified biodegradable PEAs with higher thermal stability. PEA based on caprolactone and 11-aminoundecanoic acid has also been reported by Qian *et al.* [9]. The same group also synthesized biodegradable PEA based on lactic acid and aminoundecanoic acid and investigated *in vitro* degradation behaviors [10]. However, PEA with low melting temperatures (≤89°C) were obtained at 50 mol% lactic acid loading level or above, which might be attributed the lower molecular weights. In this work, a small quantity of rigid amide group was

---

[*] Corresponding author, e-mail: biaobingwang@hotmail.com

distributed into the PLA chains to improve the thermal stability of PLA through melt polycondensation using L-lactic acid (LA) and 11-aminoundecanoic acid as starting materials. The PEAs were characterized by GPC, FTIR, ^{1}H NMR, DSC and TGA.

2. Experimental

2.1. Materials

L-Lactic acid was supplied as a 90 wt% aqueous solution by Lingfeng Chemical Reagent (China). 11-aminoundecanoic acid was purchased from Zhonglian Zenong Chemical Co. (China). Tin(II) chloride dihydrate ($SnCl_2{\cdot}2H_2O$; 98%, reagent grade) and p-toluenesulfonic acid monohydrate (TSA; 98.5+%, ACS reagent grade) were purchased from Alfa Aesar Co. (America). Other chemical reagents were purchased from Yonghua Chemical (Jiangsu, China).

2.2. Dehydration/oligomerization

The lactic acid and 11-aminoundecanoic acid were added to a 250 mL three-neck flask and stirred with a magnetic stirrer and dehydrated at 110°C under atmospheric pressure for 2 h, then at 130°C under a reduced pressure of 13 300 Pa for 3 h, and finally at 150°C under a reduced pressure of 13 300 Pa for another 4 h. Then a viscous transparent oligomer was obtained, and became solid after cooling to room temperature. Oligomer of pure lactic acid was also synthesized as a control following the same procedures.

2.3. Polymerization

The previous flask was equipped with a mechanical stirrer and a reflux condenser that was connected with a vacuum system through a liquid nitrogen cold trap and then mixed with $SnCl_2{\cdot}2H_2O$ (0.4 wt% relative to oligomer) and TSA (an equimolar amout to $SnCl_2{\cdot}2H_2O$) as a binary catalyst. The mixture was gradually heated to 180°C with stirring, following which the pressure was reduced gradually to 1330 Pa in 1.5 h and the reaction was continued for another 10 h. The product was cooled and dissolved in chloroform and subsequently precipitated into anhydrous ethanol. The resulting solid was filtered and dried under vacuum at 80°C for 12 h. Bulk PEAs were labeled as PEA-2.5 and PEA-5 according to the weight ratio of 11-aminoundecanoic acid to lactic acid. Pure PLA was also synthesized following the same procedures and used as a control.

2.4. GPC analysis

The weight ($\overline{M}_\mathrm{w}$) and number-average molecular ($\overline{M}_\mathrm{n}$) weight as well as the polydispersity index (PDI, equal to $\overline{M}_\mathrm{w}/\overline{M}_\mathrm{n}$) were determined through GPC (Waters, America). The test was carried out with a Waters 1515 separations module, Waters 2414 refractive index detector. Samples were dissolved in tetrahydrofuran at a concentration of 5 mg/mL. The measurement was performed at room temperature and a flow rate of 1 mL/min. The molecular weight was calibrated according to a polystyrene standard.

2.5. FTIR spectroscopy

FTIR spectra were acquired with an Avatar 370 spectrometer (Thermo Nicolet, America). Spectra were collected in the region of 4000–370 cm^{-1} with a spectral resolution of 0.1 cm^{-1}.

2.6. NMR spectroscopy

^{1}H NMR spectra were acquired at room temperature for PLA and PEAs on an Advance III 400M NMR (Bruker, Rheinstetten, Germany) in $CDCl_3$ containing tetramethylsilane as the internal reference.

2.7. Thermogravimetric analysis (TGA)

Decomposition characteristics of the samples were determined with a TG 209 F3 (Netzsch Tarsus, Germany). About 5 mg of each sample was placed in the pan and heated from 50 to 650°C at a heating rate of 10°C/min under a nitrogen atmosphere.

3. Results and discussion

3.1. Molecular weights

Molecular weights of PLA and PEAs were measured using GPC, and the corresponding values are summarized in Table 1. As can be seen, the $\overline{M}_\mathrm{w}$ of the pure PLA is 25 566 g/mol. By comparison, the molecular weights of the PEAs are decreased with the incorporation of 11-aminoundecanoic acid since it is not easy to amidate under the reaction temperature (180°C). For example, the $\overline{M}_\mathrm{w}$ of the PEA-5 is 16 210 g/mol. The PDI values for the pure PLA and

Table 1. Molecular weights of PLA and PEAs

Sample	$\overline{M}_\mathrm{n}$	$\overline{M}_\mathrm{w}$	PDI ($\overline{M}_\mathrm{w}/\overline{M}_\mathrm{n}$)
PLA	16 230	25 566	1.58
PEA-2.5	11 889	18 932	1.59
PEA-5	11 109	16 213	1.46

PEAs range between 1.4 and 1.8, which are similar to those for PLA obtained from the melt polycondensation method [11, 12].

3.2. NMR

Figure 1 shows the typical ^{1}H NMR spectra of the pure PLA, PEA-2.5 oligomer and corresponding PEA-2.5. The major peaks at 1.58 and 5.17 ppm are assigned to the methyl and methine proton resonances from the PLA main chain. The weak peaks at 4.36 and at 1.28 ppm are assigned to the methine and methyl proton next to the terminal hydroxyl group, respectively. The above two weak peaks could be identified only for LA oligomers [13] since the intensity of these peaks decrease dramatically with the increasing molecular weights. As such, the above two peaks become obvious in the spectrum of PEA-2.5 oligomer. According to the assignment, the degree of polymerization of PEA-2.5 oligomer is estimated to be 8 from the integration ratio between the methane proton of peak b and peak c. The spectra of the PEA-2.5 oligomer and corresponding PEA-2.5 display three new weak peaks, which corresponds to the methane of 11-aminoundecanoic acid, at 3.22 ppm (peak f for PEA-2.5 oligomer) or 3.72 ppm (peak f for PEA-2.5), 2.32 ppm (peak g) and 1.25 ppm (peak e), respectively. It is indicating that the aminoundecanoic acid fragment is chemically introduced into the main chain of PLA.

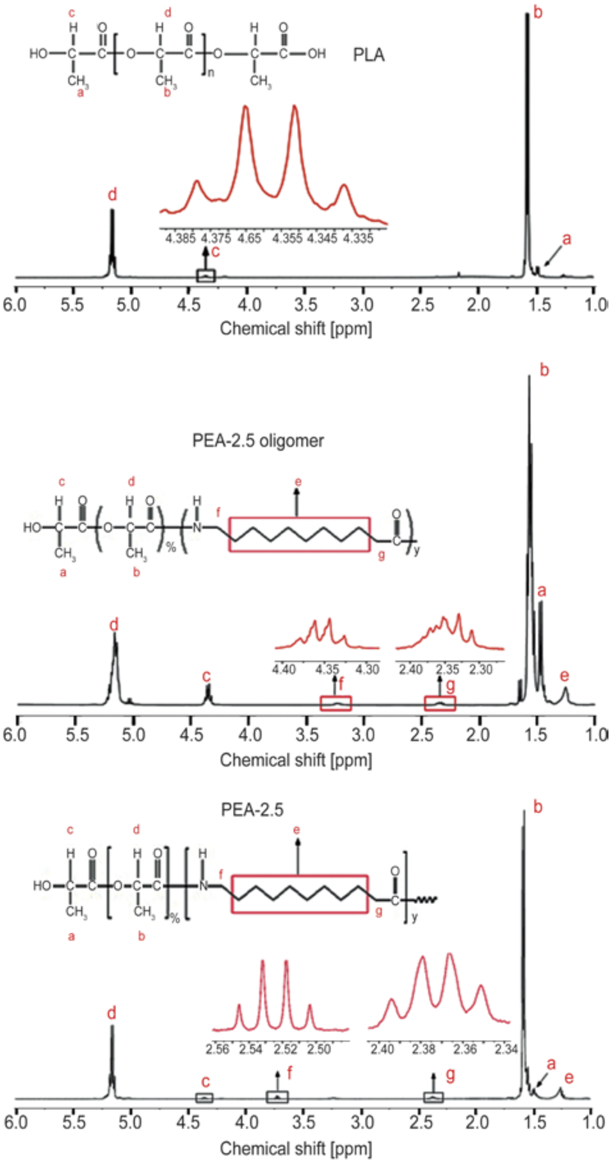

Figure 1. ^{1}H NMR spectra of PLA, PEA-2.5 oligomer and corresponding PEA-2.5

3.3. FTIR

The FTIR spectra of PLA and PEAs are illustrated in Figure 2. The pure PLA shows a strong absorption band at 1751 cm^{-1} corresponding to the stretching vibration of carbonyl groups (–C=O) from the repeated ester units. The –C–O– stretching vibrations from the ester units are observed at 1180, 1129, and 1082 cm^{-1}. The bands at 2996 and 2877 cm^{-1} are assigned to the –C–H asymmetric and symmetric stretching vibrations of CH$_3$ groups in the side chains, whereas their bending vibration appears at 1454 cm^{-1}. The band at 2948 cm^{-1} is attributed to the stretching of –CH– groups in the main chain of PLA, and its symmetric and asymmetric bending vibrations appear at 1382 and 1358 cm^{-1}. As compared with the pure PLA, the spectra of PEAs display the typical amide peaks at 3304 cm^{-1} (amide A), 3087 cm^{-1} (amide B), 1655 cm^{-1} (C=O stretching, amide I), and 1545 cm^{-1} (N–H bending, amide II). It is further demonstrating that 11-aminoundecanoic

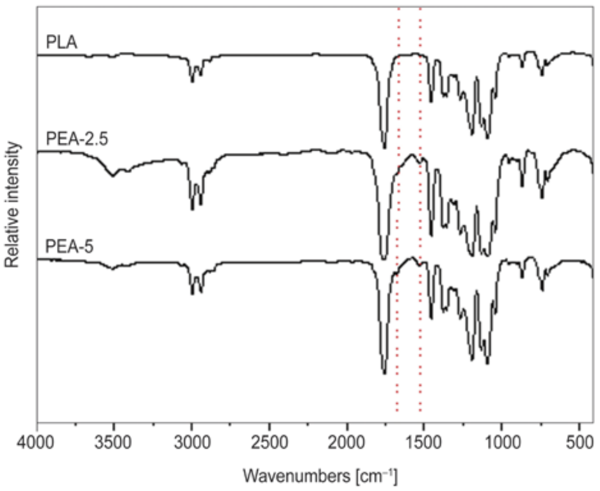

Figure 2. FTIR spectra of PLA and PEAs

acid fragment is chemically introduced into the main chain of PLA.

3.4. Thermal properties

The DSC thermograms (Figure 3) of all samples display glass transition, cold crystallization and melting behaviors, and the quantified results are summarized in Table 2. As can be seen, the glass transition temperature (T_g) of PEA-5 is about 6°C lower than that of the pure PLA because of its lower molecular weight [14]. The PEAs display a lower cold crystallization temperature but far smaller crystallinity than that of the pure PLA. It is attributed to the more readily chain mobility as the reduction of the molecular weights and the irregularity of the PLA chain with the incorporation of the 11-aminoundecanoic acid, respectively. Both PLA and PEAs exhibit double melting behavior, which can be explained by the melt-recrystallization model. The melting temperatures of the obtained PEAs are higher than that of PEAs reported in literature [10] at higher lactic acid contents.

The results of the thermogravimetric analysis of the pure PLA and PEAs are summarized in Table 3, while the weight loss and derivative weight loss curves are presented in Figures 4. The PLA shows a distinct one-stage degradation pattern and reaches its maximum rate at 255°C. The PEAs, however, display a two-stage degradation pattern. This implies that the degradation mechanism is altered by the incorporation of the 11-aminoundecanoic acid. For PEAs, the first and second weight loss processes belong to the breakage of the ester and amide bond [9], respectively. Moreover, it appears that the incorporation of the 11-amineundecanoic acid into the PLA chain improves the thermal stability. For example, the onset temperatures of PEA-2.5 and PEA-5 are increased by 32C and 38°C as compared to the pure PLA, respectively. The improvement of the thermal stability of PEAs can be attributed to the occurrence of the amide bond which has better thermal stability than ester bond and the intermolecular hydrogen bonding between ester and amide groups.

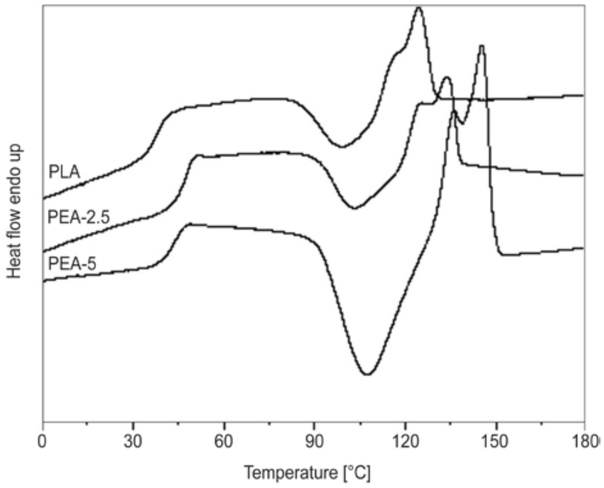

Figure 3. DSC thermograms of PLA and PEAs

Table 2. Thermal properties of PLA and PEAs determined from DSC thermograms

Sample	T_g [°C]	T_c [°C]	ΔH_c [J/g]	T_m [°C]	ΔH_m [J/g]	X_m [%]
PLA	43.5	107.2	36.9	145.4	30.0	32.1
PEA-2.5	46.8	102.7	9.8	133.9	10.6	11.3
PEA-5	37.7	99.7	10.5	124.6	9.6	10.3

Table 3. Thermal decomposition temperatures of PLA and PEAs

Sample	T_{onset} [°C]	T_{end} [°C]	T_{max} [°C]
PLA	214	278	255
PEA-2.5	246	378	276–335
PEA-5	252	480	289–340

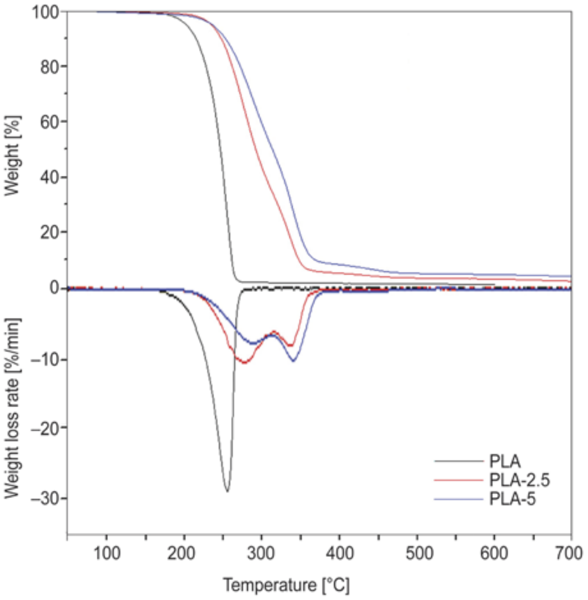

Figure 4. TGA and DTG curves of of PLA and PEAs

4. Conclusions

PEAs based on lactic acid and 11-aminoundecanoic acid was prepared by melt polycondensation. The lower cold crystallization temperatures and crystallinity of the PEAs were attributed to the reduced molecular weights and the irregularity of the PLA chain due to the incorporation of 11-aminoundecanoic acid. By contrast with the one-stage decomposition process of the pure PLA, the PEAs displayed two-stage decomposition process. Moreover, the thermal stability of the PEAs was higher than that of the pure PLA.

Acknowledgements

This work was financially funded by the Priority Academic Program Development of Jiangsu Higher Education Institution and Qing Lan project of Jiangsu.

References

[1] Wang B-B., Hu G-S., Zhao X., Gao F-Z.: Preparation and characterization of nylon 6 11 copolymer. Materials Letters, **21–22**, 2715–2717 (2006).
DOI: 10.1016/j.matlet.2006.01.076

[2] Wan J., Bu Z-Y., Li C., Fan H., Li B-G.: Preparation, melting, glass relaxation and nonisothermal crystallization kinetics of a novel dendritic nylon-11. Thermochimica Acta, **524**, 117–127 (2011).
DOI: 10.1016/j.tca.2011.07.002

[3] Ishimoto K., Arimoto M., Okuda T., Yamaguchi S., Aso Y., Ohara H., Kobayashi S., Ishii M., Morita K., Yamashita H., Yabuuchi N.: Biobased polymers: Synthesis of graft copolymers and comb polymers using lactic acid macromonomer and properties of the product polymers. Biomacromolecules, **13**, 3757–3768 (2012).
DOI: 10.1021/bm301212a

[4] Liao C-C., Wang C-C., Chen C-Y.: Stretching-induced crystallinity and orientation of polylactic acid nanofibers with improved mechanical properties using an electrically charged rotating viscoelastic jet. Polymer, **52**, 4303–4318 (2011).
DOI: 10.1016/j.polymer.2011.07.031

[5] Mallakpour S., Zadehnazari A.: Advances in synthetic optically active condensation polymers-A review. Express Polymer Letters, **5**, 142–181 (2011).
DOI: 10.3144/expresspolymlett.2011.15

[6] Liu S., Li C., Zhao J., Zhang Z., Yang W.: Synthesis and characterization of polyesteramides having short nylon-6 segments in the main chains through polycondensation and chain extension. Polymer, **52**, 6046–6055 (2011).
DOI: 10.1016/j.polymer.2011.10.048

[7] Fonseca A. C., Serra A. C., Coelho J. F. J., Gil M. H., Simões P. N.: Novel poly(ester amide)s from glycine and L-lactic acid by an easy and cost-effective synthesis. Polymer International, **62**, 736–743 (2013).
DOI: 10.1002/pi.4356

[8] Pramanik S., Sagar K., Konwar B. K., Karak N.: Synthesis, characterization and properties of a castor oil modified biodegradable poly(ester amide) resin. Progress in Organic Coatings, **75**, 569–578 (2012).
DOI: 10.1016/j.porgcoat.2012.05.009

[9] Qian Z., Li S., He Y., Li C., Liu X.: Synthesis and thermal degradation of biodegradable polyesteramide based on ε-caprolactone and 11-aminoundecanoic acid. Polymer Degradation and Stability, **81**, 279–286 (2003).
DOI: 10.1016/S0141-3910(03)00098-3

[10] Qian Z., Li S., Zhang H., Liu X.: Synthesis, characterization and in vitro degradation of biodegradable polyesteramide based on lactic acid. Colloid and Polymer Science, **281**, 869–875 (2003).
DOI: 10.1007/s00396-002-0846-1

[11] Moon S. I., Lee C. W., Miyamoto M., Kimura Y.: Melt polycondensation of L-lactic acid with Sn(II) catalysts activated by various proton acids: A direct manufacturing route to high molecular weight poly(L-lactic acid). Journal of Polymer Science Part A: Polymer Chemistry, **38**, 1673–1677 (2000).
DOI: 10.1002/(SICI)1099-0518(20000501)38:9<1673::aid-pola33>3.0.CO;2-T

[12] Moon S. I., Kimura Y.: Melt polycondensation of L-lactic acid to poly(L-lactic acid) with Sn(II) catalysts combined with various metal alkoxides. Polymer International, **52**, 299–305 (2003).
DOI: 10.1002/pi.960

[13] Espartero J. L., Rashkov I., Li S. M., Manolova N., Vert M.: NMR analysis of low molecular weight poly (lactic acid)s. Macromolecules, **29**, 3535–3539 (1996).
DOI: 10.1021/ma950529u

[14] Jamshidi K., Hyon S-H., Ikada Y.: Thermal characterization of polylactides. Polymer, **29**, 2229–2234 (1988).
DOI: 10.1016/0032-3861(88)90116-4

eXPRESS Polymer Letters Vol.8, No.1 (2014) 55–61
Available online at www.expresspolymlett.com
DOI: 10.3144/expresspolymlett.2014.7

Comparison of structural health assessment capabilities in epoxy – carbon black and epoxy – carbon nanotube nanocomposites

F. Inam[1*], *B.R. Bhat*[2], *N. Luhyna*[3], *T. Vo*[1]

[1]Northumbria University, Faculty of Engineering and Environment, Newcastle upon Tyne, NE1 8ST, United Kingdom
[2]National Institute of Technology Karnataka, Department of Chemistry, Catalysis and Materials Laboratory, Surathkal, Srinivasanagar-575025, India
[3]Advanced Composite Training and Development Centre (Airbus) and Glyndŵr University, Hawarden and Wrexham, CH5 3US and LL11 2AW, United Kingdom

Received 10 July 2013; accepted in revised form 9 September 2013

Abstract. A novel method for comparing structural health of different types of brittle epoxy nanocomposites filled with carbon nanostructured fillers is presented. Epoxy – 0.2 vol% carbon black (CB) and epoxy – 0.2 vol% carbon nanotube (CNT) nanocomposite bars were prepared by calendering and thermal curing. Nanocomposite bars were subjected to Vickers diamond indentation to produce sub-surface damage. Electrical conductivities were analysed by 4-point method to estimate the structural damage caused by indentation. For comprehensive comparison, fracture toughness and percolation threshold were analysed as well. Because of the systematically induced indentation damage, a sharp decrease of 89% was observed in the electrical conductivity of epoxy – CNT nanocomposite as compared to 25% in the electrical conductivity of epoxy – CB nanocomposite. CNTs impart superior damage sensing capability in brittle nanocomposite structures, in comparison to CB, due to their high aspect ratio (fibrous nature) and high electrical conductivity.

Keywords: *nanocomposites, carbon nanotubes, epoxy, material testing, smart polymers*

1. Introduction

Carbon nanotubes (CNTs), discovered accidentally in 1991 [1], have been widely investigated for their addition in polymer [2–5], ceramic [6] and metal [7] matrices to prepare nanocomposites owing to the combination of the superlative mechanical, thermal, and electronic properties attributed to them. CNT-filled polymer matrix composite materials are subject of significant research for their utilisation in an increasing number of industrial applications including energy, transportation, defence, automotive, aerospace, sporting goods, and infrastructure sectors [8]. Particularly among brittle epoxy materials, CNTs have been reported to significantly improve mechanical, thermal and electrical properties of the epoxy nanocomposites [9]. Apart from these improvements, CNTs also offer structural damage sensing ability to epoxy and the subject has been widely investigated [10–16] too. Structural health monitoring (SHM) is a type of a Non-destructive Evaluation (NDE) technique that essentially involves the strategic embedding of conductive filler into a structure to allow continuous and remote monitoring for damage, deformation and failure. SHM technology is applied increasingly for research and industrial purposes as a potential tool for quality assurance [17, 18]. However, many of the developed and available NDE technologies are complex, expensive and require signif-

---

[*]Corresponding author, e-mail: fawad.inam@northumbria.ac.uk

icant calibration with the passage of time. Nanostructured carbon embedded systems have proven to be more sensitive towards structural damage [10–16]. Most of the previous researched methods incorporating CNTs were based on the sensing of damage of long-fibre or woven reinforced epoxy [10–16] or for other brittle matrices like cement for civil structures [19]. Such studies aimed to induce damage systematically to the nanocomposite sample using tensile [10, 11] and bending [11, 12] modes. Anand and Mahapatra [13] dispersed carbon black (CB) and CNTs in epoxy thins and conducted a quasi-static and dynamic strain sensing study. However, there was no characterisation of damage in that report. Thostenson and Chou [14] studied *in situ* sensing to detect localized damage in CNT-filled glass fiber composites but no comparison was made with CB-filled system. Recently, Nagashpour and Hoa [15] investigated *in situ* monitoring of through-thickness strain in glass fiber/epoxy composite laminates using carbon nanotube sensors. Kostopoulos *et al*. [16] reported improved structural health monitoring capability in CNT-filled carbon fibre-reinforced epoxy system as compared to carbon fibre-reinforced epoxy. However, no comparisons were made for CB-filled systems in these studies.

A novel method of assessing structural damage in epoxy by analysing change in the electrical conductivity of epoxy-CNT nanocomposite is presented in this letter. A comparison between the sensitivity of CNT based nanocomposites with carbon black based nanocomposites has been made.

2. Experimental

The epoxy matrix used in this study consists of a modified DGEBA-based epoxy resin (GY250, a diglycidyl ether of bisphenol A) with a piperidine hardener, supplied by Ciba-Geigy, India. Carbon black powder (<50 nm, grade 633100, >99% pure) was supplied by Sigma Aldrich, UK. As per supplier, carbon black powder was produced by laser technique. Helium pycnometry (AccuPyc II 1340, micrometrics, UK) was used to evaluate densities of CNTs and CB for the calculation of filler volume fraction. Density of CB powder was found to be ~1 g/cm^3. The multiwall CNTs (grade: Elicarb) used in this study were kindly supplied by Thomas Swan, UK. They were synthesised by the Chemical Vapour Deposition (CVD) method and have an entangled cotton-like form. The CNTs have density of ~1.1 g/cm^3, an average outer diameter of 15 nm and lengths of up to 50 microns. CNT dimensions were measured as per technique mentioned elsewhere [20]. For reducing the non-carbonaceous content in CNT powder, an acid treatment was performed using a mixture of nitric (HNO_3, 90%) and sulfuric (H_2SO_4, 90%) acids. Acids were supplied by Sigma-Aldrich, UK. Distilled water (~20 vol%) was used to dilute the acids. In order to produce pure CNTs, the as-received CNTs (400 mg) were mixed with 200 mL acidic solution. Both acids were equally mixed in the solution. The acid–CNT mixture was homogenised by stirring with a glass rod on heating plate (~85°C) for 30 min and then bath ultrasonicated for 2 h. The resulting CNT dispersion was thoroughly washed with distilled water until the filtrate was colourless and neutral (pH ~7) after filtration. A Whatman filter paper of 1 µm was used. The purified CNTs were then dried for 48 h at 100°C in an oven. With the aid of Thermogravimetric analysis (TGA) technique, the amount of carbonaceous content in CNT powder was measured by recording the dry mass of remnant after complete oxidation of carbonaceous content. TGA was performed using TA Instruments (UK) SDT Q600 thermo gravimetric analyser. All specimens were examined on platinum pans in the range 30–650°C. A heating rate of 5°C/minute in flowing air (at 180 mL/minute) was used. Powder sample masses ranged from 30–40 mg. CNTs were purified to >99% (i.e. carbonaceous content) by acid treatment. Average length of CNT was found to be ~40 microns. No change in diameter was observed after acid treatment.

For producing epoxy – 0.2 vol% CNT nanocomposites, a batch of CNTs were aggressively mixed by high-speed mixing (RPM: ~2400, Silverson L5 Series, UK,) with the epoxy resin (without hardener) for 10 mins. This suspension was then added batch-wise to a mini-calender (Exakt, Germany) for final high shear mixing. The gap size between the alumina rolls of the mini-calender was 3 µm and the speed was set to 250 (1st roll), 70 (2nd roll) and 165 rpm (3rd roll). The dwell time of each batch of suspension was ~3 min. The suspension was collected, mixed with the hardener for 15 min by high-speed mixing (RPM: ~2000) for 5 mins. The suspension was poured in an open teflon mould (5 samples) and then cured for 16 h at 120°C. The same procedure was used for producing 5 bars of epoxy – 0.2 vol% CB nanocomposites and a bar of monolithic epoxy for comparison.

All samples were produced on the same day and were placed in a desiccator. After 15 hours they were removed from desiccator and all sample surfaces were cleaned by gentle wiping using a lint-free cloth soaked with isopropanol. After silver coating (Figure 1), they were then immediately indented and electrical conductivities were measured (at least 5 observations were made). The Vickers indentations were performed using a Zwick microhardness tester (500 g load with 10 seconds of indentation time). HVµ micro Vickers hardness tester was supplied by Zwick (UK). Five indents (equally spaced) were produced on each bar and the bulk electrical conductivity of nanocomposites was measured at room temperature based on the four-probe method (Figure 1) using specimens of dimensions 64×13×3 mm on a resistivity/Hall measurement system (Sony Tektronix 370 A, Japan). For this work, sharp diamond indenter was used and Vickers hardness was calculated by 1.854(F/D2), where F and D2 are applied force and area of indentation respectively. Fracture toughness of neat and nanofilled epoxy was determined from static three-point tests of the single edge notch specimens. Each of these specimens was cycled 100 times between 4 and 40% of the peak load at 1 Hz and then statically tested. During the static tests, the change in specimen length was measured by recording the ram positions through the displacement transducer of the universal tensile testing machine (Acumen eletrodynamic test system, MTS, USA). At least 5 samples (dimension: 64×13×3 mm) were tested for evaluating fracture toughness. The critical stress intensity factor (K_{IC}) was calculated according to the Equations (1) and (2) [21]:

$$K_{\mathrm{IC}} = \left(\frac{P}{B}w^{3/2}\right)f(a/w) \tag{1}$$

where P applied load on the specimen, B specimen thickness, w specimen width, a crack length, and

$$f(a/w) = \frac{\sqrt[3]{\frac{a}{w}}\left[1.99 - \left(\frac{a}{w}\right)\left(1 - \frac{a}{w}\right)\left(2.15 + 3.93\frac{a}{w} + 2.7\frac{a^2}{w^2}\right)\right]}{2\left(1 + 2\frac{a}{w}\right)\left(1 - \frac{a}{w}\right)} \tag{2}$$

Fractured surfaces were gold coated after indentation and observed in an FE-SEM (FEI, Inspect F, 20 kV, USA). For measuring the percolation threshold, circular discs of about 0.8 mm thickness were cut and the cross-sectional areas were coated with conductive silver paint. Prior to silver coating, all sample surfaces were cleaned by gentle wiping using a lint-free cloth soaked with isopropanol. The diameters of circles with equivalent area to the cross-section were much greater than the distance between them. 2-probe AC impedance spectroscopy was performed using a Solartron 1260 Impedance/gain phase analyser with a voltage amplitude of 1 V. The frequency range was set from 1 to 107 Hz. All electrical conductivities were measured at 42% humidity.

3. Results and discussion

Structural health assessing for nanostructured carbon-filled epoxy composites was verified by measuring the change in electrical resistivity after systematic introduction of damage to the samples. The experimental setup shown in Figure 1 was especially designed for the evaluation of the change in electrical conductivity during the incremental damage. It should be noted that the connecting wires in the experimental setup (Figure 1) were permanently bonded by using silver paste in order to avoid any contact resistance for this comparative analysis. Following Vickers indentation, clear damage was visible to the unaided eye for all specimens.

During Vickers indentation, brittle materials usually fracture under the surface or sub-surface (Hertzian cone crack) and from the tips of the diagonal indent to accommodate the penetrating diamond indenter [22]. As a result of that, new surfaces are created and radial-median and lateral crack systems are produced during loading and unloading of Vickers indenter (Figure 2). Electronic microscopy revealed radial cracking from the tip of the indent (Figure 3). All samples (epoxy, epoxy – 0.2 vol% CB and epoxy – 0.2 vol% CNT nanocomposites) retained their integrity because of the small Vickers loadings after indenta-

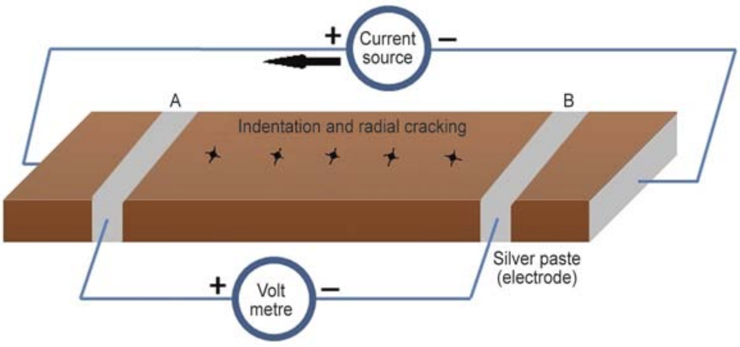

Figure 1. Four-probe electrical conductivity measurement schematics of indented sample. Distance between A and B is 56 mm

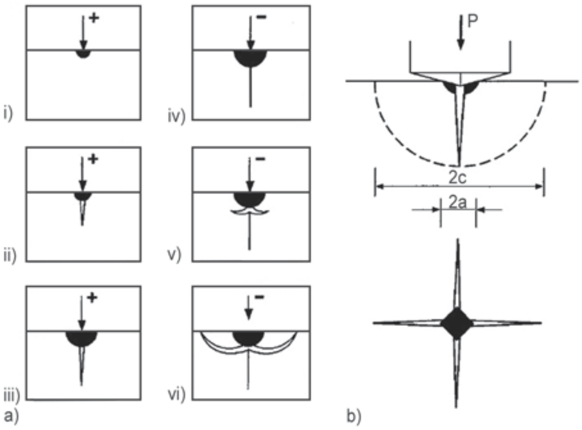

Figure 2. Radial-median and lateral crack system: a) evolution during complete loading (+) and unloading (–) cycle. Dark region denotes irreversible deformation zone; and b) geometrical parameters of radial system [22].

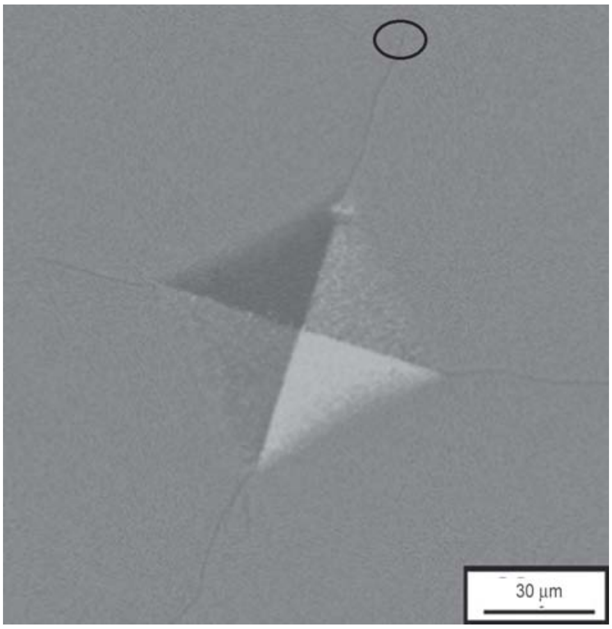

Figure 3. Vickers indent on epoxy – 0.2 vol% CB nanocomposite showing radial cracking. Tip of the crack (encircled) is analysed in Figure 4.

tion. The load (500 g) was carefully selected to cause appropriate sub-surface damage for analysing electrical conductivities without completely fracturing the sample bars.

As compared to epoxy, with a Vickers hardness of 0.16±0.02 GPa, slight decreases in hardness were observed for epoxy – 0.2 vol% CB and epoxy – 0.2 vol% CNT nanocomposite samples (i.e. 0.12±0.03 and 0.11±0.03 GPa respectively). This is primarily due to the lubricant nature of carbon nanofillers which is responsible for deeper penetration on the Vickers indenter during the indentation. These observations for nanocomposites and measured values of hardness for epoxy are in consistent with study conducted by Low and Shi [23] and Lau *et al*. [2] respectively. Due to fibrous nature of CNTs, crack bridging was observed (Figure 4) which is also responsible for improving fracture toughness of epoxy nanocomposites [24]. Such phenomenon was not observed for particulate (carbon black) filled epoxy nanocomposites where isolated CB particles were observed on the edges of the fractured surfaces (Figure 4). This observation is also consistent with previous research work comparing mechanical properties of CNT and CB-filled epoxy nanocomposites [3].

In order to efficiently exploit the full potential of CNTs for improving the sensing capability in polymers, it is important to have good dispersion of CNT in the polymeric matrix. The extraordinary large specific surface area of CNTs is the main hurdle for homogeneous dispersion and de-bundling of CNTs. Calendering epoxy-nanofiller dispersions has proved to be the one of the best available solution for producing homogeneous epoxy-nano filler dispersions [3]. Individual CB particles, pointed by white arrows, and CNT fibres can be seen in Figure 4a and 4b respectively. Particularly for epoxy – 0.2 vol% CNT nanocomposites, this level of dispersion is critical

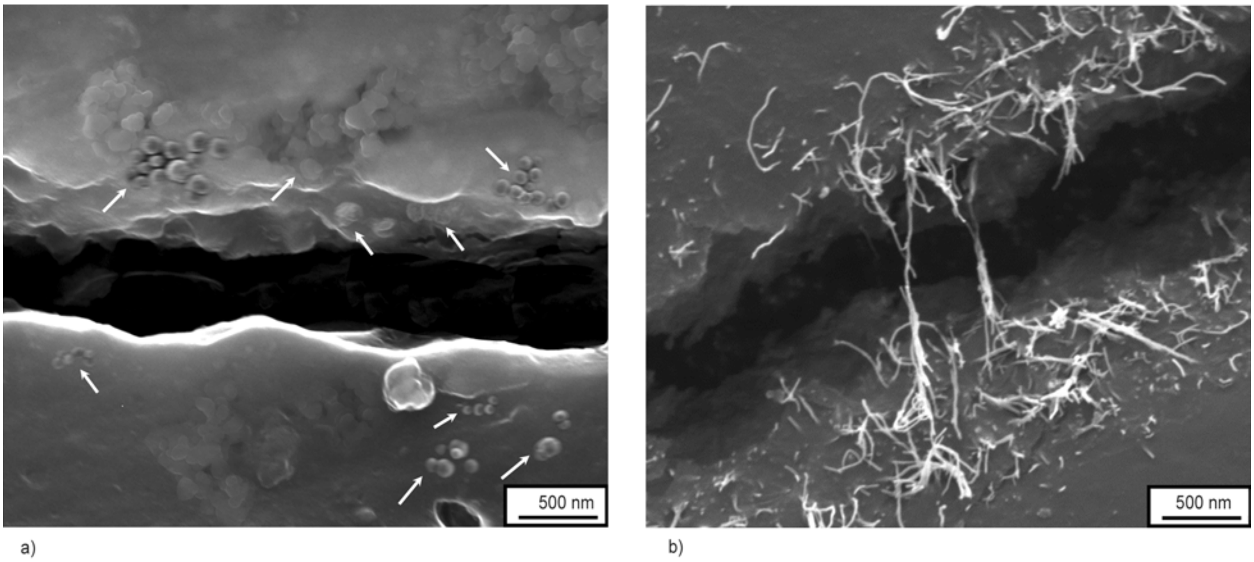

Figure 4. Damaged caused by Vickers indentation in: a) epoxy – 0.2 vol% CB nanocomposite; and b) epoxy – 0.2 vol% CNT nanocomposite

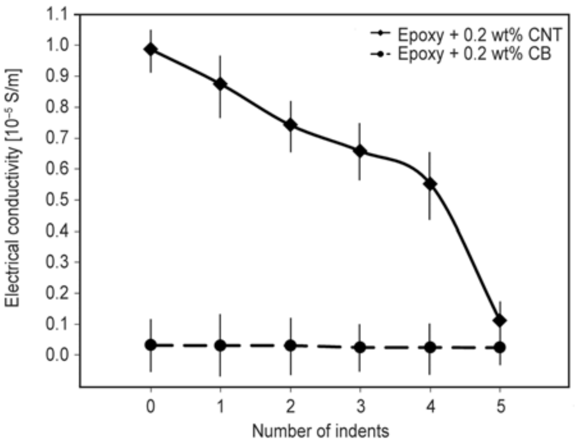

Figure 5. Change in electrical conductivity due to Vickers indentation in epoxy – carbon nanocomposites

for its improved damage sensing capability. It can be understood that if CNTs are not homogeneously distributed and there is no separation of CNTs taking place during the fracturing, such high sensitivity (Figure 5) cannot be achieved.

It is necessary to discuss the fracture, hardness and location of carbon nanofillers to understand the induced structural health assessing capability, which can be observed from Figure 5. The change in electrical conductivities of epoxy – 0.2 vol% CB and epoxy – 0.2 vol% CNT nanocomposite samples as a result of the deliberate damage (i.e. Vickers indentation) is shown in Figure 5. Electrical conductivity was measured after every indentation for all 5 samples of both types of nanocomposites. Error bars, shown in Figure 5, represent good repeatability of measured values. It is obvious from Figure 5 that CNT-filled epoxy nanocomposites were more sensitive towards the indentation damage as compared to CB-filled epoxy nanocomposites. After 5 indentations, the average electrical conductivity for CNT nanocomposites decreased from $0.987\cdot10^{-5}$ to $0.111\cdot10^{-5}$ S/m (i.e. a decrease of 89%). For CB nanocomposites, the average electrical conductivity decreased from $0.032\cdot10^{-5}$ to $0.024\cdot10^{-5}$ S/m (i.e. a decrease of 25%). This is due to the fibrous nature of CNTs as opposed to particulate form of CB (Figure 4). The different behaviour of the carbon nanotube modified matrix system and the carbon black modified matrix system has to be attributed to the intrinsic structure of the percolated conductive paths in the composite. In this context, the high axial electrical conductivity CNT not only offers the potential for fabricating conducting polymers but also responsive polymeric systems.

For correlating change in electrical conductivity and indentation damage, fracture toughness of samples was compared (Figure 6). It was found that CNT nanocomposites have 14% higher fracture toughness as compared to CB nanocomposites. This means that upon indentation, more damage was done by the penetrating diamond indenter for CB nanocomposites as compared to CNT nanocomposites. However, very small change in electrical conductivity was observed for CB nanocomposites. For CNT nanocomposites, CNTs are responsible for improving fracture toughness of epoxy matrix, which is also consistent with the literature [3, 9]. As compared to CB nanocomposites, less damage was produced in

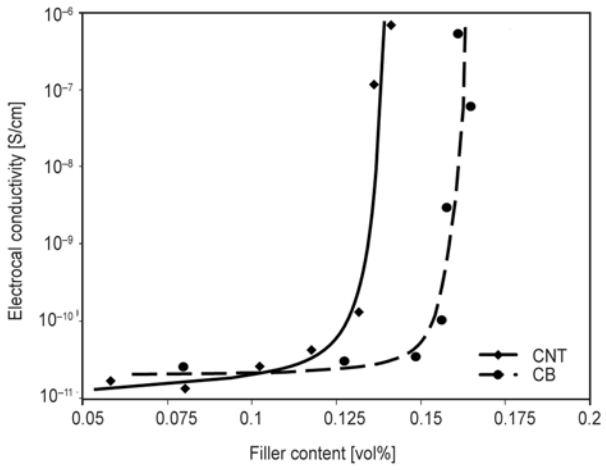

Figure 6. Epoxy nanocomposite conductivity as a function of carbon nanofiller volume fraction

CNT nanocomposites but a sharp decrease in electrical conductivity was observed. This means that CNTs nanocomposite have superior damage sensing capability as compared to CB nanocomposites, which is due to the fibrous nature and high surface area of CNTs.

Both carbon fillers used in this study have different geometrical shapes (i.e. CNTs are cylindrical, whereas CB consists of spherical particles). For the sake of real and comprehensive comparison, it is necessary to evaluate the percolation threshold for epoxy nanocomposites. Percolation thresholds for epoxy – carbon nanocomposites were measured (Figure 7). A percolation threshold of 0.0129 and 0.158 vol% was found for epoxy – CNT and epoxy – CB nanocomposites respectively. Therefore, it is confirmed that by using 0.2 vol% of filler content for comparing structural health assessing capabilities, the authors are making sure that the filler content is more than the percolation threshold which is important for this work. These percolation threshold and electrical conductivity values for epoxy nanocomposites are consistent with the previously reported values as reviewed by Bauhofer and Kovacs [25].

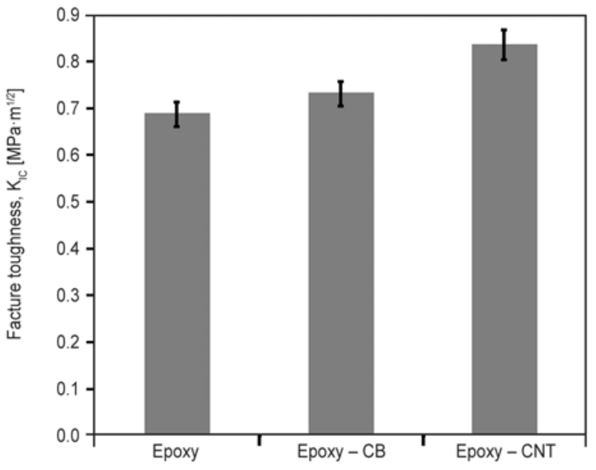

Figure 7. Fracture toughness of neat epoxy and epoxy nanocomposites

4. Conclusions

The results of the experiments presented here demonstrate the high potential of CNTs to be used for damage sensing in brittle materials like epoxy and glasses. CNTs were used to sense sub-surface damage in cured epoxy. All nanocomposite compositions used in this study had filler content higher than the percolation threshold for electrical conductivity. As compared to CB, CNTs possess better damage sensing ability in brittle nanocomposite structures due to their high aspect ratio (fibrous nature) and electrical conductivity. It was found that CNT nanocomposites have 14% higher fracture toughness as compared to CB nanocomposites. A sharp decrease of 89% was observed in the electrical conductivity of epoxy – CNT nanocomposite as compared to 25% in the electrical conductivity of epoxy – CB nanocomposite due to indentation damage. Therefore, it is concluded that as compared to CB, CNT offer higher sensitivity for structural health assessing to diagnose a structural safety and to prevent a catastrophic failure in brittle materials. There are many challenges for practical implementation of proposed novel NDE technique for a real structural unit and it would be the subject of the future research. This technique can also be used for damage sensing in ceramics matrices, which is subject of future research.

Acknowledgements

Dr. Fawad Inam would like to acknowledge generous support from Airbus UK, Cytec Engineered Materials Ltd. and Thomas Swan for supplying materials and their valuable time.

References

[1] Iijima S.: Helical microtubules of graphitic carbon. Nature, **354**, 56–58 (1991).
DOI: 10.1038/354056a0

[2] Lau K-T., Shi S-Q., Zhou L-M., Cheng H-M.: Microhardness and flexural properties of randomly-oriented carbon nanotube composites. Journal of Composite Materials, **37**, 365–376 (2003).
DOI: 10.1177/0021998303037004043

[3] Gojny F. H., Wichmann M. H. G., Köpke U., Fiedler B., Schulte K.: Carbon nanotube-reinforced epoxy-composites: Enhanced stiffness and fracture toughness at low nanotube content. Composites Science and Technology, **64**, 2363–2371 (2004).
DOI: 10.1016/j.compscitech.2004.04.002

[4] Inam F., Peijs T.: Transmission light microscopy of carbon nanotubes-epoxy nanocomposites involving different dispersion methods. Advanced Composites Letters, **15**, 7–13 (2006).

[5] Prashantha K., Soulestin J., Lacrampe M. F., Krawczak P.: Present status and key challenges of carbon nanotubes reinforced polyolefins: A review on nanocomposites manufacturing and performance issues. Polymers and Polymer Composites, **17**, 205–245 (2009).

[6] Cho J. C., Inam F., Reece M. J., Chlup Z., Dlouhy I., Shaffer M. S. P., Boccaccini A. R.: Carbon nanotubes: Do they toughen brittle matrices? Journal of Materials Science, **46**, 4770–4779 (2011).
DOI: 10.1007/s10853-011-5387-x

[7] Bakshi S. R., Lahiri D., Agarwal A.: Carbon nanotube reinforced metal matrix composites – A review. International Materials Reviews, **55**, 41–64 (2010).
DOI: 10.1179/095066009X12572530170543

[8] De Volder M. F. L., Tawfick S. H., Baughman R. H., Hart A. J.: Carbon nanotubes: Present and future commercial applications. Science, **339**, 535–539 (2013).
DOI: 10.1126/science.1222453

[9] Zhou Y. X., Wu P. X., Cheng Z-Y., Ingram J., Jeelani S.: Improvement in electrical, thermal and mechanical properties of epoxy by filling carbon nanotube. Express Polymer Letters, **2**, 40–48 (2008).
DOI: 10.3144/expresspolymlett.2008.6

[10] Lee S-I., Yoon D-J.: Structural health monitoring for carbon fiber/carbon nanotube (CNT)/epoxy composite sensor. Key Engineering Materials, **321–323**, 290–293 (2006).
DOI: 10.4028/www.scientific.net/KEM.321-323.290

[11] Böger L., Wichmann M. H. G., Meyer L. O., Schulte K.: Load and health monitoring in glass fibre reinforced composites with an electrically conductive nanocomposite epoxy matrix. Composites Science and Technology, **68**, 1886–1894 (2008).
DOI: 10.1016/j.compscitech.2008.01.001

[12] Alexopoulos N. D., Bartholome C., Poulin P., Marioli-Riga Z.: Structural health monitoring of glass fiber reinforced composites using embedded carbon nanotube (CNT) fibers. Composites Science and Technology, **70**, 260–271 (2010).
DOI: 10.1016/j.compscitech.2009.10.017

[13] Anand S. V., Mahapatra D. R.: Quasi-static and dynamic strain sensing using carbon nanotube/epoxy nanocomposite thin films. Smart Materials and Structures, **18**, 045013/1–045013/13 (2009).
DOI: 10.1088/0964-1726/18/4/045013

[14] Thostenson E. T., Chou T-W.: Carbon nanotube-based health monitoring of mechanically fastened composite joints. Composites Science and Technology, **68**, 1886–1894 (2008).
DOI: 10.1016/j.compscitech.2008.05.016

[15] Naghashpour A., Hoa S. V.: *In situ* monitoring of through-thickness strain in glass fiber/epoxy composite laminates using carbon nanotube sensors. Composites Science and Technology, **78**, 41–47 (2013).
DOI: 10.1016/j.compscitech.2013.01.017

[16] Kostopoulos V., Vavouliotis A., Karapappas P., Tsotra P., Paipetis A.: Damage monitoring of carbon fiber reinforced laminates using resistance measurements. Improving sensitivity using carbon nanotube doped epoxy matrix system. Journal of Intelligent Material Systems and Structures, **20**, 1025–1034 (2009).
DOI: 10.1177/1045389X08099993

[17] Montalvão D., Maia N. M. M., Ribeiro A. M. R.: A review of vibration-based structural health monitoring with special emphasis on composite materials. The Shock and Vibration Digest, **38**, 295–324 (2006).
DOI: 10.1177/0583102406065898

[18] Ciang C. C., Lee J-R., Bang H-J.: Structural health monitoring for a wind turbine system: A review of damage detection methods. Nanotechnology, **22**, 045017/1–045017/5 (2013).
DOI: 10.1088/0957-0233/19/12/122001

[19] Yu X., Kwon E.: A carbon nanotube/cement composite with piezoresistive properties. Smart Materials and Structures, **18**, 055010/1–055010/5 (2009).
DOI: 10.1088/0964-1726/18/5/055010

[20] Inam F., Vo T., Jones J. P., Lee X.: Effect of carbon nanotube lengths on the mechanical properties of epoxy resin: An experimental study. Journal of Composite Materials, **47**, 2321–2330 (2013).
DOI: 10.1177/0021998312457198

[21] ASTM D5045-99(2007)e1: Standard test methods for plane-strain fracture toughness and strain energy release rate of plastic materials (2007).

[22] Lawn B.: Facture of brittle solids. Cambridge University Press (1993).

[23] Low I. M., Shi C.: Vickers indentation responses of epoxy polymers. Journal of Materials Science Letters, **19**, 1181–1183 (1998).
DOI: 10.1023/A:1006517005082

[24] Hollertz R., Chatterjee S., Gutmann H., Geiger T., Nüesch F. A., Chu B. T. T.: Improvement of toughness and electrical properties of epoxy composites with carbon nanotubes prepared by industrially relevant processes. Nanotechnology, **22**, 125702/1–125702/9 (2011).
DOI: 10.1088/0957-4484/22/12/125702

[25] Bauhofer W., Kovacs J. Z.: A review and analysis of electrical percolation in carbon nanotube polymer composites. Composites Science and Technology, **69**, 1486–1498 (2009).
DOI: 10.1016/j.compscitech.2008.06.018

eXPRESS Polymer Letters Vol.8, No.1 (2014) 62–72
Available online at www.expresspolymlett.com
DOI: 10.3144/expresspolymlett.2014.8

The effect of needleless electrospun nanofibrous interleaves on mechanical properties of carbon fabrics/epoxy laminates

K. Molnár[1,2*], *E. Košťáková*[3], *L. Mészáros*[1]

[1]Department of Polymer Engineering, Faculty of Mechanical Engineering, Budapest University of Technology and Economics, Műegyetem rkp. 3., H-1111, Budapest, Hungary
[2]MTA–BME Research Group for Composite Science and Technology, Műegyetem rkp. 3., H-1111, Budapest, Hungary
[3]Department of Nonwovens, Faculty of Textile Engineering, Technical University of Liberec, Hálkova 6, 461 17 Liberec Czech Republic

Received 3 June 2013; accepted in revised form 11 September 2013

Abstract. The effect of polyacrylonitrile nanofibrous interlaminar layers on the impact properties of unidirectional and woven carbon fabric (CF)-reinforced epoxy (EP) matrix composites was investigated. The nanofibers were produced directly on the surface of carbon fabrics by a needleless electrospinning method, and composites were then prepared by vacuum-assisted impregnation. Interlaminar shear stress tests, three-point bending, Charpy-impact and instrumented falling weight tests were carried out. The fracture surfaces were analyzed by scanning electron microscopy. Due to the nano-sized reinforcements, the interlaminar shear strength of the woven and unidirectional fiber-reinforced composites was enhanced by 7 and 11%, respectively. In the case of the falling weight impact tests carried out on woven reinforced composites, the nanofibers increased the absorbed energy to maximum force by 64% compared to that measured for the neat composite. The Charpy impact tests indicated that the nanofiber interleaves also led to a significant increase in the initiation and total break energies. Based on the results, it can be concluded that the presence of nanofibers can effectively increase the impact properties of composites without compromising their in-plane properties because the thickness of the composites was not altered by the presence of interleaves. The improvement of the impact properties can be explained by the good load distribution behavior of the nanofibers.

Keywords: *polymer composites, needleless electrospinning, carbon fiber, nanofiber, delamination*

1. Introduction

The relatively easy production of polymer nanofibers by electrospinning has been the subject of many application-oriented investigations over the past few years. Most of these studies address the possibility of using such nanofibers in filtering, biomedical, sensor and clothing applications [1–4]. Because of their high surface-area-to-volume ratio, the nanofibrous materials could also be efficient reinforcing materials in polymer matrix composites. In these systems, the nanofibers can even act as the primary reinforcement (the nanofibers are the only reinforcing materials) as well as co-reinforcement (in addition to microfibers) [5]. From a mechanical properties point of view, the main problem associated with common fiber-reinforced polymer composite laminates is their weak interlaminar properties. Due to a geometry that is not absolutely planar, much free space occurs between layers of the reinforcing structures, which are filled up by the matrix material during impregnation. Thus, between the layers, the properties are determined mainly by the matrix and voids. The loads induced by shear- or out-of-plane stresses must be borne by this relatively weak matrix,

---

[*]Corresponding author, e-mail: molnar@pt.bme.hu

and therefore, damage such as delamination, buckling and peeling can occur [6, 7]. It should also be noted that the physical properties of the matrix can also be affected by the change in several environmental factors such as temperature or humidity [8] that can result in the further decrement of interlaminar properties.

There are several technologies that have been developed to enhance the interlaminar shear strength of polymer composites, such as physical blending, the placement of special thin films [9–11] and the incorporation of carbon nanotubes (CNTs), alumina or silica particles between laminate layers [12–14]. However, these techniques often modify the geometry and increase the weight of laminates. In such cases, improving the interlaminar properties can lead to a decrease of in-plane properties. Stitching [15], z-fiber pinning and other methods [16] can be applied to clench the layers, but these procedures can cause fiber breaks in the primary reinforcement that can also lead to a decrease in in-plane properties and generate additional production costs.

Using nanofibrous layers can be a feasible way to enhance interlaminar properties without compromising other mechanical properties. Nanofibers can be applied in small amounts, and because they are very flexible, they can take the shape of the microfibrous reinforcement that is applied, locally exerting their effects in matrix-rich areas. Furthermore, because nanofibrous layers are porous, they can be easily soaked in resin; therefore, they do not affect the geometry or the fiber content of composites significantly. The main benefit of using nanofibers in conventional composites is that the load transfer between the strengthening layers becomes more efficient, thus making the matrix between the layers tougher [17].

Interlaminar toughening using small-diameter fibers was first applied at the beginning of 2000s by Dzenis and Reneker [18], who produced graphite/epoxy unidirectional pre-pregs with poly(benzimidazole) electrospun fibers. The authors measured 15 and 130% improvements in the Mode I and II critical energy release rates, respectively.

Zhang *et al*. [19] investigated the effect of the thickness of nanofibrous interleaves and the nanofiber diameters in composites, concluding that finer nanofibers resulted in better improvements in interlaminar properties without altering the in-plane performance of toughened composites. Chen *et al*. [20] used electrospun carbon nanofiber mats to modify the interlaminar properties of conventional carbon fiber fabric-reinforced epoxy composites. It was demonstrated that the nanofibrous carbon interleaves could effectively improve the interlaminar and flexural properties of the composites. A significant enhancement in the in-plane and out-of-plane electrical conductivity was observed as well. In another study, Chen *et al*. [21] achieved superior mechanical properties. The main difference compared to the previous composite was that the nanofibers were collected on the surface of the microfibrous fabrics.

Nanofiber mats can be placed between laminate layers manually or can be deposited by directly spinning them onto the surface of the reinforcement [22, 23]. One of the most efficient technologies for covering a surface with nanofibers is a needleless technology called Nanospider™. This process is based on using an electric field to simultaneously induce numerous polymeric jets from a sufficiently large liquid surface carried on a roller wading in a bath of polymer solution [24].

The positive effects of the interlaminar incorporation of nanofibers have been proved mainly by static mechanical tests; however, the impact properties have not been as widely investigated [19, 23, 25].

The aim of this study was to investigate the interlaminar behavior of carbon fiber-reinforced epoxy matrix composite laminates toughened by electrospun nanofibers. Both unidirectional (UD) and woven carbon fabrics were covered directly by nanofibers and then laminated. The toughening effect was investigated by static mechanical and impact tests and scanning electron microscopy.

2. Materials and specimen preparation

For the production of nanofibers, polyacrylonitrile (PAN) copolymer was chosen because of its ductility and good adhesion to epoxy resin, which is a typical matrix material for high-performance carbon fiber-reinforced composites [26, 27]. The PAN supplied by a carbon fiber manufacturer was dissolved in dimethylformamide (DMF, Molar Chemicals, Hungary) with the aid of a magnetic mixer at 50°C for 6 hours in a beaker. The optimal concentration of the solution for electrospinning was determined to be 11 wt% based on our previous experiments [28]. The applied electrospinning setup is shown in Figure 1. Between the rotary spinneret electrode (Figure 1. (1)) and the grounded plate electrode (Figure 1. (2)), a moving textile collector was placed (Figure 1. (7)). The distance between the collector and the spinneret was set to 130 mm, and the traction speed of the collector was set to 100 mm/min by adjusting the rotation speed of the rollers (Figure 1. (6)). The applied voltage was 70 kV (direct current). Electrospinning was carried out in an air-conditioned chamber, where the temperature and relative humidity were set to 20°C and 20%, respectively. A low relative humidity level was set because the formed PAN fibers are very hygroscopic and the moisture in the PAN solution leads to early precipitation and beard formation.

As the primary reinforcement, the unidirectional carbon fabric Panex35 (PX35FBUD300, Zoltek Zrt., Hungary), with an areal density of 333 g/m^2, was selected. In this fabric, the linear density of yarns is 3700 tex and the thread count is 2/cm. The other material selected was Sigratex KDL 8003 (SGL Technologies GmbH, Germany), a plain weave carbon fabric with an areal density of 200 g/m^2. In this fabric, the linear density of yarns is 200 tex and the thread count is 5/cm in both the weft and warp directions.

In this work, different carbon fiber reinforcements were coated directly with nanofibers, indicating that the moving textile collector between the rollers (Figure 1. (6)) was the chosen microfibrous reinforcing fabrics themselves; therefore, nanofibers were produced exactly on the surface of the fabrics. The carbon fabrics were cut into 40 cm-wide strips, attached to the rollers and then coated with nanofibers.

Figure 2 shows the unidirectional carbon fabrics before (Figure 2a) and after electrospinning (Figure 2b) with a thin white layer of nanofibers.

After the coating process, the carbon fabrics were detached from the rollers and composite preparation procedure was implemented. As the matrix material,

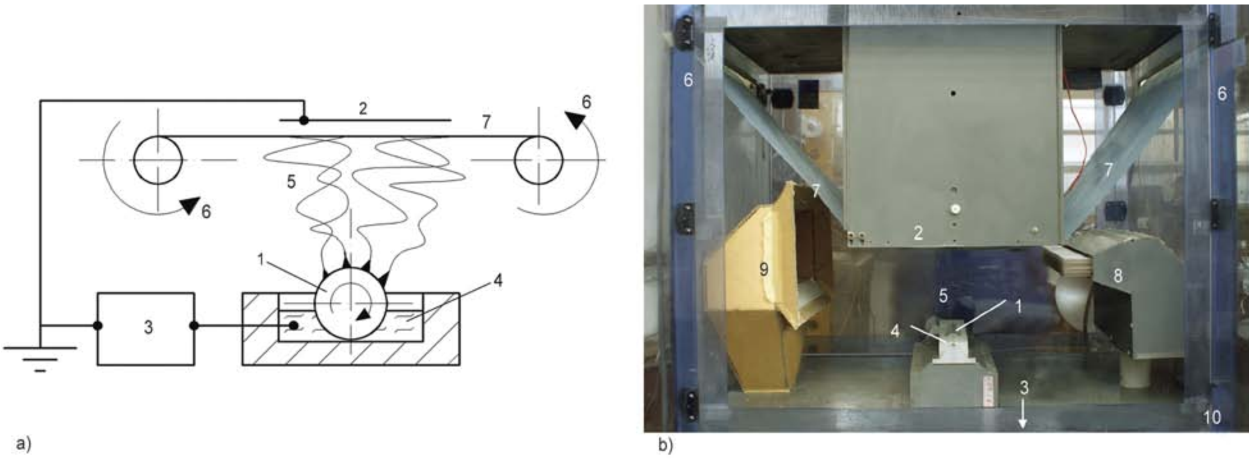

Figure 1. Electrospinning setup used to collect nanofibers on the surface of reinforcing materials. 1: rotary electrode, 2: grounded plate electrode, 3: high-voltage power supply, 4: polymer solution, 5: fiber formation space, 6: rollers, 7: moving belt collector, 8: air inlet, 9: air outlet, 10: chamber.

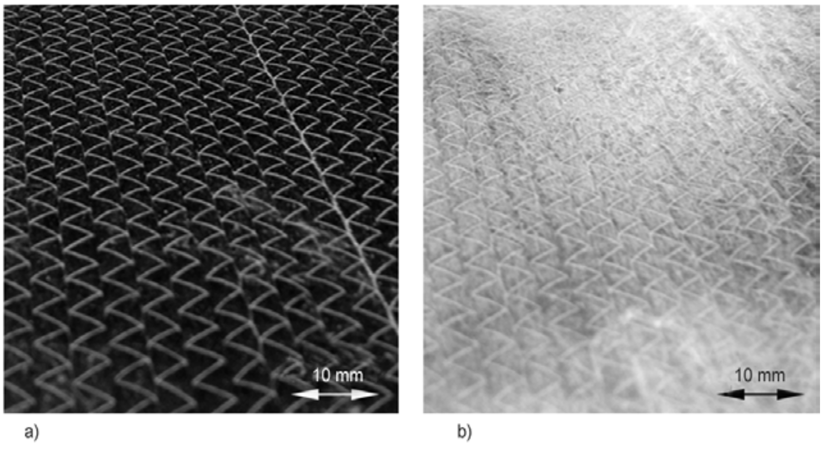

Figure 2. A sample of unidirectional carbon fabric before (a) and after (b) electrospinning

Table 1. Applied samples, measurement parameters and standards used for mechanical tests. UD: unidirectional, W: woven (fabric)

	Sample size [mm×mm]	Layers of primary reinforcement	Gauge/span length [mm]	Test/impact speed [variable]	Standard
ILSS	76.2×12.8	6-ply UD	25/6.35	1.3 mm/min	ASTM D3846-94
ILSS	76.2×12.8	4-ply W	25/6.35	1.3 mm/min	ASTM D3846-94
3PB	70×15	3-ply UD	56	5 mm/min	ISO 14125:1998
3PB	50×15	4-ply W	40	5 mm/min	ISO 14125:1998
Charpy	70×10	6-ply UD	56	2.9 m/s	ISO 179-2:2000
Charpy	25×10	4-ply W	20	2.9 m/s	ISO 179-2:2000
I-FWIT	70×70	4-ply W	ø20	4.4 m/s	ISO 6603-2

FM20-type (P+M Polimerkemia Kft., Hungary) epoxy resin was used, with a T16-type curing agent from the same company. The mass ratio of the components was 100:20 (epoxy:curing agent).

The specimens used for the investigations were produced by the wet hand layup method in a one-sided, polished sheet mold. After impregnation, vacuum pressing in a bag was applied to achieve a higher fiber content and to remove air bubbles. The pressure was set to 0.1 bar and held for 6 hours at 25°C. Post-curing was carried out at 60°C for 4 hours under the same pressure. The same number of reference coupons (without nanofibers) was also produced. To best compare the samples, all samples were prepared together at the same time and under the same curing and heat treatments.

Table 1 summarizes the characterization methods, sample sizes and measurement parameters. Five nanofiber-covered UD layers with one top (non-coated) UD layer [0_{N2}/0] were laminated for interlaminar shear strength (ILSS) and Charpy measurements. For three-point bending (3PB) testing, three layers with two interleaves [0_{N2}/0] were used. In the case of the woven reinforcement, four layers of the woven fabric composite (fiber direction: 0 and 90°) were laminated with three nanofibrous interleaves [$0F_{N3}$/0F] for the same measurements, which were supplemented by instrumented falling dart impact tests.

3. Mechanical and morphological characterizations

The composite samples had a thickness of approximately 2.8 mm in the case of the six-ply UD reinforcement, 1.4 mm for the three-ply UD reinforcement and 1 mm in the case of the woven fabric composite. The exact thickness values were evaluated from the measured fiber contents and the densities of the materials. A piece of weighed composite was placed in a ceramic crucible with a known mass. The crucible was heated to 600°C in a Nabertherm (Germany) oven and held at this temperature for an hour. From the residual ash mass, the carbon fiber content could be calculated for three individual specimens per sample.

The ILSS and 3PB tests were carried out on a Zwick Z005 (Germany) universal testing machine for seven specimens per sample type. The ILSS was determined by applying a tensile load instead of a compressive load to prevent the samples from buckling. Charpy-impact measurements were carried out on Ceast Resil Impactor Junior (Italy) impact tester equipped with a DAS 8000 data collector. The impact speed was 2.9 m/s, and the pendulum carried an energy of 2 J. In Charpy Ep (edge, parallel) tests, specimens are hit along the edge parallel to the piles of fibers, whereas in Charpy Fn (face, normal) tests, specimens are hit along the face normal to the direction of fibers. Seven specimens for each kind of sample and direction were investigated.

For the instrumented falling weight impact tests (I-FWIT), specimens were cut from the woven carbon fabric-reinforced laminates in the direction of the fiber orientations (the UD-reinforced composites were not suitable for this test). The measurements were carried out using a Ceast Fractovis (Italy) impact tester equipped with a DAS 8000 data collector to conduct seven measurements per sample type. The diameter of the dart was 20 mm, the diameter of the clamping unit was 40 mm, the falling mass was 23.62 kg, the impact speed was 4.4 m/s and the temperature was 23°C. The tip of the dart was lubricated with silicone oil to reduce the friction between the specimen and the dart. Subcritical impact tests of the specimens were carried out with a 3.62 kg falling mass carrying 0.6 J energy using the same equipment; during the measurement, the deformation and adsorbed energy were monitored. After the test, the residual deformation was zero; therefore, no fiber break occurred, but the matrix was damaged.

The morphology of the fracture surfaces was studied using a JEOL 6380 LA (Japan) SEM after sputtering the samples with Au/Pd alloy.

4. Results and discussion

The thickness of the electrospun layer was measured by SEM before impregnation and determined to be 27±5 μm. The areal density of the electrospun coating was measured to be 1 g/m^2. On the one hand, thicker interleaves may improve the quality of toughening [19]; on the other hand, they can significantly alter the cross-section of composites, therefore reducing their in-plane strength. The diameters of 250 nanofibers were determined based on the SEM images using the UTHSCSA Image Tool 3.0 software program. The average nanofiber diameter was determined to be 195±46 nm.

4.1. Fiber content

The results of carbon fiber content measurements, quasi-static ILSS and flexural tests for different types of composite samples are summarized in Table 2.

The carbon fiber content was approximately 50 wt% (approx. 38 V%) for each composite, which corresponds to the expected content. The type of reinforcing structure (UD or woven) and the presence of nanofibers (representing only 0.1 and 0.2 V% in the case of UD and woven reinforced composites, respectively) did not affect the fiber content; therefore, the results of the mechanical tests are comparable. The standard deviation of the carbon fiber weight is greater than the total weight of the nanofibers within the specimens; thus, the presence of nanofibers, in terms of the weight and size of the composites, was non-significant. It can also be concluded that the presence of the nanofibers did not change the quality of the impregnation.

4.2. Interlaminar shear strength

The interlaminar shear strength of the composites was observed to increase when nanofibers were used. The strengths of the unidirectional and woven fabric-reinforced composites were enhanced by 11 and 7%, respectively. It should be noted that the changes in the standard deviations were even more notable. The standard deviations decreased by 73 and 56%, respectively, which indicates that nanofibers made the failure process more uniform, which can be explained by the fact that the nanofibers could distribute the stress in-plane. Figure 3 shows SEM images of the fracture surfaces after the ILSS tests.

The images reveal that nanofibers could toughen the matrix. In the case of the reference materials, separation of the matrix and the carbon fibers (Figure 3a; 3d) occurred. The fracture surfaces appear rigid, and the fragmentation of the matrix into numerous pieces with sharp edges and no plastic deformation can be observed. In the case of the nanofibrous reinforcement (Figure 3b; 3e), the matrix partly remained on the surface of the primary reinforcement. The images suggest that after the fabrication of the composite, the nanofibers remained uniformly distributed between the reinforcing layers. Fracture occurred within the matrix, and the fracture surface became more structured than it was in the reference material in both cases. Overall, the nanofiber-containing matrix could distribute more stress and transmit the load toward the carbon fibers, thus changing the type of delamination that occurred and resulting in higher shear strength with a lower standard deviation, respectively.

The connection between the nanofibers and the matrix material was investigated at higher magnification (Figure 3c; 3f). In the case of the UD-rein-

Table 2. Interlaminar shear strength and flexural properties of composites with and without nanofibrous interleaves (UD CFRP: unidirectional carbon fiber-reinforced polymer; UD CFNRP: unidirectional carbon fiber and nanofiber-reinforced polymer; W CFRP: woven carbon fiber-reinforced polymer; W CFNRP: woven carbon fiber- and nanofiber-reinforced polymer)

	UD CFRP	UD CFNRP	W CFRP	W CFNRP
Carbon fiber content [wt%]	50.5±2.1	50.4±0.5	51.7±0.8	50.7±2.5
ILSS [MPa]	11.4±1.9	12.7±0.5	13.3±1.5	14.3±0.7
Change in ILSS [%]		+11%		+7%
Flexural strength [MPa]	778±86	945±61	610±23	534±65
Change in flexural strength [%]		+21%		–12%
Flexural modulus [GPa]	54.3±9.6	83.6±3.9	44.2±5.2	49.8±6.1
Change in flexural modulus [%]		+54%		+13%

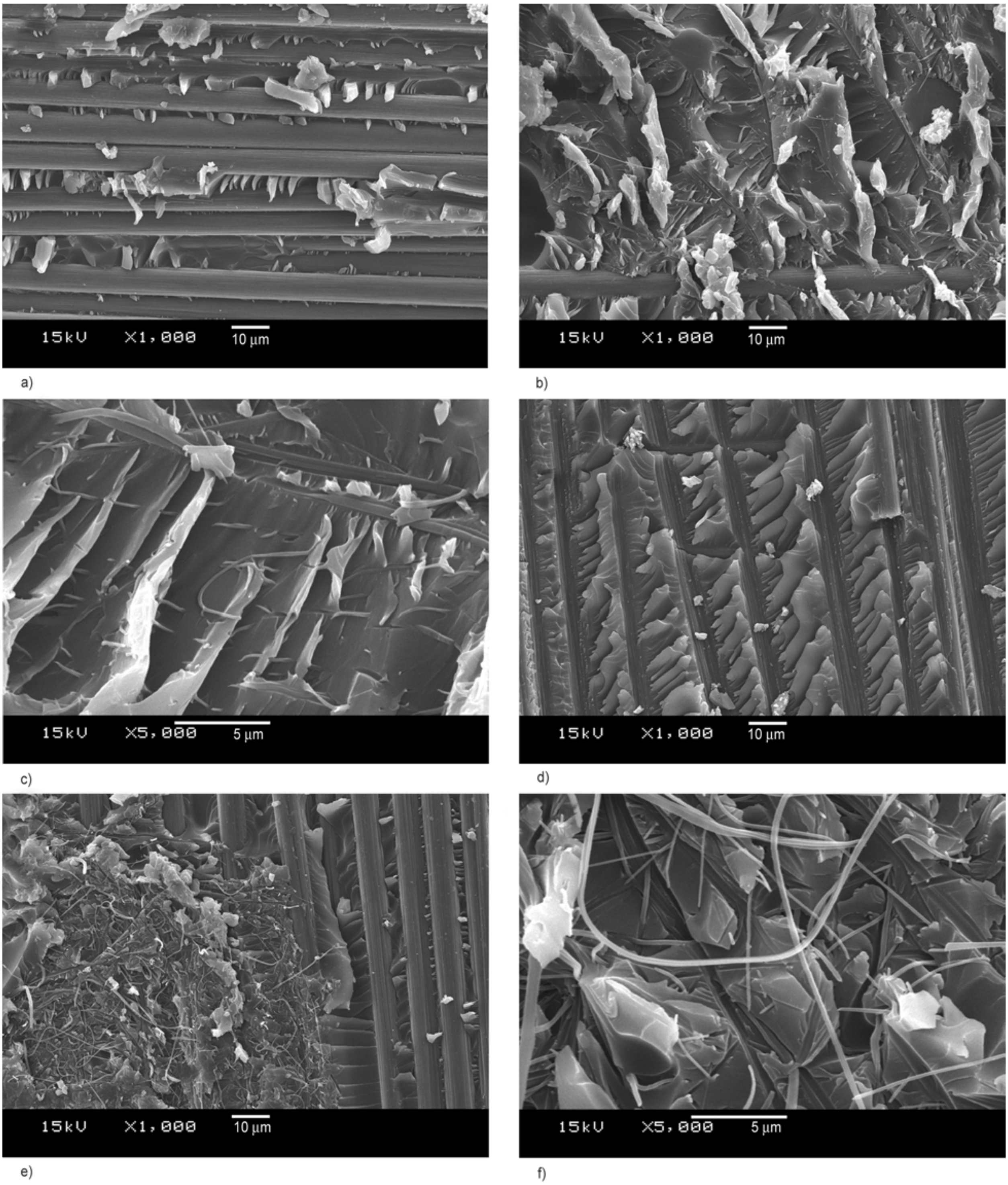

Figure 3. SEM images of the fracture surfaces of ILSS specimens. a) UD CFRP (×1000); b) UD CFNRP (×1000); c) UD CFNRP (×5000); d) W CFRP (×1000); e) W CFNRP (×1000); f) W CFNRP (×5000); W: woven reinforcement, UD: unidirectional fabric reinforcement

forced composite, broken nanofibers were observed, and there were some nanofibers that were still bonded to the matrix material and could stop crack propagation. Therefore, the nanofibers actively participated in load distribution, and plastic deformation could occur. In the case of the woven fabric-reinforced composites, the nanofibers debonded from the matrix and did not break. Because the surface was quite structured, a partial load distribution effect occurred, but in this case, the load distribution was less effective than in the case of the UD reinforcement. Because the preparation methods and the applied matrix were the same, the differences observed were caused by the structure of the composites. In the ILSS measurement, theoretically, there is pure shear stress between the layers of composites. In practice, however, the stress state also depends on the type of load transfer surface exhibited by composites. In the case of the UD reinforcement, the surface was approximately flat, but that of the woven fabric was wavy and uneven due to the shape of the weft and warp yarns entwining one another, leading to a more complex geometry and stress state between layers. These differences also manifested themselves in the smaller increase in the ILSS values.

4.3. Flexural behavior

The flexural properties of the composites varied more significantly (Table 2). At low deformation, the effect of the nanofibers was outstanding: the modulus increased by 54 and 13% in the UD and woven fabric reinforcements, respectively, which can be explained by the fact that in the nanofiber-toughened composites, the nanofibers could transfer the load toward the carbon fibers; thus, the utilization of carbon fibers was enhanced. However, the UD composites showed an increase in flexural strength when nanofibers were also applied, but this increase was not as high as that for the modulus. In the woven fabric reinforcement, the presence of nanofibers reduced the flexural strength values. To explain this behavior, the failure process must be examined. Typical failure curves are shown in Figure 4. Without nanofibers, the damage process of the specimens was rapid; when nanofibers were applied, failure gradually occurred. In the latter case, the layers broke independently one after the other. This phenomenon was confirmed by visual and acoustic observations of the damage process.

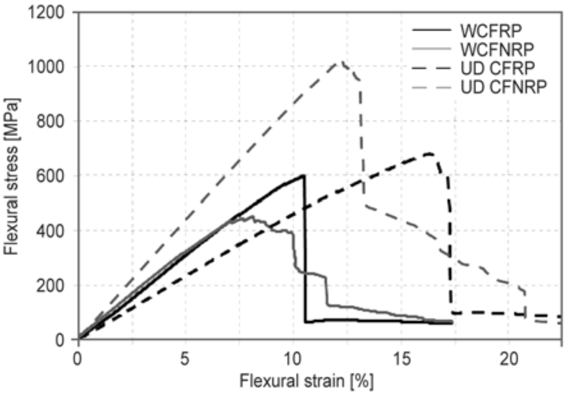

Figure 4. Typical flexural curves of the prepared composites

Figure 5a shows how the nanofibrous layer affected crack propagation. As cracks reached the nanofibrous part of the composite, the number of fracture trails increased and the surface became more structured, indicating an increase in toughness.

In Figure 5b, the arrow shown points to a nanofiber. The good adhesion of the nanofiber and matrix is indicated by their good physical contact after the composite was broken. The fracture around the nanofiber shows that the load was absorbed by the nanofiber and distributed throughout the matrix (crack propagation was blocked).

4.4. Charpy impact test

The results of the impact tests are shown in Table 3. By incorporating nanofibers, the initiation energy and the energy to maximum force increased in all cases. It can be concluded that in the Charpy Ep tests,

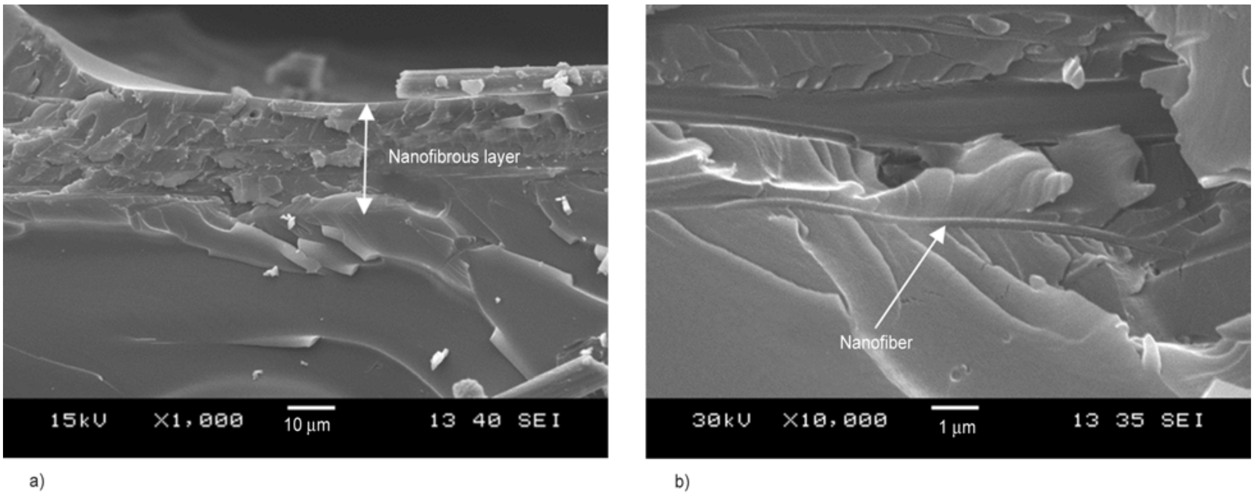

Figure 5. SEM images of the fracture surfaces of nanofiber-toughened flexural specimens after three-point bending tests. a) woven reinforced sample with a thin layer of nanofibers, b) adhesion between a nanofiber and matrix.

Table 3. Summary of Charpy test and I-FWIT results. Fn: face of the specimen is hit normal direction to the direction of fibers. Ep: edge of the specimen is hit parallel to the fiber reinforcement plies.

		UD CFRP	UD CFNRP	Change	W CFRP	W CFNRP	Change
Charpy Fn	Initiation energy [kJ/mm^2]	65.7±4.6	68.2±5.9	+4%	116±25	133±24	+14%
Charpy Fn	Total break energy [kJ/mm^2]	80.5±9.9	90.8±4.9	+13%	130±15	149±23	+15%
Charpy Ep	Initiation energy [kJ/mm^2]	24.1±3.1	35.5±10.5	+47%	37.7±20.1	153±40.6	+306%
I-FWIT	Total break energy [kJ/mm^2]	115±11.6	148±16.8	+29%	158±37.0	227±59.5	+44%
I-FWIT	Energy to maximum force [J/mm]	N/A	N/A	N/A	1.540±0.320	2.520±1.040	+64%
I-FWIT	Total break energy [J/mm]	N/A	N/A	N/A	8.590±0.190	8.07±0.58	–6%
I-FWIT	Absorbed energy at subcritical impact [J/mm]	N/A	N/A	N/A	0.267±0.033	0.349±0.036	+31%

the presence of nanofibers resulted in a major improvement in the initiation energy relative to that observed in the Charpy Fn tests for both the UD- and woven fabric-reinforced composites. The most significant increase was observed for the woven fabric-reinforced composite (W CFNRP) in the Charpy Ep impact test. As the composite was hit parallel to the plane of the reinforcing layers and the toughening interleaves, at the moment of impact, the entire area of the interleaves immediately became involved in bearing the applied load and nanofibers exerted their effects throughout the entire shear plane. In addition to being able to adsorb the impact energy via plastic deformation, these nanofibrous layers could transfer the load toward the adjacent carbon fiber layers. In the quasi-static ILSS tests of the woven reinforced composites, waviness of the interacting surfaces led to a moderate increase in ILSS. In this case, when the load transfer was instantaneous, the more complex geometry and larger area

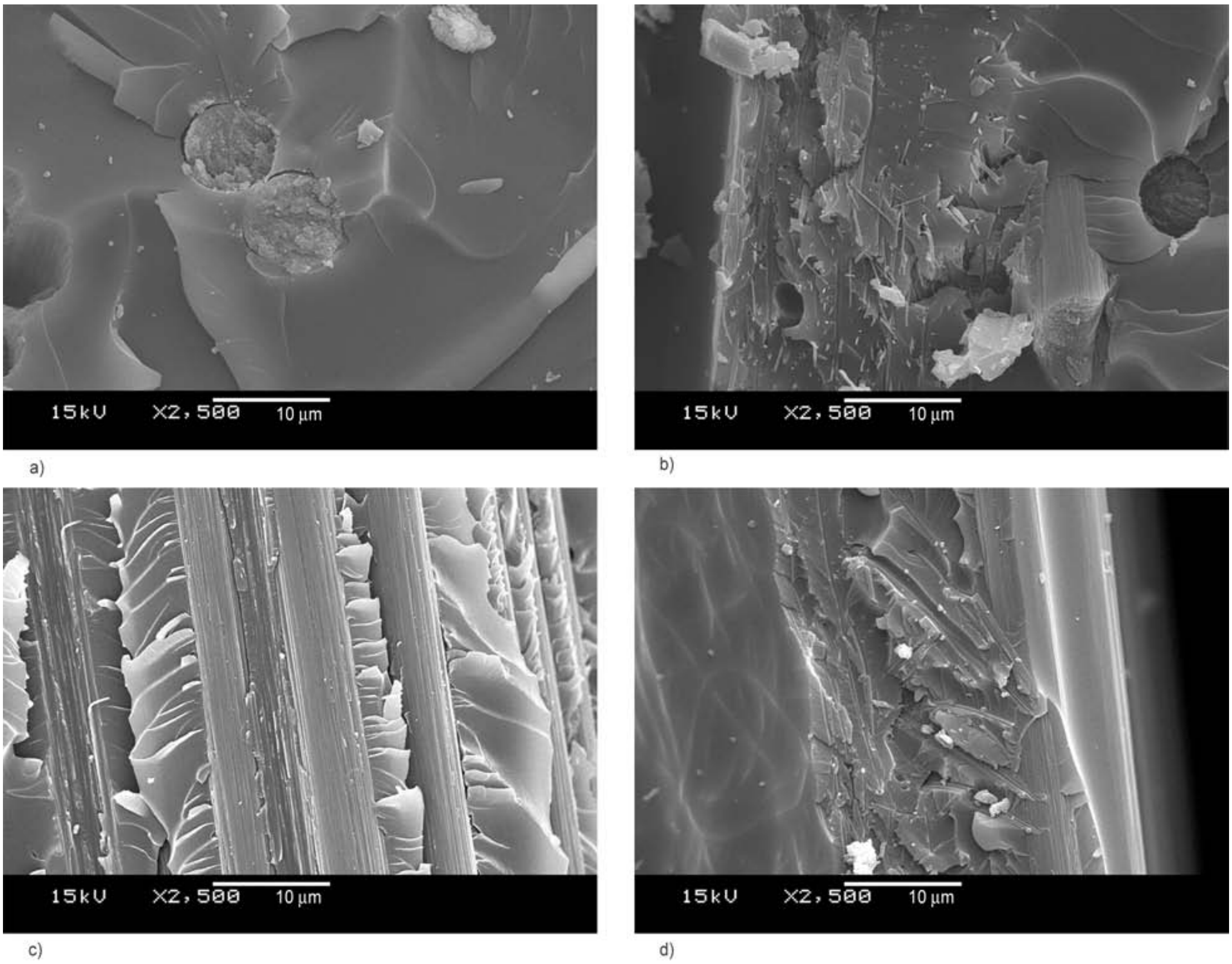

Figure 6. SEM images of surface fractures of Charpy Fn impact specimens. a) UD CFRP; b) UD CFNRP; c) W CFRP; d) W CFNRP; W: woven reinforcement, UD: unidirectional fabric reinforcement.

of the interacting surfaces resulted in an improved load-bearing ability. On the other hand, in the Charpy Fn test and I-FWIT, only the surfaces near the impact zone were involved in load transfer, and in this case, the stress field was continuously formed and changed during the damage process both in time and space.

Figure 6 shows SEM images of the fracture surfaces of the Charpy Fn impact specimens. In the nanofiber-reinforced samples (Figure 6b; 6d), nanofibers were present on the fracture surfaces and microfiber breakage could also be observed. Nanofiber layers with broken nanofibers can clearly be observed in the figures as distinct zones: to the left of the center of Figure 6b and at the center of Figure 6d. In the nanofiber-containing region, which is approximately 20 µm wide, broken nanofibers and a tough damage surface indicate good adhesion between the matrix and nanofibers. In the reference sample (Figure 6c), the matrix was separated from the fibers in small pieces, forming a rough interlaminar fracture surface. SEM images confirm that nanofibers played an important role in the damage process because they effectively blocked crack propagation.

4.5. Instrumented falling weight impact test

The total absorbed energy showed a moderate increase, except in the I-FWIT measurements (Table 3), in which a slight decrease was observed. In the I-FWIT, the energy to maximum force significantly increased by more than 60% and the adsorbed energy at subcritical impact improved by more than 30%, demonstrating the increased resistance of the nanofiber-toughened composites against dynamic stress. Overall, the results of the I-FWITs showed that if there were nanofibers in the composites, then they could stop the crack propagation process, allowing for a higher energy to maximum force. Because nanofibers are able to distribute the applied load, the nanocomposite layers may act as energy storage materials. After the breaking of these layers, the stored energy is released and the composite itself breaks more rapidly than the reference material. Thus, despite a higher energy to maximum force, the total absorbed energy decreases only slightly. This speculation corresponds well with the results of the three-point bending tests.

5. Conclusions

The toughening effect of nanofibrous interlayers in carbon fiber-reinforced structures was proven. Beneficial changes occurred not only in the static but also in the impact behavior of the composites. Under static loads, the positive effects were more significant in the UD-reinforced composites, for which the interlaminar shear strength increased by 11% and the flexural strength and modulus by 21 and 54%, respectively. This improvement was explained by the presence of nanofibers that could transfer the applied load toward the carbon fibers. The greatest improvements were observed in the Charpy Ep test results of the woven reinforced composites, in which the initiation energy increased three-fold. Falling dart impact tests revealed that the energy to maximum force increased by 64% in this material. These outstanding improvements are explained by the energy-absorption behavior of the nanofibrous composite layer.

Acknowledgements

This research was supported by the Czech-Hungarian intergovernmental research agency KONTAKT (CZ-07/2009) and by funding from the European Union's Seventh Framework Programme (FP7/2007-2013) for the Clean Sky Joint Technology Initiative under grant agreement no 270599. This work is related to the scientific program of the 'Development of quality-oriented and harmonized R+D+I strategy and functional model at BME' and to the New Széchenyi Plan (Project ID: TÁMOP-4.2.1/B-09/1/KMR-2010-0002 and TÁMOP- 4.2.2.B-10/1-2010-0009). This research was also supported by the Hungarian Research Fund (OTKA K100949, OTKA PD105564). This study is dedicated to the memory of our friend and student: Adam Papp.

References

[1] Subbiah T., Bhat G. S., Tock R. W., Parameswaran S., Ramkumar S. S.: Electrospinning of nanofibers. Journal of Applied Polymer Science, **96**, 557–569 (2005). DOI: 10.1002/app.21481

[2] Nagy Z. K., Balogh A., Vajna B., Farkas A., Patyi G., Kramarics Á., Marosi Gy.: Comparison of electrospun and extruded soluplus®-based solid dosage forms of improved dissolution. Journal of Pharmaceutical Sciences, **101**, 322–332 (2012). DOI: 10.1002/jps.22731

[3] Zhuo H. T., Hu J. L., Chen S. J.: Coaxial electrospun polyurethane core-shell nanofibers for shape memory and antibacterial nanomaterials. Express Polymer Letters, **5**, 182–187 (2011). DOI: 10.3144/expresspolymlett.2011.16

[4] del Valle L. J., Diaz A., Royo M., Rodriguez-Galan A., Puiggali J.: Biodegradable polyesters reinforced with triclosan loaded polylactide micro/nanofibers: Properties, release and biocompatibility. Express Polymer Letters, **6**, 266–282 (2012).
DOI: 10.3144/expresspolymlett.2012.30

[5] Li G., Li P., Zhang C., Yu Y., Liu H., Zhang S., Jia X., Yang X., Xue Z., Ryu S.: Inhomogeneous toughening of carbon fiber/epoxy composite using electrospun polysulfone nanofibrous membranes by *in situ* phase separation. Composites Science and Technology, **68**, 987–994 (2008).
DOI: 10.1016/j.compscitech.2007.07.010

[6] Tong L., Mouritz A. P., Bannister M. K.: 3D fibre reinforced polymer composites. Elsevier, Oxford (2002).

[7] Wu X-F., Yarin A. L.: Recent progress in interfacial toughening and damage self-healing of polymer composites based on electrospun and solution-blown nanofibers: An overview. Journal of Applied Polymer Science, **130**, 2225–2237 (2013).
DOI: 10.1002/app.39282

[8] Czél G., Czigány T.: A study of water absorption and mechanical properties of glass fiber/polyester composite pipes – Effects of specimen geometry and preparation. Journal of Composite Materials, **42**, 2815–2827 (2008).
DOI: 10.1177/0021998308096668

[9] Chen S. F., Jang B. Z.: Fracture behaviour of interleaved fiber-resin composites. Composites Science and Technology, **41**, 77–97 (1991).
DOI: 10.1016/0266-3538(91)90054-S

[10] Aksoy A., Carlsson L. A.: Interlaminar shear fracture of interleaved graphite/epoxy composites. Composites Science and Technology, **43**, 55–69 (1992).
DOI: 10.1016/0266-3538(92)90133-N

[11] Todo M., Jar P. B., Takahashi K.: Initiation of a mode-II interlaminar crack from an insert film in the end-notched flexure composite specimen. Composites Science and Technology, **60**, 263–272 (2000).
DOI: 10.1016/S0266-3538(99)00119-0

[12] Kishi H., Kuwata M., Matsuda S., Asami T., Murakami A.: Damping properties of thermoplastic-elastomer interleaved carbon fiber-reinforced epoxy composites. Composites Science and Technology, **64**, 2517–2523 (2004).
DOI: 10.1016/j.compscitech.2004.05.006

[13] Godara A., Gorbatikh L., Kalinka G., Warrier A., Rochez O., Mezzo L., Luizi F., van Vuure A. W., Lomov S. V., Verpoest I.: Interfacial shear strength of a glass fiber/epoxy bonding in composites modified with carbon nanotubes. Composites Science and Technology, **70**, 1346–1352 (2010).
DOI: 10.1016/j.compscitech.2010.04.010

[14] Deng F., Lu W., Zhao H., Zhu Y., Kim B-S., Chou T-W.: The properties of dry-spun carbon nanotube fibers and their interfacial shear strength in an epoxy composite. Carbon, **49**, 1752–1757 (2011).
DOI: 10.1016/j.carbon.2010.12.061

[15] Tan K. T., Watanabe N., Yoshimura A., Iwahori Y.: Validation of delamination reduction trend for stitched composites using quasi-static indentation test. in 'Proceedings of the 15th European Conference on Composite Materials (ECCM-15), Venice, Italy' 282, p7 (2012).

[16] Zhang X., Hounslow L., Grassi M.: Improvement of low-velocity impact and compression-after-impact performance by z-fibre pinning. Composites Science and Technology, **66**, 2785–2794 (2006).
DOI: 10.1016/j.compscitech.2006.02.029

[17] Kornmann X., Rees M., Thomann Y., Necola A., Barbezat M., Thomann R.: Epoxy-layered silicate nanocomposites as matrix in glass fibre-reinforced composites. Composites Science and Technology, **65**, 2259–2268 (2005).
DOI: 10.1016/j.compscitech.2005.02.006

[18] Dzenis Y. A., Reneker D. H.: Delamination resistant composites prepared by small diameter fiber reinforcement at ply interfaces. U.S. Patent 6265333, USA (2001).

[19] Zhang J., Lin T., Wang X.: Electrospun nanofibre toughened carbon/epoxy composites: Effects of polyetherketone cardo (PEK-C) nanofibre diameter and interlayer thickness. Composites Science and Technology, **70**, 1660–1666 (2010).
DOI: 10.1016/j.compscitech.2010.06.019

[20] Chen Q., Zhang L., Rahman A., Zhou Z., Wu X-F., Fong H.: Hybrid multi-scale epoxy composite made of conventional carbon fiber fabrics with interlaminar regions containing electrospun carbon nanofiber mats. Composites Part A: Applied Science and Manufacturing, **42**, 2036–2042 (2011).
DOI: 10.1016/j.compositesa.2011.09.010

[21] Chen Q., Zhao Y., Zhou Z., Rahman A., Wu X-F., Wu W., Xu T., Fong H.: Fabrication and mechanical properties of hybrid multi-scale epoxy composites reinforced with conventional carbon fiber fabrics surface-attached with electrospun carbon nanofiber mats. Composites Part B: Engineering, **44**, 1–7 (2013).
DOI: 10.1016/j.compositesb.2012.09.005

[22] Sihn S., Kim R. Y., Huh W., Lee K-H., Roy A. K.: Improvement of damage resistance in laminated composites with electrospun nano-interlayers. Composites Science and Technology, **68**, 673–683 (2008).
DOI: 10.1016/j.compscitech.2007.09.015

[23] Zhang J., Yang T., Lin T., Wang C. H.: Phase morphology of nanofibre interlayers: Critical factor for toughening carbon/epoxy composites. Composites Science and Technology, **72**, 256–262 (2012).
DOI: 10.1016/j.compscitech.2011.11.010

[24] Jirsak O., Sanetrnik F., Lukas D., Kotek V., Martinova L., Chaloupek J.: A method of nanofibres production from a polymer solution using electrostatic spinning and a device for carrying out the method. International Patent WO 2005/024101 A1 (2005).

[25] Akangah P., Lingaiah S., Shivakumar K.: Effect of Nylon-66 nano-fiber interleaving on impact damage resistance of epoxy/carbon fiber composite laminates. Composite Structures, **92**, 1432–1439 (2010).
DOI: 10.1016/j.compstruct.2009.11.009

[26] Liao C-C., Wang C-C., Chen C-Y., Lai W-J.: Stretching-induced orientation of polyacrylonitrile nanofibers by an electrically rotating viscoelastic jet for improving the mechanical properties. Polymer, **52**, 2263–2275 (2011).
DOI: 10.1016/j.polymer.2011.03.018

[27] Nataraj S. K., Yang K. S., Aminabhavi T. M.: Polyacrylonitrile-based nanofibers – A state-of-the-art review. Progress in Polymer Science, **37**, 487–513 (2012).
DOI: 10.1016/j.progpolymsci.2011.07.001

[28] Molnár K., Koštáková E., Vas L. M.: Preparation of composites reinforced with '*in situ*' electrospun fibres. in 'Proceedings of the European Conference on Composite Materials (ECCM-14), Budapest, Hungary' 116-ECCM14, p7 (2010).